信州大学審査学位論文

DYNAMIC ANALYSIS OF CARBON NANOTUBES BASED ON CONTINUUM MECHANICAL MODELS

March 2012

Xiao-Wen LEI

ABSTRACT

The study of vibration in carbon nanotubes (CNTs) is currently a major topic of interest that increases understanding of their dynamic mechanical behavior. By now, there are three methods to analyze the mechanical properties of CNT. They are spectroscopy experiment, computational simulation and theoretical analysis. However, technically these are difficult experiments of vibrational properties because of the small diameter of the nanotubes, and plenty of time will be spent on the molecular dynamics (MD) simulation. Theoretical analyses have shown the advancement on the taken cost and the spent time of researches compared with experiment operation and MD simulation method, and they can predict some results which cannot be achieved by the other two methods by now. Elastic continuum models are used to study the vibrational behavior of CNTs to avoid the difficulties encountered during experimental characterization of nanotubes as well as the time-consuming nature of computational atomistic simulations. Especially, the elastic continuum models can provide the disciplines of CNTs on vibrational properties in a concise method.

This thesis focuses on building continuum models of CNTs based on the elastic continuum mechanics theory, and analyzing the vibrational properties of CNTs in different conditions. Using the built models, the calculation processes and analysis results are to be accurate and brief, which are easy to use on engineering applications.

Step from the mechanical properties of single-walled carbon nanotubes (SWCNTs), a continuum model of SWCNTs at atomic scale is carried out. The carbon-carbon

(*C-C*) bonds between two adjacent atoms are modeled as Euler beams. According to the relationship of Tersoff-Brenner force theory and potential energy acting on *C-C* bonds, material constants of beam element are determined at the atomic scale. Based on the elastic deformation energy and mechanical equilibrium of a unit in graphite sheet, simply form equations of calculating Young's modulus of armchair and zigzag graphite sheets are derived. Following with the geometrical relationship of SWCNTs in cylindrical coordinates and the structure mechanics approach, Young's modulus and Poisson's ratio of armchair and zigzag SWCNTs are also investigated.

To calculate the resonant vibration of double-walled carbon nanotubes (DWCNTs) and the DWCNTs embedded in an elastic medium, a theoretical analysis is presented based on Euler–Bernoulli beam model and Winkler spring model. The vibration modes of DWCNTs are quite different from those of SWCNTs. The resonant vibrations of DWCNTs are found to have in-phase and anti-phase modes, in which the deflections of the inner and outer nanotubes occur in the same and opposite directions, respectively. For the vibration of DWCNTs with the same harmonic numbers, the resonant frequencies of anti-phase mode are larger than the ones of in-phase mode. Moreover, influence of the surrounding medium on the resonant vibrations is investigated using the Winkler spring model. The results show that surrounding medium makes a strong impact on the vibration frequencies of in-phase mode, but little on those of anti-phase mode.

And, the Euler–Bernoulli beam model is also used to analyze the resonant vibration of DWCNTs with inner and outer nanotubes of different lengths. The resonant properties of DWCNTs with different inner and outer nanotube lengths are investigated in detail using the theoretical approach. The resonant vibration is significantly affected by the vibrational modes of the DWCNTs, and by the lengths of the inner and outer nanotubes. For an inner or outer nanotube of constant length, the

vibrational frequencies of the DWCNTs increase initially and then decrease as the length of another nanotube increases. A design for nano-electromechanical devices that operate at various frequencies can be realized by controlling the length of the inner and outer nanotubes of DWCNTs.

The vibration behaviors of DWCNTs, accounting for surface effects, are studied based on the nonlocal Bresse-Timoshenko theory. The influences of the surface elasticity modulus, residual surface stress, nonlocal parameter, axial half-wave number and aspect ratio are investigated in detail. The present analysis shows that the effective surface properties influence on the natural frequency of CNTs are significant. It is shown that the natural frequency is largely affected by the surface material, nonlocal parameter, vibration mode and aspect ratio. Especially in short DWCNTs for the higher vibrational modes, the influence of the nonlocal and surface effects on vibration frequency is more pronounced.

A theoretical vibrational analysis of the radial breathing mode (RBM) of DWCNTs subjected to pressure is presented based on an elastic shell continuum model. The results agree with reported experimental results obtained under different conditions. Frequencies of the RBM in DWCNTs subjected to increasing pressure depend strongly on circumferential wave numbers, but weakly on the aspect ratio and axial half-wave numbers. For the inner and outer tubes of DWCNTs, the frequency of the RBM increases obviously as the pressure increases under different conditions. The range of variation is smaller for the inner tube than the outer tube.

The theoretical analysis of the RBM of CNTs subjected to axial pressure is also presented based on an elastic continuum model. SWCNTs are described as an individual elastic shell and DWCNTs are considered to be two shells coupled through the van der Waals force. The effects of axial pressure, wave numbers and nanotube diameter on the RBM frequency are investigated in detail. The validity of these

theoretical results is confirmed through the comparison of the experiment, calculation and simulation. Our results show that the RBM frequency is linearly dependent on the axial pressure and is affected by the wave numbers. We concluded that RBM frequency can be used to characterize the axial pressure acting on both ends of a CNT.

ACHIEVEMENT

OVERSEAS EDUCATION

Study in Columbia University in the City of New York from October 2011 to December 2011 as a scholar visitor.

LIST OF PUBLICATIONS

Journal Publications

1. **Xiao-Wen Lei**, Toshiaki Natsuki, Jin-Xing Shi, Qing-Qing Ni, Analysis of carbon nanotubes on the mechanical properties at atomic scale. Journal of Nanomaterials. 2011; 805313: 1.
2. Toshiaki Natsuki, **Xiao-Wen Lei**, Qing-Qing Ni, Morinobu Endo, Free vibration characteristics of double-walled carbon nanotubes embedded in an elastic medium. Physics Letters A. 2010; 374: 2670.
3. Toshiaki Natsuki, **Xiao-Wen Lei**, Qing-Qing Ni, Morinobu Endo, Vibrational analysis of double-walled carbon nanotubes with inner and outer nanotubes of different lengths. Physics Letters A. 2010; 374: 4684.
4. **Xiao-Wen Lei**, Toshiaki Natsuki, Jin-Xing Shi, Qing-Qing Ni, Surface effects on the vibrational frequency of double-walled carbon nanotubes using the nonlocal Timoshenko beam model. Composites Part B, 2012, 43: 64.
5. **Xiao-Wen Lei**, Toshiaki Natsuki, Jin-Xing Shi, Qing-Qing Ni, Radial breathing vibration of double-walled carbon nanotubes subjected to pressure. Physics Letters A, 2011; 24: 2416.

6. **Xiao-Wen Lei**, Qing-Qing Ni, Jin-Xing Shi, Toshiaki Natsuki, Radial breathing vibration of double-walled carbon nanotubes subjected to axial pressure. Nanoscale Research Letters, 2011; 6: 492

---

7. Jin-Xing Shi, Qing-Qing Ni, **Xiao-Wen Lei**, Toshiaki Natsuki, Nonlocal elasticity theory for the buckling of double-layer graphene nanoribbons based on a continuum model. Computational Materials Science 2011; 50: 3085.
8. Kai Wei, Yuan Li, **Xiao-Wen Lei**, Heejae Yang, Akira Teramoto, Juming Yao, Koji Abe, Frank K. Ko, Emulsion electrospinning of collagen-like protein/PLGA fibrous scaffold: Empirical modeling and preliminary release assessment of encapsulated protein. Macromolecular Bioscience, 2011, DOI: 10.1002/mabi.201100141.
9. Jin-Xing Shi, Qing-Qing Ni, **Xiao-Wen Lei**, Toshiaki Natsuki, Wave propagation in embedded double-layer graphene nanoribbons as electromechani. Journal of Applied Physics, 2011; 110: 084321.
10. Jin-Xing Shi, Qing-Qing Ni, **Xiao-Wen Lei**, Toshiaki Natsuki, Nonlocal vibration of embedded double-layer graphene nanoribbons in in-phase and anti-phase modes. Physica E: Low-dimensional Systems and Nanostructures, doi:10.1016/j.physe.2011.12.023.

Conference Publications

11. **Xiao-Wen Lei**, Toshiaki Natsuki, Jin-Xing Shi, Qing-Qing Ni, Natural frequencies of carbon nanotubes accounting for surface effects. International Conference on Advanced Fiber / Textile Materials. December, 2011.
12. **Xiao-Wen Lei**, Toshiaki Natsuki, Jin-Xing Shi, Qing-Qing Ni, Vibration characteristics of double walled carbon nanotubes subjected to pressure. International Conference of Composite Materials. August, 2011.
13. **Xiao-Wen Lei**, Toshiaki Natsuki, Jin-Xing Shi, Qing-Qing Ni, Radial breathing vibration of double-walled carbon nanotubes subjected to axial pressure. Villa conferences on Energy, Materials and Nanotechnology. April, 2011.
14. **Xiao-Wen Lei**, Toshiaki Natsuki, Jin-Xing Shi, Qing-Qing Ni, Analysis of carbon nanotubes on mechanical properties. International Conference of Future Textile. July, 2010.

ACKNOWLEDGMENTS

This thesis would not have been possible without the guidance and the help of several individuals who in one way or another contributed and extended their valuable assistance in the preparation and completion of this study.

First of all I would like to thank my supervisor Prof. Qing-Qing Ni for giving me the opportunity to do this study in his group and for always encouraging me positively and supporting me in both study and life with useful advice.

I am also grateful to Prof. Toshiaki Natsuki as my vice advisor, for his assistance and guidance in getting my doctoral career started on the right foot and providing me with the foundation for becoming a mechanical researchers.

I am particularly grateful to Prof. Xi Chen in Columbia University in the City of New York for the discussion and helpful suggestions and comments. Especially, for the study in Prof. Chen's group from October to December, 2011, he and his research group gave me a distinctive time in Columbia University in the city of New York.

I thank Prof. Masayuki Takatera, Prof. Michihiko Koseki and Prof. Ning Hu to be co-referees of the thesis and for the discussion and helpful suggestion and comments.

I want to express my gratitude to Global COE of Shinshu University for financial support, a program by the Ministry of Education, Culture, Sports, Science and Technology in Japan.

I really appreciate the friends in Shinshu University, especially my group mates (Dr. Li Zhang, Dr. Chao Du, Dr. Yang Hua, Dr. Hong-Xia Jiang, Mr. Xu-Dong Jin, Mr. Fan

Liu, Mr. Yao-Feng Zhu, Mr. Yi Wang, Mr. Ryo Ueno, Mr. Keiji Suzuki, Miss Yan Wang and Mr. Ran Li), we have a memorable time for studying and living together.

Special thanks to Professor Ying-Hua Zhao and Professor Gang Yang at Dalian Maritime University in China for their constant support and encouragement.

Finally, and most importantly, I would like to thank my husband Mr. Jin-Xing Shi. His support, encouragement and unwavering love were undeniably the bedrock upon which the past years of my life have been built. I thank my parents, Ming Lei and Yun-Ling Zhu, for their faith in me and allowing me to be as ambitious as I wanted. It was under their watchful eye that I gained so much drive and an ability to tackle challenges head on. Also, I thank Jin-Xing's parents, Xi-You Shi and Shu-Hua Liu. They, like Jin-Xing and me, are a couple who endured and survived the experience of graduate school and provided me with unending encouragement and support.

January, 2012

in Japan

TABLE OF CONTENTS

CHAPTER ONE

General Introduction

1 General introduction

1.1 Introduction

In 1985, a molecule called buckminsterfullerene was discovered by a group of researchers at Rice University [1]. This molecule consisted of 60 carbon atoms in sp^2 hybridized bonds arranged in a surprisingly symmetric fashion. The Nobel Prize was awarded to Richard Smalley, Robert Curl, and Harry Kroto for their discovery of this new allotrope of carbon, they predicted the possibility of innovations that will allow for "manipulating and controlling things on small-scale." [2] Endo et al. [3] have reported that carbon nanofibers with diameter ranging from 20 to more than 500 Å were prepared by paralyzing a mixture of benzene and hydrogen at high temperature. This discovery was groundbreaking for the now vibrant field of carbon nanotechnology [4].

Carbon nanotubes (CNTs), discovered in 1991 by Sumio Iijima [5], are members of the fullerene family. Their morphology is considered equivalent to a graphene sheet rolled into a seamless tube capped on both ends. The main properties that make CNTs a promising technology for many future applications are: extremely high strength, low mass density, and linear elastic behavior up to strains of 12%, almost perfect geometrical structure, and nanometer scale structure.

1.2 Structure and mechanical property of CNTs

Since their discovery, CNTs have generated huge activity in most areas of science

and engineering due to their unprecedented physical and chemical properties [6-9]. No previous material has displayed the combination of superlative mechanical, thermal and electronic properties attributed to them [10]. These properties make nanotubes ideal, not only for a wide range of applications but as a test bed for fundamental nanoscience and nanotechnology [11, 12].

1.2.1 Structure of CNTs

The structure of CNTs has been explored early on by high resolution Transmission Electron Microscopy (TEM) and Scanning Tunneling Microscopy (STM) techniques [15], yielding direct confirmation that the nanotubes are seamless cylinders derived from the honeycomb lattice representing a single atomic layer of crystalline graphite [16], called a graphene sheet, [Figure. 1.1 (*a*)]. The structure of a single-wall carbon nanotube is conveniently explained in terms of its 1D unit cell, defined by the vectors C_h and T in Figure 1.1 (*a*).

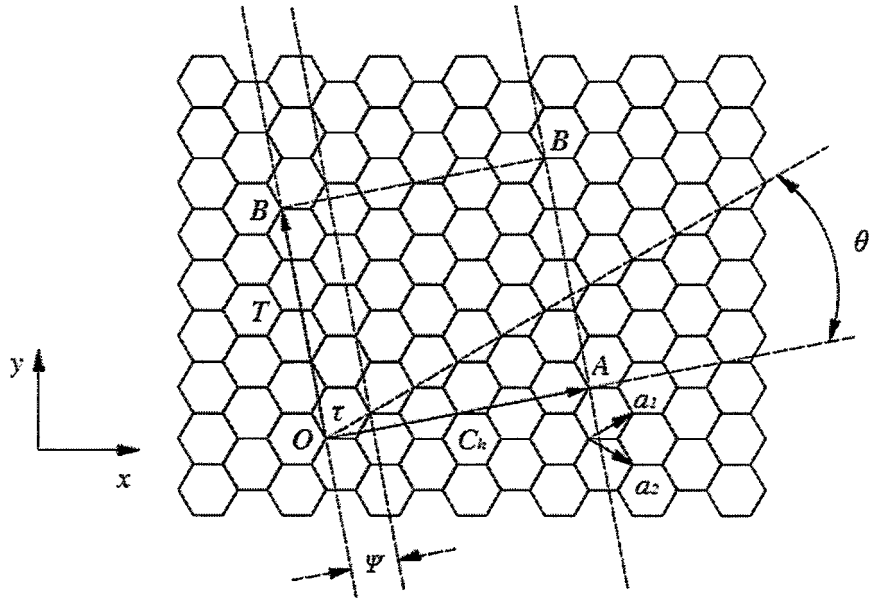

(*a*)

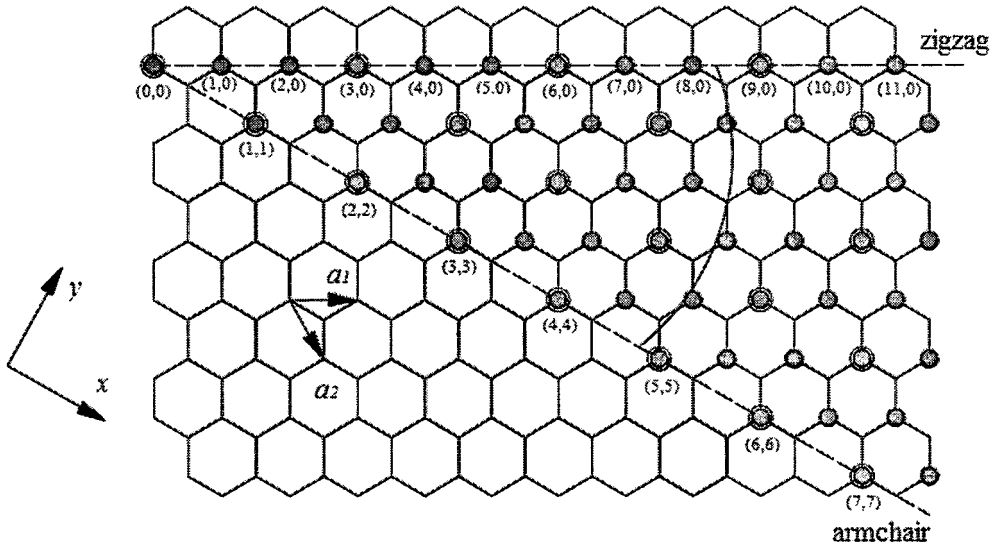

(*b*)

Figure 1.1 (*a*) The chiral vector $\overrightarrow{OA}$ or $C_h = n\hat{a}_1 + m\hat{a}_2$ is defined on the honeycomb lattice of carbon atoms by unit vectors $\hat{a}_1$ and $\hat{a}_2$ and the chiral angle θ with respect to the zigzag axis. Along the zigzag axis $\theta = 0°$. Also shown are the lattice vector $\overrightarrow{OB} = T$ of the 1D nanotube unit cell and the rotation angle Ψ and the translation τ which constitute the basic symmetry operation R = ($\Psi|\tau$) for the carbon nanotube. The diagram is constructed for (n,m) = (4, 2) [13]. (*b*) Possible vectors specified by the pairs of integers (n,m) for general carbon nanotubes, including zigzag, armchair, and chiral nanotubes. Below each pair of integers (n,m) is listed the number of distinct caps that can be joined continuously to the carbon nanotube denoted by (n,m) [13]. The encircled dots denote metallic nanotubes while the small dots are for semiconducting nanotubes [14]

The chirality and the fiber diameter are uniquely specified by the vector $C_h = na_1 + ma_2 \equiv (n, m)$, where n, $m$are integers and a_1, a_2 the unit vectors of graphite, and C_h connects two crystal graphically equivalent sites, A and A', as shown in Figure 1.1. The graphene cylinder is formed by connecting together the points A and A' and the cylinder joint is made along the lightly dotted lines perpendicular to C_h. The fiber diameter d is defined by $d = |C_h|/\pi = a\sqrt{n^2 + nm + m^2}/\pi$, where a = 1.42×$\sqrt{3}$Å is the lattice constant. The chiral fiber thus generated has no distortion of bond angles other than that caused

by the cylindrical curvature of the fiber. This generalized description of chiral fibers [Figure. 1.1 (*b*)] includes a range of orientations for C_h extending from the zigzag direction [$\theta = 0^\circ$, or $(n, m) = (p,0)$, p is an integer] to the armchair direction [$\theta = \pm 30^\circ$, $(n, m) = (2p, -p)$, (p, p)], which form two limiting cases. The chiral angle, θ = arctan $[-\sqrt{3}m/(2n+ m)]$, is defined as the angle between C_h and the zigzag direction, as shown in Figure 1.1 (*a*). Since there are six definable angles for a fiber because of the hexagonal local structure, we select $|\theta| \leq 30^\circ$ or $-n \leq m \leq n$ ($n \geq 0$). Since there is no mirror symmetry for a fiber, both right- ($\theta > 0^\circ$) and left- ($\theta < 0^\circ$) handed optical isomers are possible, as are also chiral fibers with $|\theta| > 30^\circ$. The chiral angle θ should determine the optical activity of the fiber and the speed (or stability) of fiber growth [17]. Figure 1.1 (*b*) indicates the nanotubes that are semiconducting and those that are metallic, and shows the number of distinct fullerene caps that can be used to close the ends of an (n,m) nanotube, such that the fullerene cap satisfies the isolated pentagon rule [18, 19].

Single-walled carbon nanotubes (SWCNTs) can be ideally constructed starting from a graphite sheet. According to the chiral vector, there are three kinds of structure, armchair CNTs, zigzag CNTs and chiral CNTs.

1.2.2 Mechanical property of CNTs

Because of the atomic structure of CNTs, they have attracted considerable attention in the scientific community. This is partly because of their novel mechanical and physical properties [21-24]. The mechanical properties of CNTs have been extensively investigated by researchers in mechanical fields. Experimental measurements and theoretical analyses have shown that CNTs possess excellent mechanical stiffness and strength [25-27].

By assuming CNT as a structural member, the elastic properties of CNT can be obtained from different methods. Researchers using micro-Raman spectroscopy [28],

direct tensile loading tests [29, 30], and beam model [31-33] reported Young's modulus of CNT are over 1 TPa and tensile strength is about 60 GPa [34, 35] exceptionally higher than those of steel (200 GPa and 500 MPa, respectively). Hence, CNTs are five times stiffer and over a hundred times stronger than steel but are yet six times lighter [36]. Hence have great potential for applications that require high- modulus and high-strength materials, especially in vibration application.

1.3 Vibration property of CNTs

The study of vibration in CNTs is currently a major topic of interest [37-40], which can be used to further understand their dynamic mechanical behavior. The study of vibrational properties can be used to measure the elastic modulus of individual CNTs [41, 42]. The vibrational properties of CNTs are quite important in micro electro mechanical system (MEMS), high-frequency resonators and sensors. The studies of vibrational properties in CNTs are of great current interest, which can be used indirectly determine the elastic modules of individual CNTs. The CNT dimensions and vibration amplitudes were measured by electron micrographs, and it was assumed that the vibration modes were driven stochastically and chosen of clamped cantilevers [42].

Natural frequencies are the intermediate step to find the response of the system. In other words, all objects have a set of natural frequencies at which they vibrate when exited. The actual natural frequency depends on the properties of the material that the object is made of and the dimensions of structure. The primary tool for vibrational analysis of beams is the Euler–Bernoulli beam equation [43-45] or Bresse-Timoshenko beam equations [46-47] which allow quick calculation of the natural frequencies of structural elements.

1.4 Continuum mechanical model of CNTs

Since CNTs are extremely small to several nanometers in the diameter, their experimental measurement is very difficult to obtain good accuracy [48]. Therefore, computational simulations have been regarded as a powerful tool in view of such experimental difficulty.

Although the dimensions of CNTs are from a few to tens of nanometers (nm) in diameter, and a few millimeters (mm) long, continuum models have been found to describe their mechanical behavior very well under many circumstances. The Euler–Bernoulli beam theory is used for small deformation and large aspect length to diameter ratios, Bresse-Timoshenk theory for small aspect ratios, and shell theory for larger and more complicated distortions [49]. In recent years, cylindrical shell models [50-54] are also used for studying the basic mechanic properties of CNT.

In this thesis, the main objective is to review recent researches on the vibrational properties by computational modeling and simulation for CNTs. The theoretical approaches are based on including the atomic-based continuum model, the Euler-Bernoulli beam, the Bresse-Timoshenko beam model and the three-dimensional elastic shell mode.

1.4.1 Atomistic continuum model

An atomistic-based continuum theory is based on linkage of computational chemistry and solid mechanics. For CNT systems, Odegard et al. [55] have developed an equivalent-continuum model served as structure-property relationships of nanostructured materials. The linkage was established by replacing discrete molecular structures with equivalent-continuum models. This replacement may be accomplished by equating the molecular potential energy of nanostructured materials with the

mechanical strain energy of representative continuum model. There are two reported models of CNTs which are shown in Figure 1.2 and Figure 1.3.

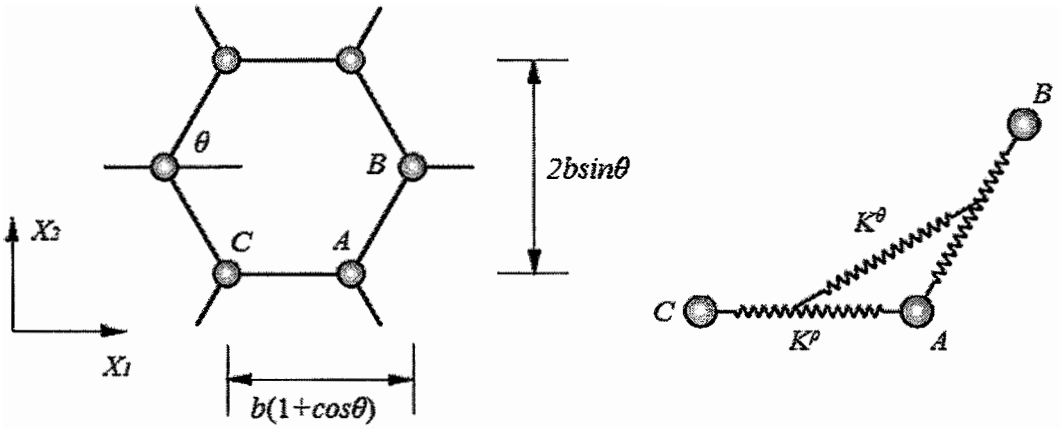

Figure 1.2 Element of a frame structure model [27].

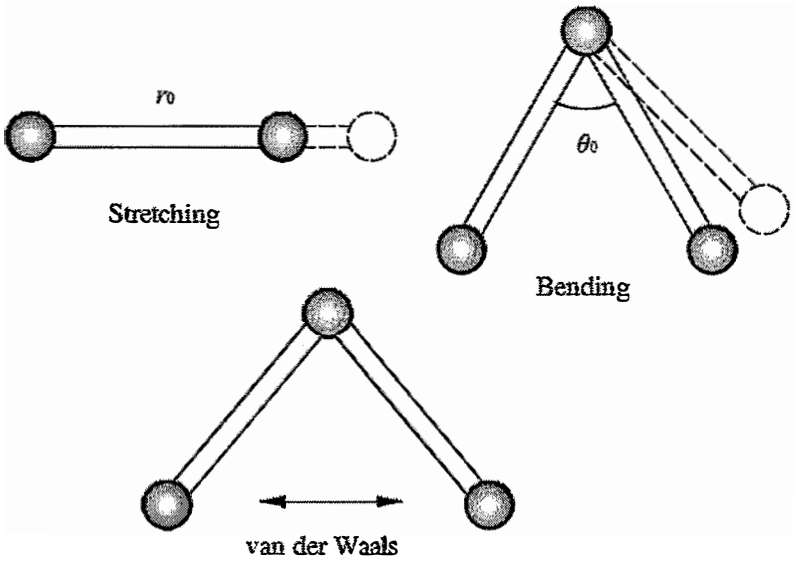

Figure 1.3 Inter-atomic interactions in molecular mechanics [56].

1.4.2 Euler-Bernoulli beam model

Euler-Bernoulli beam is a simplification of the linear beam theory of elasticity which provides a means of calculating the load-carrying and deflection characteristics of

beams. It covers the case for small deflections of a beam which is subjected to lateral loads only. The different boundary conditions in Euler-Bernoulli beam are shown in Figure 1.3. Although CNTs have smaller diameters only several times larger than the length of a bond between CNTs, a continuum approach has been found to describe their mechanical behaviors very well. The Euler--Bernoulli beam theory neglects shear deformations by assuming that plane sections remain plane and perpendicular to the neutral axis during bending. As a result, shear strains and stresses are removed from the theory [57].

1.4.3 Bresse-Timoshenko beam model

Consider that the effects of the shear deformation and the rotary inertia can be significant for short CNTs, Bresse-Timoshenko beam theory is commonly used to investigate the vibrational characteristics because the Bresse-Timoshenko beam theory is more accure than the Euler–Bernoulli beam theory. In the Euler – Bernoulli beam model, the cross-section of beam was perpendicular to the neutral axis, whereas this assumption was removed in the Bresse-Timoshenko beam model to account for the shear and rotary effects. The Bresse-Timoshenko theory was normally able to provide more accurate wave solution at higher wave, although it was more complicated than the Euler–Bernoulli theory [37]. By comparing the results obtained from the Bresse-Timoshenko and Euler–Bernoulli beam theories, they showed that the frequencies are significantly over predicted by the Euler–Bernoulli beam theory for smaller length-to-diameter ratios and higher vibration modes. For vibration analysis of one-dimensional beam-like structures, Euler–Bernoulli beam model and Bresse-Timoshenko beam model were usually employed, which assumed that the cross-section of beams remained plane under bending deformation [37, 45].

1.4.4 Three-dimensional elastic shell model

Elastic continuum shell model have been effectively used to study the vibration in CNTs. From Figure 1.5, we can see the simplification process of model of CNTs' structure. However, the analysis of vibration characteristics of cylindrical shells is more complex than that of beams and plates. This is mainly because the motion equations of cylindrical shells together with boundary conditions are more complex. Love modified the Kirchhoff hypothesis for plates and established the preconditions of the so-called classic theory of thin shells, which is now commonly known as Love's first approximation of the first kind. He then subsequently formulated a shell theory known as Love's first approximation theory and the preconditions he established soon became the foundations on which many thin shell theories were later developed, like Donnell and Flügge theory [59]. Incorporating the constitutive relations and equilibrium state equation, they obtained a set of three expressions for analyzing the vibration of CNTs.

In this thesis, we aim at doing the dynamic analysis of CNTs based on continuum mechanical models mentioned above. Firstly, to get the mechanical properties of CNTs, and then based on that to build three models of CNTs for analysis the vibrational behavior of SWCNTs and double-walled carbon nanotubes (DWCNTs) in different conditions. We firstly get the theoretical analysis on vibrational behavour of CNTs to prediction the available results on nanotechnoledgy.

1.5 Layout of this thesis

The thesis is organized to provide a snapshot of vibration of CNTs.

In chapter 1, generally introduces the mechanical property of CNTs, especially force on the vibration property using continuum mechanical model.

In chapter 2, the mechanical properties of both armchair and zigzag SWCNTs are

characterized by using continuum mechanics in the atomic scale. I predict Young's modulus and Poisson's ratio of SWNCTs.

In chapter 3, an analytical procedure based on the Euler-Bernoulli beam model was used to characterize the resonant frequency of cantilevered DWCNTs embedded in matrix and DWCNTs with inner and outer nanotubes of different lengths.

In chapter 4, an analytical procedure based on the nonlocal Bresse-Timoshenko beam mode was used to investigate the vibrational behavior of DWCNTs adhered by surface materials and embedded in elastic media.

In chapter 5, based on elastic shell continuum mechanics, we studied the RBM frequency of simply-supported CNTs exposed to radial pressure and axial pressure.

In Chapter 6, presents a summary of the research and offers some overall conclusions.

References

[1] H. W. Kroto, J. R. Heath, S. C. O'Brien, R. F. Curl, R. E. Smalley, Nature **318**, 162 (1985)

[2] R. P. Feynman, Eng. Sci. **23**, 22 (1960)

[3] A. Oberlin, M. Endo, J. Cryst. Growth **32**, 335 (1976)

[4] Michael J. O' Connell, Carbon Nantubes: Properties and Applications, Theranos, Inc. Menlo Park, California, 2006 America

[5] S. Iijima, Nature **354**, 56 (1991)

[6] M. Terrones, Annu. Rev. Mater. Res. **33**, 419 (2003)

[7] H. N, S. Sawada, A. Oshiyama. Phys. Rev. Lett. **68**, 1579 (1992)

[8] R. Saito, M. Fujita, G. Dresselhaus, M. S. Dresselhaus, Phys. Rev. B **46**, 1804 (1992)

[9] R. Saito, M. Fujita, G. Dresselhaus, M. S. Dresselhaus, Appl. Phys. Lett. **60**, 2204 (1992)

[10] Y. Y. Liu, X. W. Wang, K. H. Qi, J. H. Xin, J. Mater. Chem. **18**, 3454 (2008)

[11] J. N. Coleman, U. Khan, Y. K. Gun'ko, Adv. Mater. **18**, 689 (2006)

[12] J. N. Coleman, U. Khan, W. Y. Blau, Y. K. Gun'ko, Carbon **44**, 1624 (2006)

[13] R. Saito, H. Kataura: Optical Properties and Raman Spectroscopy of Carbon Nanotubes in "Carbon Nanotubes", Springer-Verlag, Berlin, (2001)

[14] A. W. Moore, Chem. Phys. Carbon **104**, 69 (1973)

[15] C. H. Olk, J. P. Heremans, J. Mater. Res. **9**, 259 (1994)

[16] J. Tersoff, R. S. Ruoff, Phys. Rev. Lett. **73**, 676 (1994).

[17] A. Loiseau, P. Launois, P. Petit, S. Roche, J. -P. Salvetat. Understanding Carbon Nanotubes from Basics to Application. Springer-Verlag Berlin Heidelberg. 2006.

[18] M. S. Dresselhaus, P. Avouris, Appl. Phys. **80**, 1 (2001)

[19] M. Endo, S. Iijima, M.S. Dresselhaus, Carbon nanotubes. Reprinted Carbon, 33,1996

[20] http://www.seas.upenn.edu/mse/research/nanotubes.html.

[21] P. Ball, Nature (London) **414**, 142 (2001).

[22] R. H. Baughman, A. A. Zakhidov, W. A. de Heer, Science **297**, 787 (2002).

[23] E. T. Thostenson, Z. Ren, T. W. Chou, Compos. Sci. Tech. **61**, 1899 (2001).

[24] L. S. Schadler, S. C. Giannaris, P. M. Ajayan, Appl. Phys. Lett. **73**, 3842 (1998).

[25] M. M. J. Treacy, T. W. Ebbesen, J. M. Gibson, Nature **381**, 678 (1996).

[26] E. W. Wong, P. E. Sheehan, C. M. Lieber, Science **277**, 1971 (1997).

[27] T. Natsuki, K. Tantrakarn, M. Endo, Carbon **42**, 39 (2004).

[28] O. Lourie, H. D. Wagner, J. Mater. Res. **13**, 2418 (1998).

[29] M. F. Yu, B. S. Files, S. Arepalli, R. S. Ruoff, Phys. Rev. Lett. **84**, 5552 (2000).

[30] M. F. Yu, O. Lourie, M. J. Dyer, K. Moloni, T. F. Kelly, R.S. Ruoff, Science **287**, 637 (2000).

[31] E.W. Wong, P.E. Sheehan, C.M. Lieber, Science **277**, 1971 (1997).

[32] J. P. Salvetat, A.J. Kulik, J.M. Bonard, G.A.D. Briggs, T. Stockli, K. Metenier, S. Bonnamy, F. Beguin, N.A. Burnham, L. Forro, Adv. Mater. **11**, 161 (1999).

[33] J. P. Salvetat, G.A.D. Briggs, J.M. Bonard, R.R. Bacsa, A.J. Kulik, T. Stockli, N. A. Burnham, L. Forro, Phys. Rev. Lett. **82**, 944 (1999).

[34] Z. W. Pan, S. S. Xie, L. Lu, B. H. Chang, L. F. Sun, W. Y. Zhou, G. Wang, D. L. Zhang, Appl. Phys. Lett. **74**, 3152 (1999).

[35] D. R. Lide, 1994, CRC Handbook of Chemistry and Physics, 75th ed., CRC, Boca Raton, FL.

[36] C. M. Wang, Y. Y. Zhang, Y. Xiang, J. N. Reddy. Appl. Mech. Rev. **63**, 030804 (2010)

[37] Q. Wang, V. K. Varadan, Int. J. Solids Struct. **43**, 254 (2006).

[38] R. F. Gibson, E. O. Ayorinde, Y. F. Wen, Compos. Sci. Technol. **67**, 1 (2007).

[39] C. Y. Wang, C. Q. Ru, A. Mioduchowski, Phys. Rev. B **72**, 075414 (2005).

[40] T. Natsuki, Q. Q. Ni, M. Endo, Carbon **46**, 1570 (2008).

[41] P. Poncharal, Z. L. Wang, D. Ugarte, W. A. de Heer, Science **283**, 1513 (1999).

[42] A. Krishnan, E. Dujardin, T. W. Ebbesen, P. N. Yianilos, M. M. J. Treacy, Phys. Rev. B **58**, 14013 (1998).

[43] Q. Wang, V.K. Varadan, Int. J. Solids Struct. **43**, 254 (2006).

[44] L. L. Ke, Y. Xiang, J. Yang, S. Kitipornchai, Comput. Mater. Sci. **47**, 409 (2009).

[45] C. M. Wang, V. B. C. Tan, Y. Y. Zhang, J. Sound Vib. **294**, 1060 (2006).

[46] J. Yoon, C. Q. Ru, A. Mioduchowski, Composites: Part B **35**, 87 (2004).

[47] J. C. Hsu, H. L. Lee, W. J. Chang, Nanotechnology, **18**, 285503 (2007)

[48] Q. Wang, B. I. Yakobson, K. M. Liew, Recent developments on modeling and applications of carbon nanotubes, 2009 Kerala, India.

[49] I. Elishakoff, D. Pentaras, K. Dujat, C.Versaci, G. Muscolino, J. Storch, S. Bucas, N. Challamel, T. Natsuki, Y. Y. Zhang, C. M. Wang, G. Ghyselinck. Carbon Nanotubes and Nanosensors: Vibrations, Buckling, and Ballistic Impact. May 3, 2011.

[50] C. Q. Ru, J Appl. Phys. **87**, 1712 (2000).

[51] C. Q. Ru, Phys. Rev. B **62,** 9973 (2000).

[52] C. Q. Ru, Phys. Rev. B **62**, 10405 (2000).

[53] C. Q. Ru, J. Mech. Phy. Solids **49**, 1265 (2001).

[54] C. Q. Ru, J Appl. Phys. **89**, 3426 (2001).

[55] Gregory M. Odegarda, Thomas S. Gatesb, Lee M. Nicholsonc, Kristopher E. Wised, Compos. Sci. Technol. **62**, 1869 (2002).

[56] C. Y. Li, T. W. Chou, Int. J. Solids Struct. **40**, 2487 (2003)

[57] Y. M. Ghugal, R. P. Shimpi. J. Reinf. Plast. Compos. **20**, 255 (2001)

[58] K. T. Lau, M. Chipara, H. Y. Ling, D. Hui, Compos. Part B **35**, 95 (2004)

[59] S. P. Timoshenko, J.M. Gere, Theory of Elastic Stability, second ed., McGraw–Hill, New York, 1961.

CHAPTER TWO

Analysis of Carbon Nanotubes on the Mechanical Properties at Atomic Scale

2 Analysis of carbon nanotubes on the mechanical properties at atomic scale

2.1 Introduction

Since the discovery by Iijima in 1991 [1], carbon nanotubes (CNTs) have generated huge activities in most areas of science and engineering due to their unprecedented mechanical, electrical and thermal properties [2-13]. Especially in mechanical field, experimental measurements have determined that CNTs possess excellent mechanical properties [14-21]. Therefore, the effective method to analyze the basic characteristics of nanosized CNTs is essential.

In the past, researchers used experimental method to measure mechanical properties of CNTs. Treacy et al. [14] firstly measured the amplitude of intrinsic thermal vibrations observed in transmission electron microscopy (TEM). The average value of Young's modulus of CNTs derived from this experimental technique is 1.8 TPa by 11 tubes, in which the lowest value and the highest value are 0.40 TPa and 4.15 TPa, respectively. Later, Poncheral et al. [18] obtained Young's modulus of CNTs which is between 0.7 and 1.3 TPa by electromechanical resonant vibrations. In addition, based on

an atomic force microscope (AFM), Wong et al. [20] in 1997 firstly directly measured the stiffness constant of armchair MWCNTs pinned at one end, from which the value of Young's modulus of CNTs is 1.28 TPa. Salvetat et al. [21] used the AFM for experiment of bending an armchair (Multi-walled carbon nanotubes) MWCNT pinned at each end over a hole and obtained an average modulus value of CNTs being 0.81 TPa. These experiments all promote the research of mechanical properties of CNTs. However, in description of nanoscale structures, the results are with experimental errors.

Meanwhile, for researching mechanical properties of CNTs, a number of scholars solved the difficulties in nanosized experiments in terms of computer simulation. For the analysis of nanostructural materials, atomic simulation methods such as first-principle quantum-mechanical methods [22], molecular dynamics (MD) [23, 24] and Monte Carlo [25] simulations have been routinely adopted. As early as 1993, Overney et al. [26] calculated the Young's modulus of rigid short SWCNTs which is 1.5 TPa, approximately equaling to that of graphite. This was followed by a range of papers predicting that the Young's modulus of CNTs is close to 1 TPa independent of type and diameter [27]. Yakobson et al. [28] fitted these results by MD simulations of the continuum shell model. Unlike the previous work that assumed a thickness of 0.34 nm, both the thickness and Young's modulus were taken as the fitting parameters, yielding a thickness of 0.066 nm and Young's modulus of 5.5 TPa. The MD approach was also used by Lu [27, 29] who reported Young's modulus is 1 TPa, and claimed that chirality and the number of walls have little effect on the value of Young's modulus. A different potential model was used by Yao et al. [16] who obtained Young's modulus of CNTs is 1 TPa. Although MD method has been widely used in simulating the properties of nanostructural materials, it is complex and time consuming, especially for large amount atomic systems. Therefore, the continuum mechanics seems to be a better way to investigate the properties of CNTs. However, for the case of nano-reinforced adhesives,

these models cannot accurately describe the influence of the relationship between carbon atoms upon the mechanical properties and their interactions in the composite systems because they lack the appropriate constitutive relations that govern material behavior at this scale [30]. Another modeling approach is the atomic-based continuum technique, which has the unique advantage of describing atomic structured properties in a continuum framework for reducing the computational demand while employing the appropriated atomic constitutive relations.

Therefore, there is a demand of developing a modeling technique that analyzes the mechanical properties of CNTs at the atomic scale. In this chapter, considering CNTs as a rolled cylindrical graphite sheet, we step from the Young's modulus of the *C-C* bonds counted as Euler beam at atomic scale and extend the theory of classical structural mechanics into the modeling of carbon graphite sheet. The effects of tube curvature on the mechanical properties of SWCNTs are considered in closed-form solutions. The mechanical properties of SWCNTs, including Young's modulus, Poisson's ratio, the length of *C-C* bonds and the angle between the adjacent *C-C* bonds are discussed as functions of nanosized structure.

2.2 The structure of CNTs

CNTs can be considered as graphite sheets rolled into cylindrical shape. The one-atom-thick graphite sheet looks like chicken wire which is made of a single carbon atom thickness. The structure of CNTs as shown in Figure 2.1 is conveniently explained in terms of the chiral vector integers (n, m) and the chiral angle θ [31],

$$\theta = \tan^{-1}\left(\frac{\sqrt{3}n}{2m+n}\right) \tag{2-1}$$

CNTs are classified into three categories named as zigzag (n, 0), $\theta_z = 0^o$; armchair (n,

n), $\theta_a = 30^o$; and chiral (n, m), $(m \neq n \neq 0)$. The relationship between radius r_{cnt} and integers (n, m) is expressed as

$$r_{cnt} = \frac{\sqrt{3}L_{cc}}{2\pi}\sqrt{n^2 + m^2 + mn} \tag{2-2}$$

where L_{cc} is the length of C-C bonds is 0.142 nm for SWCNTs.

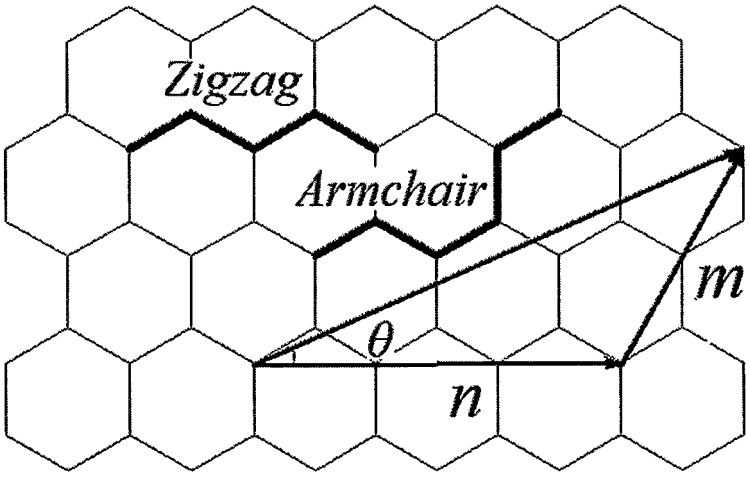

Figure 2.1 Schematic diagram of hexagonal graphite sheet

2.3 Mechanics model of graphite sheet

From the viewpoint of molecular mechanics, CNTs are treated as a large array of molecules consisting of carbon atoms. According to the Tersoff-Brenner force field theory [3, 32], the total molecular potential energy of the force field for nanostructured material can be defined as the sum of bonding and nonbonding energies,

$$V = \sum V_r + \sum V_\theta + \sum V_\varphi + \sum V_\omega + \sum V_{vdw} + \sum V_{el} \tag{2-3}$$

where V_r is the energy induced by bond stretch interaction, V_θ is the energy by the bond angle bending, V_φ is the energy by the dihedral angle torsion, V_ω is the energy by the improper torsion, V_{vdw} is the energy by the nonbonding van der Waals (vdW)

interaction, V_{el} is the energy by the electrostatic interaction. As the axial loading, improper torsion and nonbonding interactions subjected to CNTs are very small [33], for covalent systems, the main contributions to the total molecular potential energy comes from the first four terms of Eq. (2-3). Simplified system potential energy of CNTs with *C-C* bonds are given as,

$$V_r = \frac{1}{2}k_r(r - r_0)^2 = \frac{1}{2}k_r(\Delta r)^2 \tag{2-4a}$$

$$V_\theta = \frac{1}{2}k_\theta(\theta - \theta_0)^2 = \frac{1}{2}k_\theta(\Delta\theta)^2 \tag{2-4b}$$

$$V_\tau = V_\varphi + V_\omega = \frac{1}{2}k_\tau(\Delta\phi)^2 \tag{2-4c}$$

where k_r, k_θ and k_τ are the bond stretching, bond bending and torsional resistance constants, respectively, while Δr, $\Delta\theta$ and $\Delta\phi$ represent the bond stretching increment, the bond angle change, and the angle change of bond twisting, respectively.

According to classical structural mechanics, the strain energy of a uniform beam in graphite sheet are expressed as

$$U_l = \frac{EA}{2L_{cc}}(\Delta l)^2 \tag{2-5a}$$

$$U_\theta = \frac{EI}{2L_{cc}}(\Delta\theta)^2 \tag{2-5b}$$

$$U_\theta = \frac{GJ}{2L_{cc}}(\Delta\phi)^2 \tag{2-5c}$$

where EA is the tensile resistance of beam (*C-C* bonds), EI is the flexural rigidity, GJ is the torsional stiffness, Δl, $\Delta\theta$ and $\Delta\phi$ are the axial stretching deformation, the rotational angle at the end of the beam and the relative rotation between the ends of the beam, respectively.

Based on the energy conservation law, a linkage between the force constants in

molecular mechanics and the sectional stiffness parameters in structural mechanics are established. Eq. (2-4) and Eq. (2-5) equal to each others in one-to-one correspondending directions. The direct relationship between the structural mechanics parameters and the molecular mechanics parameters is deduced as follows,

$$EA = L_{cc} k_r \qquad EI = L_{cc} k_\theta \qquad GJ = L_{cc} k_\tau \tag{2-6}$$

As long as the force constants k_r, k_θ and k_τ are known, the sectional stiffness parameters EA, EI and GJ can be determined, then the deformation and elastic behavior of CNTs at atomic scale can be modeled. Further analysis of Eq. (2-4) and Eq. (2-5), three more constants of *C-C* bonds D (diameter of *C-C* bonds), E and G are depending on k_r, k_θ and k_τ,

$$D = 4\sqrt{\frac{k_\theta}{k_r}} \qquad E = \frac{k_r^2 L_{cc}}{4\pi k_\theta} \qquad G = \frac{k_r^2 k_\tau L_{cc}}{8\pi k_\theta^2} \tag{2-7}$$

2.3.1 Young's modulus for armchair graphite sheet

Knowledge of Young's modulus (*E*) is the first step towards the material using as a structural element for various applications. SWCNTs can be regarded as a two dimensional continuum shell model which is composed of the discrete molecular structures linked by the *C-C* bonds. The unrolled graphite sheet of armchair SWCNTs is shown in Figure. 2.2. Figure. 2.2 (*b*) plots the smallest unit of armchair graphite sheet, in which the force P_a and moment M_{a0} are displayed. The unit of armchair graphite sheet can be analyzed based on solid mechanics, and the unit along BD bond is symmetry on both structure and force. Therefore, in term of the elastic deformation energy, the energy of an armchair unit is written as

$$W_a = \frac{(P_a \sin\theta_a)^2 \times l_a}{2EA} + \int_0^{l_a} \frac{(P_a x \cos\theta_a - M_{a0})^2}{2EI} dx \tag{2-8}$$

where E is the Young's modulus of beam, l_a is the *C-C* bonds of armchair graphite sheet. When the relationship between force P_a and moment M_{a0} is determined, the strain of the unit can be resolved by using energy W_a.

According to the Castigliano's Law, the rotation angel on point *C* is zero due to symmetry on structure and force that is shown in Eq. (2-9),

$$\theta_{ac} = \frac{\partial W_a}{\partial M_{a0}} = 0 \tag{2-9}$$

Substituting Eq. (2-8) into Eq. (2-9), the relationship between force P_a and moment M_{a0} is obtained,

$$M_{a0} = \frac{P_a l_a}{2}\cos\theta_a \tag{2-10}$$

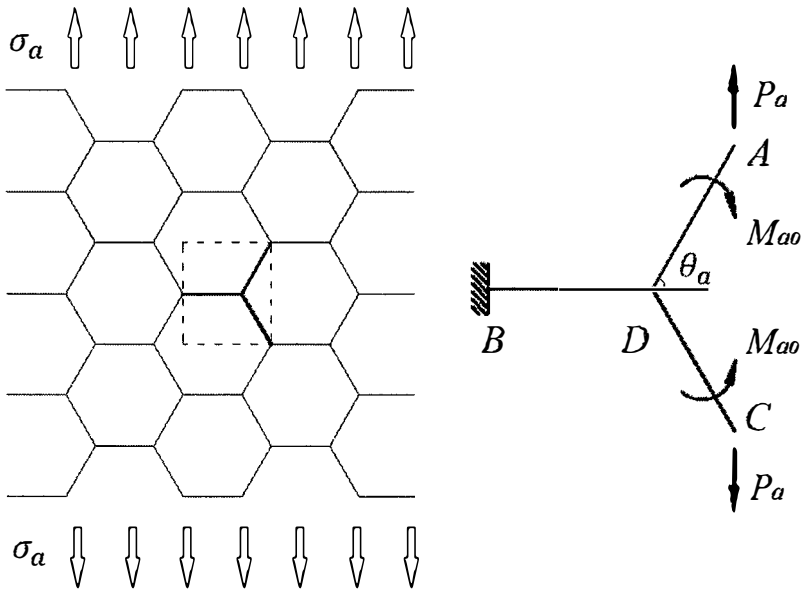

Figure 2.2 Force analysis of armchair graphite sheet unit subjected to axial tension loading

Meanwhile, the elastic deformation energy W_a is rewritten as follows,

$$W_a = \frac{P_a^2 l_a \sin^2 \theta_a}{2EA} + \frac{P_a^2 l_a^3 \cos^2 \theta_a}{24EI} \tag{2-11}$$

On basis of the Castigliano's Law, the displacement of the unit is defined by the elastic deformation energy differential Eq. (2-12),

$$\delta_a = \frac{\partial W_a}{\partial P_a} = \frac{P_a l_a \sin^2 \theta_a}{EA} + \frac{P_a l_a^3 \cos^2 \theta_a}{12EI} \tag{2-12}$$

and the strain of armchair graphite sheet is defined as follows,

$$\varepsilon_a = \frac{\delta_a}{l_a \sin \theta_a} \tag{2-13}$$

For an armchair graphite sheet being subjected to the tension stress σ_a, equation of static equilibrium of the unit are expressed as

$$\sigma_a t l_a (1 + \cos\theta_a) = P_a \tag{2-14}$$

Based on the Hooke's law, the relationship of the tension stress and the strain is,

$$\sigma_a = E_a \varepsilon_a \tag{2-15}$$

When $\theta_a = 60^0$, the Young's modulus of armchair graphite sheet E_a, which yields

$$E_a = \frac{\sqrt{3}E}{t}\left(\frac{9l_a}{4A} + \frac{l_a^3}{16I}\right)^{-1} \tag{2-16}$$

where t is the thickness of the graphite sheet.

2.3.2 Young's modulus for the zigzag graphite sheet

For a zigzag graphite sheet, the analysis approach is similar to that of an armchair graphite sheet. The unit of a zigzag graphite sheet is drawn in Figure 2.3, and the energy of the unit is in Eq. (2-17),

$$W_z = \frac{P_z^2 l_z}{EA}(\sin^2 \theta_z + 2) + \frac{P_z^2 l_z^3 \cos^2 \theta_z}{12EI} \tag{2-17}$$

where l_a is the *C-C* bonds of the zigzag graphite sheet. The displacement of the zigzag unit is defined as

$$\delta_z = \frac{P_z l_z}{EA}\left(\sin^2\theta_z + 2\right) + \frac{P_z l_z^3 \cos^2\theta_z}{12EI} \tag{2-18}$$

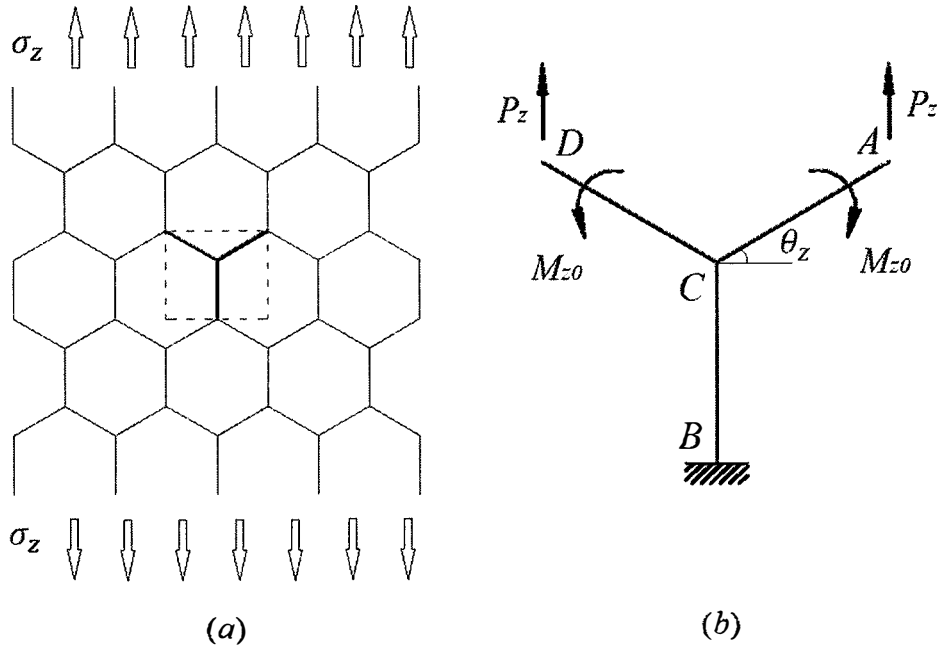

Figure 2.3 Force analysis of zigzag graphite sheet unit subjected to axial tension loading

Then the strain of per unit length is obtained as follows,

$$\varepsilon_z = \frac{\delta_z}{l_z\left(\sin\theta_z + 1\right)} \tag{2-19}$$

For a zigzag graphite sheet being subjected to the tension stress σ_z, the force acting on the unit can be written as

$$\sigma_z td\cos\theta_z = P_z \tag{2-20}$$

When $\theta_z = 30^0$, we can obtain the Young's modulus E_z of zigzag graphite sheet,

$$E_a = \frac{\sqrt{3}E}{t}\left(\frac{9l_z}{4A} + \frac{l_z^3}{16I}\right)^{-1} \tag{2-21}$$

2.4 Molecular mechanics model of SWCNTs

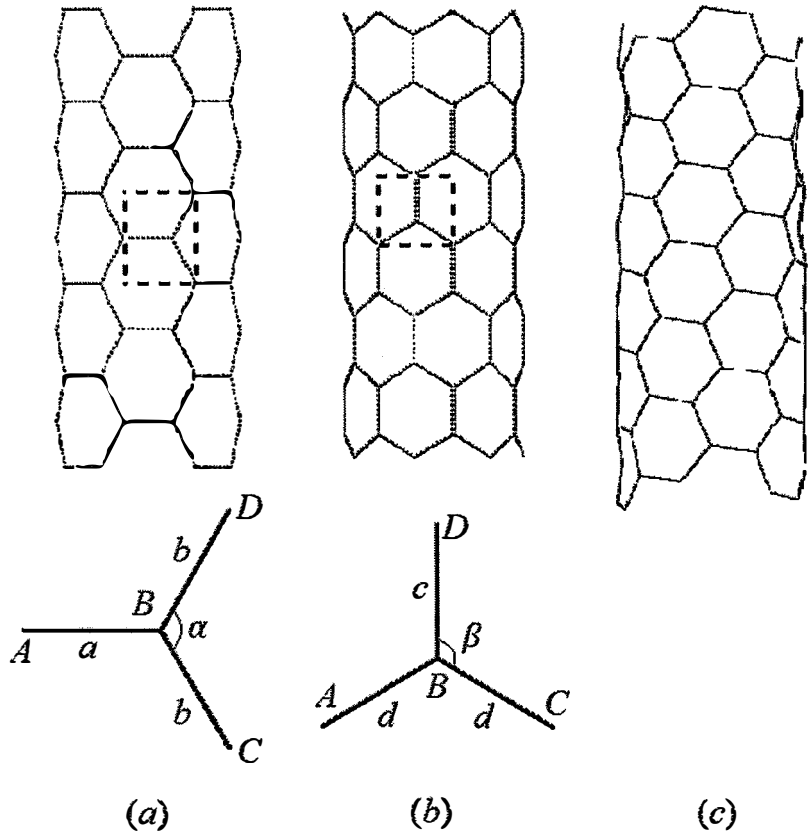

Figure 2.4 Classification of SWCNTs by chiral vector and chiral angle (a) armchair SWCNT, (b) zigzag SWCNT, (c) chiral SWCNT

SWCNTs can be ideally constructed starting from a graphite sheet. According to the chiral vector, there are three kinds of structure, as shown in Figure 2.4. After the two dimensional sheet rolled into a three dimensional tube, intrinsic properties of the structure will be changed, such as mechanical and physical characteristics.

2.4.1 Angle measurement for SWCNTs

Figure 2.4 (*a*) shows an armchair SWCNT. According to Eq. (2-2) the radius of armchair SWCNTs is $r_{acnt} = 3n \cdot L_{cc}/2\pi$. Meanwhile, by geometric relationships in cylindrical coordinates shown in Figure 2.4 (*a*), we obtain the coordinates of carbon atoms:

$$A = \left(r_{acnt},\ 0,\ 0\right) \tag{2-22a}$$

$$B = \left(r_{acnt}\cos\frac{2\pi}{3n},\ r_{acnt}\sin\frac{2\pi}{3n},\ 0\right) \tag{2-22b}$$

$$C = \left(r_{acnt}\cos\frac{\pi}{n},\ r_{acnt}\sin\frac{\pi}{n},\ -\frac{\sqrt{3}}{2}L_{cc}\right) \tag{2-22c}$$

$$D = \left(r_{acnt}\cos\frac{\pi}{n},\ r_{acnt}\sin\frac{\pi}{n},\ \frac{\sqrt{3}}{2}L_{cc}\right) \tag{2-22d}$$

Because of the effect of curvature, the lengths of the bonds between carbon atoms in vector space are shorter than those in plane and characterized in different numerical values, which are displayed in Figure 2.4 (*a*) and given as follows:

$$a = \left|\overrightarrow{BA}\right| = \frac{3n}{2\pi}\sqrt{2-2\cos\frac{2\pi}{3n}}L_{cc} \tag{2-23a}$$

$$b = \left|\overrightarrow{BD}\right| = \left|\overrightarrow{BC}\right| = \frac{3n}{2\pi}\sqrt{2-2\cos\frac{\pi}{3n}+\frac{\pi^2}{3n^2}}L_{cc} \tag{2-23b}$$

In cylindrical coordinates, on account of the curvature, the included angles between the adjacent bonds in a carboncycle of SWCNTs are different from that of graphite sheets. In accordance with geometrical relationships, the included angle between the adjacent bonds for an arbitrary unit of armchair SWCNTs plotted in Figure 2.4 (*a*) relates with coordinate figures of carbon atoms in the unit,

$$\cos\alpha = \frac{\overrightarrow{BD}\cdot\overrightarrow{BC}}{\left|\overrightarrow{BD}\right|\left|\overrightarrow{BC}\right|} \tag{2-24}$$

Substituting Eq. (2-23) into Eq. (2-24), we obtain the included angle of armchair SWCNTs

$$\alpha = \cos^{-1}\left(\frac{6n^2\left(1-\cos\frac{\pi}{3n}\right)-\pi^2}{6n^2\left(1-\cos\frac{\pi}{3n}\right)+\pi^2} \right) \tag{2-25}$$

Figure 2.4 (*b*) shows a zigzag SWCNT. According to Eq. (2-2) the radius of zigzag SWCNTs is $r_{zcnt} = \sqrt{3}n \cdot L_{cc}/2\pi$. Considered of geometric relationships in cylindrical coordinates, the coordinate figures are described as

$$A = \left(r_{zcnt},\ 0,\ 0\right) \tag{2-26a}$$

$$B = \left(r_{zcnt}\cos\frac{\pi}{n},\ r_{zcnt}\sin\frac{\pi}{n},\ \frac{1}{2}L_{cc} \right) \tag{2-26b}$$

$$C = \left(r_{zcnt}\cos\frac{2\pi}{n},\ r_{zcnt}\sin\frac{2\pi}{n},\ 0 \right) \tag{2-26c}$$

$$D = \left(r_{zcnt}\cos\frac{\pi}{n},\ r_{zcnt}\sin\frac{\pi}{n},\ \frac{3}{2}L_{cc} \right) \tag{2-26d}$$

The distances of the bonds in vector space are as follows,

$$c = \left|\overrightarrow{BD}\right| = L_{cc} \tag{2-27a}$$

$$d = \left|\overrightarrow{BA}\right| = \left|\overrightarrow{BC}\right| = \frac{\sqrt{3}n}{2\pi}\sqrt{2-2\cos\frac{\pi}{3n}+\frac{\pi^2}{3n^2}}L_{cc} \tag{2-27b}$$

For zigzag SWCNTs, the analysis method resembles armchair SWCNTs, we calculate the included angle for zigzag SWCNTs as following,

$$\beta = \cos^{-1}\left(\frac{-\pi}{\sqrt{6n^2\left(1-\cos\frac{\pi}{n}\right)+\pi^2}} \right) \tag{2-28}$$

2.4.2 Elastic properties for SWCNTs

Considered of space curvature, the Young's modulus of SWCNTs in cylindrical coordinates depends on bond length and included angle between two bonds. The method for calculating Young's modulus of armchair SWCNTs in three dimensions resembles that in two dimensions. Effecting factors in three dimensional coordinates of the Young's modulus of armchair SWCNTs are mentioned in Eq. (2-23) and Eq. (2-25), the Young's modulus of armchair SWCNTs is expressed in Eq. (2-29),

$$E_{acnt} = \xi\lambda_a\left(k_{a1}\frac{1}{A} + k_{a2}\frac{1}{12I}\right)^{-1} \tag{2-29}$$

where $\xi = \frac{E}{t}$, $\lambda_a = \frac{\sin\frac{\alpha}{2}}{a + b\cos\frac{a}{2}}$, $k_{a1} = \sin^2\frac{\alpha}{2}$ and $k_{a2} = b^2\cos^2\frac{\alpha}{2}$.

We obtain the Young's modulus of zigzag SWCNTs given in Eq. (2-30) in the same way,

$$E_{zcnt} = \xi\lambda_z\left(k_{z1}\frac{1}{A} + k_{z2}\frac{1}{12I}\right)^{-1} \tag{2-30}$$

where $\lambda_z = \frac{d\sin\left(\beta - \frac{\pi}{2}\right) + c}{d\cos\left(\beta - \frac{\pi}{2}\right)}$, $k_{z1} = d\sin^2\left(\beta - \frac{\pi}{2}\right) + 2c$ and $k_{z2} = \cos^2\left(\beta - \frac{\pi}{2}\right)d^3$.

2.4.3 Poisson's ratio for SWCNTs

For armchair SWCNTs, the stretch deformations of the bonds caused by force and bending moment are schematically signed in Figure 2.5 (*a*) to analyze the Poisson's ratio. The equilibrium of force P_a and bending moment M_a can be computed from Figure 2.5 (*a*),

$$2M_a = P_a b\sin\frac{\alpha}{2} \tag{2-31}$$

According to geometric properties and elastic theory, taking the included angle between two bonds in three dimensions into consideration, we obtain the equilibrium equations about extension variation of the *C-C* bonds,

$$\delta_a^{P1} = \frac{P_a \sin\frac{\alpha}{2}}{EA} \tag{2-32a}$$

$$\delta_a^{P2} = \frac{P_a b^3 \cos\frac{\alpha}{2}}{3EI} \tag{2-32b}$$

$$\delta_a^{M} = -\frac{M_a b^2 \cos\frac{\alpha}{2}}{2EI} \tag{2-32c}$$

where EA and EI are the tensile resistance and the flexural rigidity of beam, δ_a^{P1}, δ_a^{P2} and δ_a^{M} are the deformations of beam caused by force P_a and bending moment M_a, respectively. The strains in axial direction and circumferential direction are defined as follows, respectively,

$$\varepsilon_{a1} = \frac{\delta_a^{P1}\cos\frac{\alpha}{2} - \left(\delta_a^{P2} + \delta_a^{M}\right)\sin\frac{\alpha}{2}}{a + b\cos\frac{\alpha}{2}} \tag{2-33a}$$

$$\varepsilon_{a2} = \frac{\delta_a^{P1}\sin\frac{\alpha}{2} + \left(\delta_a^{P2} + \delta_a^{M}\right)\cos\frac{\alpha}{2}}{b\sin\frac{\alpha}{2}} \tag{2-33b}$$

Poisson's ratio of armchair SWCNTs can be defined as the ratio between circumferential strain and axial strain, substituting Eq. (2-31) and Eq. (2-32) into Eq. (2-33) we can get Poisson's ratio of armchair SWCNTs,

$$\nu_a = \frac{\varepsilon_{a1}}{\varepsilon_{a2}} = -\frac{\left(12I - Ab^3\right)\sin^2\frac{\alpha}{2}\cos\frac{\alpha}{2}}{\left(12I\sin^2\frac{\alpha}{2} + Ab^3\cos^2\frac{\alpha}{2}\right)\left(\frac{a}{b} + \cos\frac{\alpha}{2}\right)} \tag{2-34}$$

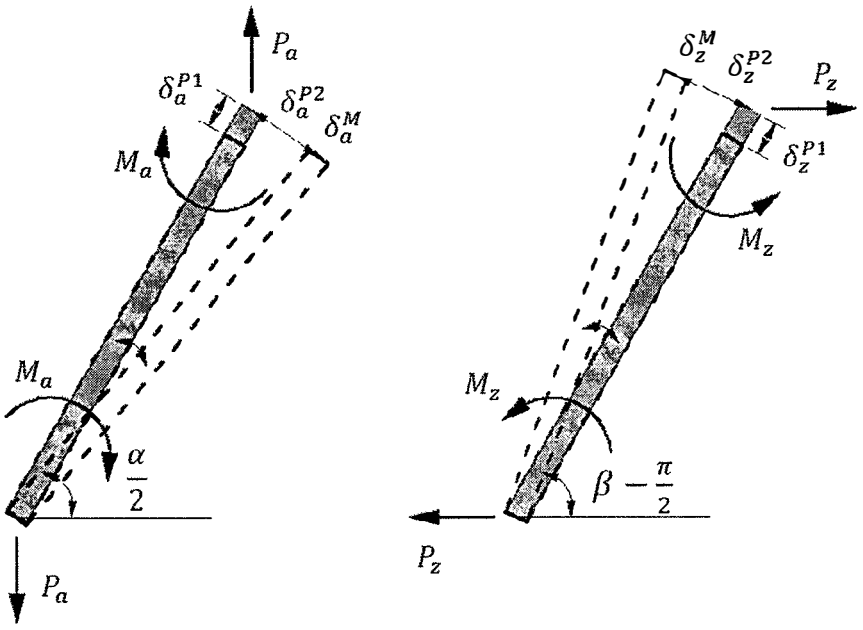

(*a*) (*b*)

Figure 2.5 Analysis of axial deformation and angular displacement of armchair and zigzag SWCNTs

For zigzag SWCNTs, the analysis step is similar to armchair SWCNTs. To analyze the Poisson's ratio of zigzag SWCNTs, Figure 2.5 (*b*) schematically signs the stretch deformations of the bonds caused by force P_z and bending moment M_z, the relationship of force and bending moment is given in Eq. (2-35),

$$2M_z = P_z b \sin\frac{\alpha}{2} \tag{2-35}$$

The equilibrium equations about extension variation of the bond are described as

$$\delta_z^{P1} = \frac{P_z \sin\left(\beta - \frac{\pi}{2}\right)}{EA} \tag{2-36a}$$

$$\delta_z^{P2} = \frac{P_z d^3 \cos\left(\beta - \frac{\pi}{2}\right)}{3EI} \tag{2-36b}$$

$$\delta_z^{P3} = \frac{2P_z \sin\left(\beta - \frac{\pi}{2}\right)}{EA} \tag{2-36c}$$

$$\delta_z^{M} = -\frac{M_z d^2 \cos\left(\beta - \frac{\pi}{2}\right)}{2EI} \tag{2-36d}$$

The strains in axial direction and circumferential direction are defined as following, respectively,

$$\varepsilon_{z1} = \frac{\delta_z^{P1} \cos\left(\beta - \frac{\pi}{2}\right) - \left(\delta_z^{P2} + \delta_z^{M}\right)\sin\left(\beta - \frac{\pi}{2}\right)}{d\cos(\pi - \beta)} \tag{2-37a}$$

$$\varepsilon_{z2} = \frac{\delta_z^{P1} \sin\left(\beta - \frac{\pi}{2}\right) + \left(\delta_z^{P2} + \delta_z^{M}\right)\cos\left(\beta - \frac{\pi}{2}\right) + \delta_z^{P3}}{c + d\sin(\pi - \beta)} \tag{2-37b}$$

Poisson's ratio of armchair SWCNTs can be defined as the ratio between circumferential strain and axial strain, then we obtain

$$\nu_z = \frac{\varepsilon_{z1}}{\varepsilon_{z2}} = \frac{\left(12I - Ab^3\right)\left(\frac{c}{d} + \sin\left(\beta - \frac{\pi}{2}\right)\right)\sin\left(\beta - \frac{\pi}{2}\right)}{\left(12I\sin^2\left(\beta - \frac{\pi}{2}\right) + Ad^3\cos^2\left(\beta - \frac{\pi}{2}\right) + 24A\right)} \tag{2-38}$$

2.5 Results and discussions

The atomic-based continuum mechanics approach described in the previous section has been implemented for studying the effective elastic properties of graphite sheets and SWCNTs. In this section, we examine the mechanical characteristics of graphite sheet have been determined at first.

2.5.1 Mechanics model of graphite sheet

In the present simulation, $k_r/2 = 46\,900 kcal/mole/nm^2$, $k_\theta/2 = 63 kcal/mole/$

$rad^2$and $k_\tau/2 = 20kcal/mole/rad^2$ are taken [34]. L_{cc} and t are 0.142 nm and 0.34 nm, respectively. According to Eq. (2-6) and Eq. (2-7), the constants of beam are obtained and summarized in Table 1. Compare the evaluated elastic moduli of graphite sheets with the literature results, Tserpes [8] and Kalamkarov [9] reported $E = 5.49$ TPa and $G = 0.871$ TPa, $E = 5.488$ TPa and $G = 0.8711$ TPa of *C-C* bonds, respectively.

Beam Element	Abbreviation	Value	Unit
Diameter	D	0.146	nm
Cross section area	A	$1.678\ 10^{-2}$	nm^2
Moment of inertia	I	$2.241\ 10^{-5}$	nm^4
Young's modulus	E	5.530	TPa
Shear elastic modulus	G	0.871	TPa

Table 2.1 Geometrical and material properties of *C-C* bonds

Comparing Eq. (2-16) to Eq. (2-21), Young's moduli of the armchair graphite sheet and the zigzag graphite sheet have the same expression form except for l_a and l_z. Because the carboncycle is a regular hexagon, graphite sheets have $l_a = l_z = L_{cc}$. We obtain the Young's moduli of both armchair and zigzag graphite sheets are 1.0424 TPa, which is close to the value of 1.033 TPa calculated by Li et al. [31] and the value of 1.04 TPa computed by Shokrieh [11]. It can be seen that the predicted values obtained from the model at the atomic scale agree well with those reported in literatures.

2.5.2 Molecular mechanics model of SWCNTs

Since SWCNTs are defined as rolled graphite sheets, the lengths of bonds in vector

space are changed owing to the effect of curvature. For armchair SWCNTs rolled by armchair graphite sheets, all of the lengths of *C-C* bonds become shorter because of the connection with curvature in circumferential direction. While, for zigzag SWCNTs rolled by zigzag graphite sheet, the length c is only in vertical direction equaling to the *C-C* bonds length of graphite sheets. According to Eq. (2-23) and Eq. (2-27), the variation of *C-C* bonds lengths with radius are shown in Figure 2.6. With increasing radius of SWCNTs, the bond lengths a, b and d approach to the length $c = 0.142nm$ which is the bond length of graphite itself, owing to the curvature approaching to zero in infinite radius.

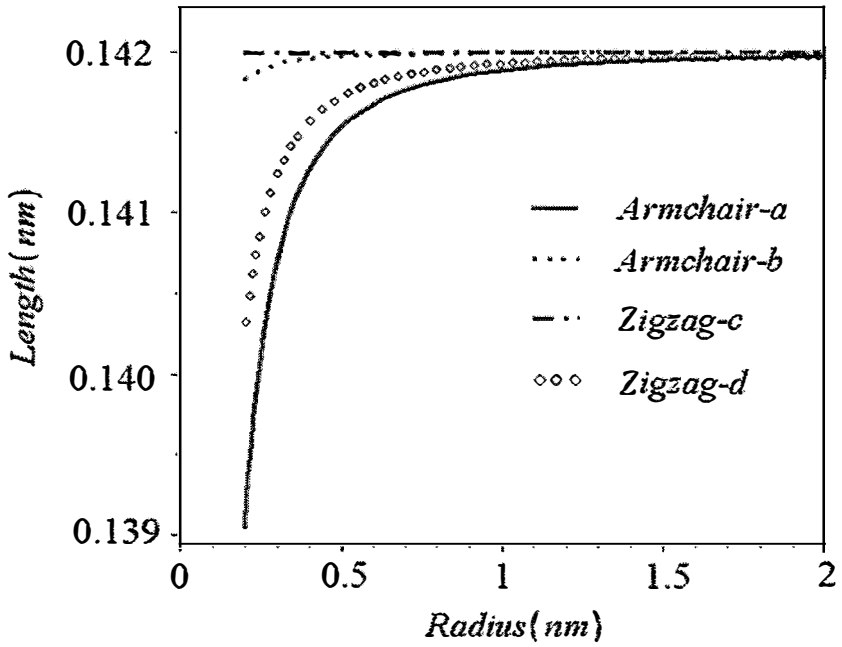

Figure 2.6 *C-C* bonds lengths of armchair SWCNTs and zigzag SWCNTs

When graphite sheets rolled into SWCNTs, the lengths and spatial relations of *C-C* bonds change obviously. Figure 2.7 shows the variation of included angle of two adjacent *C-C* bonds with radius according to Eq. (2-25) and Eq. (2-28). It expresses that the included angles are quite sensitive to SWCNTs in small radius. The included angle

of zigzag SWCNTs is a little larger than that of armchair SWCNTs in the same radius. As being larger than 1.1 nm, the radius makes less influence on the included angles of both armchair and zigzag SWCNTs, and the two lines show a tendency to be 120 degree which is nearly to that of graphite sheets, due to the SWCNTs being regarded as graphite sheet when radius is infinite.

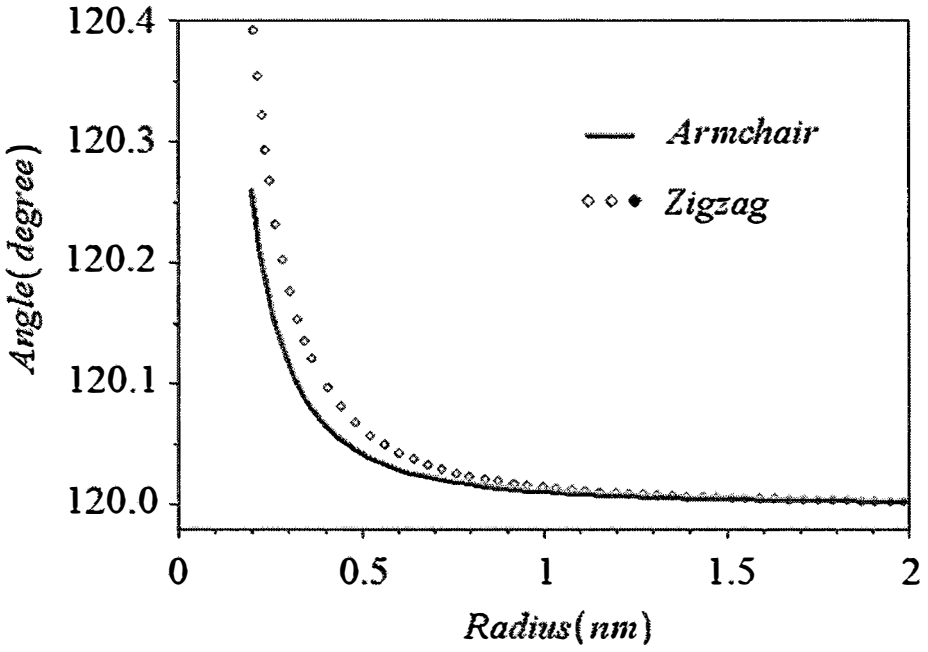

Figure 2.7 Included angles of adjacent *C-C* bonds in armchair SWCNTs and zigzag SWCNTs

Comparing Eq. (2-29) to Eq. (2-30), Young's moduli of armchair and zigzag SWCNTs have the same expression form except for coefficients λ_a, k_{a1}, k_{a2} and λ_z, k_{z1}, k_{z2}. As the two Young's moduli shown in Figure 2.8, the Young's moduli predicted by the present theory decrease monotonically with the increase of radius. The Young's modulus of armchair SWCNTs is slightly higher than that of zigzag SWCNTs in the same smaller radius. When the radius is larger, the two declining curves gradually develop into horizontal lines, which tend to be a constant of 1.0424 TPa. The value is

the Young's modulus of graphite sheet.

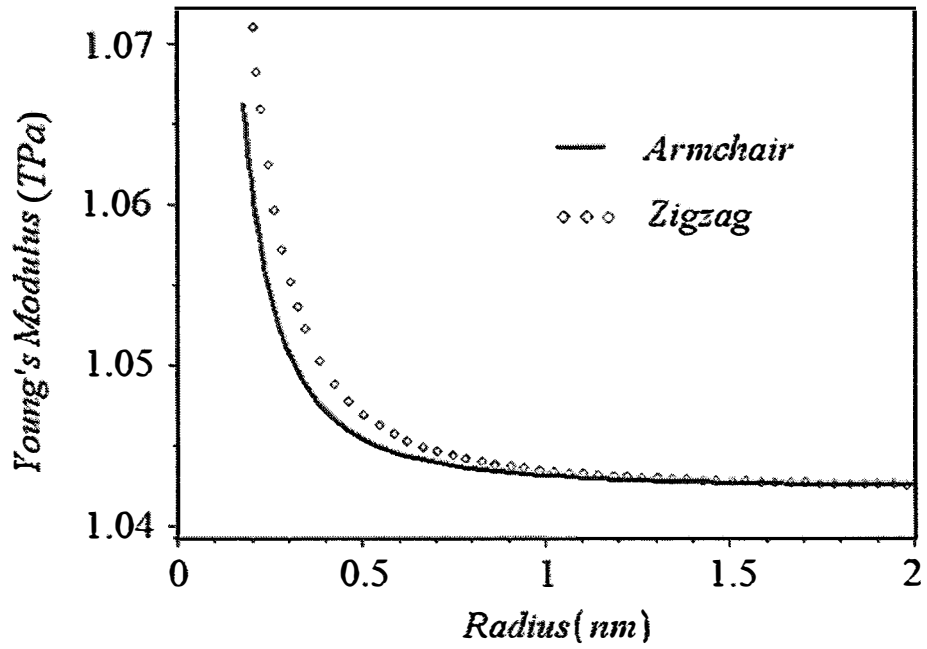

Figure 2.8 Young's modulus of armchair SWCNTs and zigzag SWCNTs

Considering the variations of length and included angles of two adjacent *C-C* bonds, from graphite sheets into SWCNTs, Figure 2.9 shows the variations of Poisson's ratio of the armchair and zigzag SWCNTs as a function of nanotube radius. It is found that, in general, the Poisson's ratio of armchair SWCNTs is slightly higher than that of zigzag SWCNTs. Poisson's ratios of armchair and zigzag SWCNTs show a smoothly monotonic decreasing versus increasing radius. When the radius of SWCNTs is larger, the two curves towards to be a straight line that means the Poisson's ratios approach to be a steady value of 0.26, which makes a great agreement with those reported in literatures [6, 33].

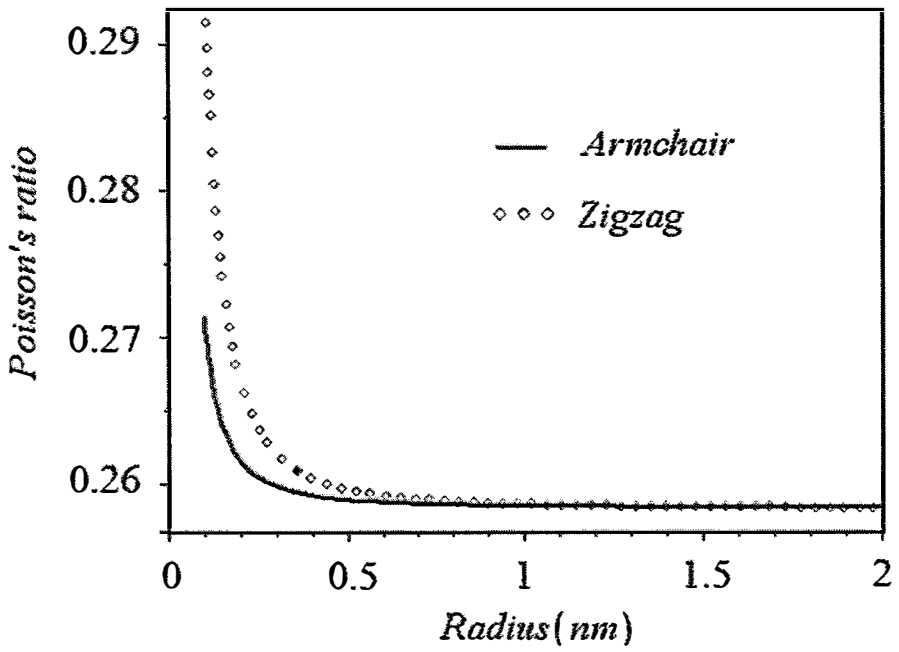

Figure 2.9 Poisson's ratio of armchair SWCNTs and zigzag SWCNTs

2.6 Conclusions

The mechanical properties of both armchair and zigzag SWCNTs are characterized by using continuum mechanics in the atomic scale. In term of the conjunction of Tersoff-Brenner force field method and energy conservation law, the graphite sheet is of isotropic property and the Young's modulus of graphite sheet is obtained to be 1.04 TPa. Furthermore, considering the variations of the length and the included angle of two adjacent *C-C* bonds rolled from graphite sheets into SWCNTs, Young's modulus and Poisson's ratio of SWNCTs with armchair and zigzag structures are investigated as a function of SWCNT radius. We predict Young's modulus and Poisson's ratio of SWNCTs are influenced obviously by relatively smaller radius, while little affected by larger radius. We are confident that this model provides a useful method to analyze mechanical properties of CNTs and other nanosized structures at the atomic scale.

References

[1] S. Iijima, Nature **354**, 56 (1991)

[2] F. Li, H. M. Cheng, S. Bai, G. Su, Appl. Phys. Lett. **77**, 3161 (2000)

[3] W. H. Chen, H.C. Cheng, Y. L. Liu, Comput. Mater. Sci. **47**, 985 (2010)

[4] Z. Spitalskya, D. Tasisb, K. Papagelisb, C. Galiotis, Prog. Polym. Sci. **35**, 357 (2010)

[5] M. A. Lo´pez Manchado, L. Valentini, J. Biagiotti, J. M. Kenny, Carbon, **43**, 1499 (2005)

[6] T. Natsuki, K. Tantrakarn, M. Endo, Appl. Phys. A, **79**, 117 (2004)

[7] M. R. Falvo, G. J. Clary, R. M. Taylor II, V. Chi, F. P. Brooks Jr, S. Washburn and R. Superfine. Nature **389**, 582 (1997)

[8] K. I. Tserpesa, P. Papanikos, Compos. Part B **36** 468 (2005)

[9] A. L. Kalamkarov, A. V. Georgiades, S. K. Rokkam, V. P. Veedu, M. N. Ghasemi-Nejhad, Int. J. Solids Struct. **43**, 6832 (2006)

[10] O. L. Blakslee, D. G. Proctor, E. J. Selden, G. B. Spence, T. Weng, J. Appl. Phys. **41**, 3373 (1970)

[11] M. M. Shokrieh, R. Rafiee, Mater. Des. **31**, 790 (2010)

[12] K. N. Kudin, G. E. Scuseria, B. I. Yakobson, Phys. Rev. B **64**, 235406 (2001)

[13] O. Lourie, H. D. Wagner, J. Mater. Res. **13**, 2418 (1998)

[14] M. M. J. Treacy, T. W. Ebbesen, J. M. Gibson, Nature **381**, 678 (1996)

[15] J. P. Salvetat, J. M. Bonard, N. H. Thomson, A. J. Kulik, L. Forr´o, W. Benoit, L. Zuppiroli, Appl. Phys. A, **69**, 55 (1999)

[16] N. Yao, V. Lordi, J. Appl. Phys. **84**, 1939 (1998)

[17] O.M. Ajayan, O. Stephan, C. Colliex, D. Trauth, Science **265**, 1212 (1994)

[18] P. Poncharal, Z. L. Wang, D. Ugarte, W.A.de Heer, Science **283**, 1513 (1999)

[19] M. R. Falvo, G. J. Clary, R. M. Taylor, V. Chi, et al. Nature **389**, 582 (1997)

[20] E. W. Wong, P. E. Sheehan, C. M. Lieber, Science **277**, 1971 (1997)

[21] J. P. Salvetat, A. J. Kulik, J. M. Bonard, et al. Adv. Mater. **11**, 161 (1999)

[22] F. Ding, Phys. Rev. B **72**, 245409 (2005)

[23] K. M. Liew, C. H. Wong, X. Q. He, M.J.Tan, S. A.Meguid, Phys. Rev. B **69**, 115429 (2004)

[24] V. U. Unnikrishnan, D. Banerjee, J. N. Reddy, Int. J. Therm. Sci. **47**, 1602 (2008).

[25] Y. Zhou, M. A. Baseer, H. Mahfuz, S. Jeelani, Mater. Sci. Eng. A, **420**, 63 (2006)

[26] G. Overney, W. Zhong, D. Tomanek, Z. Phys. D, **27**, 93 (1993)

[27] J. P. Lu, J. Phys. Chem. Solids, **58**, 1649 (1997)

[28] B. I. Yakobson, C. J. Brabec, J. Bernholc, Phys. Rev. Lett. **76**, 2511 (1996)

[29] J. P. Lu, Phys. Rev. Lett. **79**, 1297 (1997)

[30] S. A. Meguid, J.M. Wernik, Z. Q. Cheng, Int. J. Solids Struct. **47**, 1723 (2010)

[31] C. Y. Li, T. W. Chou, Int. J. Solids Struct. **40**, 2487 (2003)

[32] J. L. Tsai, S. H. Tzeng, Y. T. Chiu, Compos. Part B **41**, 106 (2010)

[33] T. Natsuki, K. Tantrakarn, M. Endo, Carbon **42**, 39 (2004)

[34] W. D. Cornell, P. Cieplak, C. I. Bayly, et al. J. Am. Chem. Soc. **117**, 5179 (1995)

CHAPTER THREE

Vibration Characteristics of Double-walled Carbon Nanotubes

3 Vibration characteristics of double-walled carbon nanotubes

Based on the analysis of the mechanical properties of CNTs in chapter two, the vibrational behavior of CNTs can be done on appropriate models in the following chapters. The study of vibrational properties in CNTs is of great current interest [1-3], which can be used to measure the elastic modulus of individual CNTs [4,5]. The CNT dimensions and vibration amplitudes were measured by electron micrographs, and it was assumed that the vibration modes were driven stochastically and chosen of clamped cantilevers [5]. For vibration analysis of one-dimensional beam-like structures, Euler–Bernoulli beam model and Bresse-Timoshenko beam model were usually employed, which assumed that the cross-section of beams remained plane under bending deformation [1,6,7]. In the Euler - Bernoulli beam model, the cross-section of beam was perpendicular to the neutral axis, since the classical Euler–Bernoulli beam model can give a simple and reliable prediction on the mechanical behavior of CNTs under some circumstances, the vibration property of the embedded CNT will be studied by this continuum model.

3.1 Vibration characteristics of double-walled carbon nanotubes embedded in an elastic medium

3.1.1 Introduction

The carbon nanotubes can be substantially applied such as nanoelectromechanical system (NEMS) [8]. The NEMS using CNTs are evolving, with new scientific studies and technical applications. However, these NEMS are extremely small in size and their dynamic properties are commonly associated with super high frequency. To correctly design NEMS, therefore, it becomes necessary to accurately analyze the high frequency vibration characteristics of CNTs. In the this section, the main objective is to propose a theoretical approach to free vibration characteristic analysis of DWCNTs and the DWCNTs embedded in an elastic medium. We build a double-elastic beam model based on the Euler-Bernoulli beam theory, and the surrounding elastic medium is described as the Winkler model characterized by the spring. Since both in-phase and anti-phase modes of DWCNTs are considered, the method provides an accurate analysis of the resonant frequency of DWCNTs. The resonance of DWCNTs with anti-phase mode will be excited at the highly vibration frequency. The noncoaxial vibration of DWCNTs distorts the geometry of DWCNTs and will crucially affect some of their important physical properties, such as electronic [9] and optical [10] ones. The results show that the influence of the phase modes and harmonic numbers of DWCNTs on the vibration frequencies is significant. The resonant frequencies of the DWCNTs with anti-phase mode are larger than those with in-phase mode for the case of the same harmonic number.

3.1.2 Double-Elastic beam model

Based on the Euler-Bernoulli beam model, which assumes that the cross section of a

beam remains plane during flexure and is perpendicular to the neutral axis, the governing equation of motion for the beam is given by

$$\rho A\frac{\partial^2 w}{\partial^2 t}+EI\frac{\partial^4 w}{\partial^4 x}=p(x) \tag{3-1}$$

where x and t are the axial coordinate and time, respectively. $w(x,t)$ is the deflection of the beam. $p(x)$ is the distributed transverse pressure acting on the beam per unit axial length. E is the elastic modulus, and ρ is the mass density. I and A are the moment of inertia and the area of the cross-section, respectively.

It is well known that DWCNTs are distinguished from traditional elastic beams by their hollow two-layer structure. For the DWCNTs, the interaction between the inner and outer nanotubes is considered to be coupled together through the vdW forces. Eq. (3-1) can be used for each layer of the inner and outer nanotubes of DWCNTs. Based on the Euler-Bernoulli beam model, the differential equations governing the motion are described by the following two-coupled equations

$$\rho A_1\frac{\partial^2 w_1}{\partial^2 t}+EI_1\frac{\partial^4 w_1}{\partial^4 x}=p_1 \tag{3-2}$$

$$\rho A_2\frac{\partial^2 w_2}{\partial^2 t}+EI_2\frac{\partial^4 w_2}{\partial^4 x}=p_2 \tag{3-3}$$

where the subscripts 1 and 2 denote the quantities associated with the inner and outer nanotubes of DWCNTs. $p_j(j=1,2)$ are the pressures exerted on the inner and outer nanotubes, respectively.

For small-deflection linear vibration, the interaction pressure at any point between two adjacent nanotubes depends linearly on the difference of their deflections at that point. Thus, the pressure p_1 acting on the inner tube caused by the vdW interaction is given by

$$p_1 = c(w_2 - w_1) \tag{3-4}$$

where c is the vdW interaction coefficient between inner and outer nanotubes.

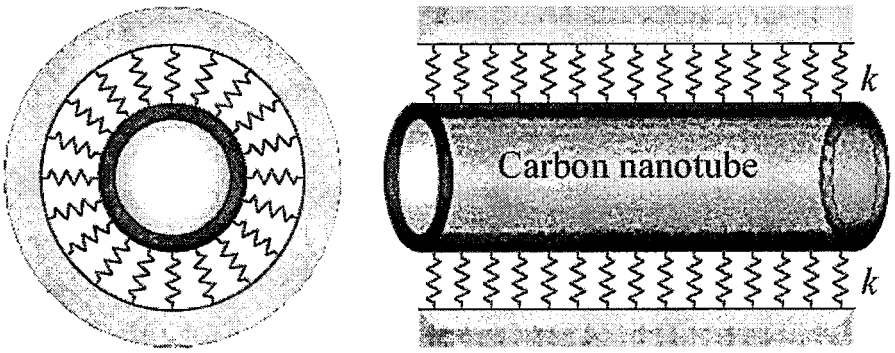

Figure 3.1 Analysis model of CNTs embedded in elastic medium

The Winkler spring model has been widely used to analyze the mechanical properties of embedded CNTs. Figure 3.1 shows the analysis model of CNTs embedded in an elastic medium. The pressure p_w acting on the outermost layer due to the surrounding elastic medium can be given by [11]

$$p_w = -k w_2 \tag{3-5}$$

where the negative sign indicates that the pressure p_w is opposite to the deflection of the nanotubes. k is a spring constant relative to the elastic medium, the diameter of nanotubes, and the wave-length of vibrational modes.

Thus, for the embedded DWCNTs, the pressure of the outermost nanotube contacting with the elastic medium is given by

$$p_2 = p_w - c(w_2 - w_1) \tag{3-6}$$

In this simulation, the vdW interaction coefficient (c) can be obtained from the

interlayer energy potential, given as [12]

$$c = \frac{\pi\varepsilon R_1 R_2 \sigma^6}{a^4}\left[\frac{1001\sigma^6}{3}H^{13} - \frac{1120}{9}H^7\right] \tag{3-7}$$

where

$$H^m = (R_1 + R_2)^{-m}\int_0^{\pi/2}\frac{d\theta}{(1-K\cos^2\theta)^{m/2}}, \qquad (m = 7, 13), \tag{3-8}$$

and

$$K = \frac{4R_1 R_2}{(R_1 + R_2)^2} \tag{3-9}$$

where $a = 0.142\,nm$ is the carbon-carbon bond length, R_1 and R_2 are the inner and outer radiuses of DWCNTs, σ and ε are the vdW radius and the well depth of the Lennard-Jones potential, respectively. The vdW parameters in the Lennard-Jones potential are $\varepsilon = 2.967\,\text{meV}$ and $\sigma = 0.34\,\text{nm}$ taken as reported by Saito et al. [13].

We consider that the deflection of DWCNTs may be different vibration modes $Y_j(x),\ j = 1,2$ for the inner and outer nanotubes. Then, the displacements of the vibrational solution in the DWCNTs can be given by

$$w_j = Y_j(x)e^{i\omega t}, \qquad (j = 1, 2) \tag{3-10}$$

where ω is the vibration frequency of DWCNTs.

Substituting Eq. (3-10) into Eq. (3-2) and (3-3), and using Eqs. (3-4) - (3-6), we obtain the coupled equation of the vibrational properties in DWCNTs

$$\begin{bmatrix} c - \rho A_1\omega^2 + EI_1 D^{(4)} & -c \\ -c & (k+c) - \rho A_2\omega^2 + EI_2 D^{(4)} \end{bmatrix}\begin{Bmatrix} Y_1 \\ Y_2 \end{Bmatrix} = \begin{Bmatrix} 0 \\ 0 \end{Bmatrix} \tag{3-11}$$

where D is the differential operator. Eliminating one of the two variables Y_1 and Y_2 from Eq. (3-11), we yield

$$\left(D^{(8)}+2pD^{(4)}+q\right)W=0 \tag{3-12}$$

where $W=Y_1$ or Y_2, and

$$p=\frac{1}{2}\left(\frac{c-\rho A_1\omega^2}{EI_1}+\frac{c'-\rho A_2\omega^2}{EI_2}\right) \tag{3-13}$$

$$q=\frac{\left(c-\rho A_1\omega^2\right)\left(c'-\rho A_2\omega^2\right)-c^2}{\left(EI_1\right)\left(EI_2\right)}, \qquad c'=c+k. \tag{3-14}$$

The solution of the unknown quantity $W=Y_1,\ Y_2$ in Eq. (3-12) is obtained as follows

(1) If $q<0$, and for any p, the solution of the differential equation (12) can be given in

$$\begin{aligned} Y_1 &= C_1e^{\sqrt[4]{\alpha}x}+C_2e^{-\sqrt[4]{\alpha}x}+C_3\cos\left(\sqrt[4]{\alpha}x\right)+C_4\sin\left(\sqrt[4]{\alpha}x\right) \\ &+e^{\left(\sqrt[4]{\beta}/\sqrt{2}\right)x}\left[C_5\cos\left(\sqrt[4]{\beta}/\sqrt{2}\right)x+C_6\sin\left(\sqrt[4]{\beta}/\sqrt{2}\right)x\right] \\ &+e^{-\left(\sqrt[4]{\beta}/\sqrt{2}\right)x}\left[C_7\cos\left(\sqrt[4]{\beta}/\sqrt{2}\right)x+C_8\sin\left(\sqrt[4]{\beta}/\sqrt{2}\right)x\right] \end{aligned} \tag{3-15}$$

$$\begin{aligned} Y_2 &= \lambda_1C_1e^{\sqrt[4]{\alpha}x}+\lambda_1C_2e^{-\sqrt[4]{\alpha}x}+\lambda_1C_3\cos\left(\sqrt[4]{\alpha}x\right)+\lambda_1C_4\sin\left(\sqrt[4]{\alpha}x\right) \\ &+\lambda_2e^{\left(\sqrt[4]{\beta}/\sqrt{2}\right)x}\left[C_5\cos\left(\sqrt[4]{\beta}/\sqrt{2}\right)x+C_6\sin\left(\sqrt[4]{\beta}/\sqrt{2}\right)x\right] \\ &+\lambda_2e^{-\left(\sqrt[4]{\beta}/\sqrt{2}\right)x}\left[C_7\cos\left(\sqrt[4]{\beta}/\sqrt{2}\right)x+C_8\sin\left(\sqrt[4]{\beta}/\sqrt{2}\right)x\right] \end{aligned} \tag{3-16}$$

where $C_j\ (j=1,2,\cdots,8)$ are unknown integration constants, and

$$\alpha=-p+\sqrt{p^2-q}, \qquad \beta=p+\sqrt{p^2-q}, \tag{3-17}$$

$$p^2-q=\frac{1}{2}\left(\frac{c-\rho A_1\omega^2}{EI_1}-\frac{c'-\rho A_2\omega^2}{EI_2}\right)^2+\frac{c^2}{2\left(EI_1\right)\left(EI_2\right)}\geq 0 \tag{3-18}$$

and λ_1 and λ_2 are associated amplitude ratios of the outer to inner nanotubes, which can be obtained from Eq. (3-11)

$$\lambda_j=1+\frac{EI_1\gamma_j}{c}-\frac{\rho A_1\omega^2}{c}, \quad j=1,2 \tag{3-19}$$

where $\gamma_{1,2} = \mp p + \sqrt{p^2 - q}$.

(2) If $q > 0$, from Eq. (3-14), we have

$$\left(c - \rho A_1 \omega^2\right)\left(c' - \rho A_2 \omega^2\right) > c^2 \tag{3-20}$$

That is

$$\omega^2 > \frac{\left(c' A_1 + c A_2\right) + \sqrt{\Delta}}{2\rho A_1 A_2}, \qquad \Delta = \left(c' A_1 - c A_2\right)^2 + 4c^2 A_1 A_2 \tag{3-21}$$

Furthermore, we obtain form Eq. (3-21)

$$c - \rho A_1 \omega^2 < \frac{\left(c' A_1 - c A_2\right) - \sqrt{\Delta}}{2A_2} < c\sqrt{\frac{A_1}{A_2}} \tag{3-22}$$

$$c' - \rho A_2 \omega^2 < \frac{\left(c' A_1 - c A_2\right) - \sqrt{\Delta}}{2A_1} < c\sqrt{\frac{A_2}{A_1}} \tag{3-23}$$

Substituting Eq. (3-22) and (23) into Eq. (3-13) leads to $p < 0$. Therefore, the solution of differential equation (12) can be given in the following forms

$$\begin{aligned} Y_1 = {} & C_1 e^{\sqrt[4]{\alpha}x} + C_2 e^{-\sqrt[4]{\alpha}x} + C_3 \cos\left(\sqrt[4]{\alpha}x\right) + C_4 \sin\left(\sqrt[4]{\alpha}x\right) \\ & + C_5 e^{\sqrt[4]{\beta}x} + C_6 e^{-\sqrt[4]{\beta}x} + C_7 \cos\left(\sqrt[4]{\beta}x\right) + C_8 \sin\left(\sqrt[4]{\beta}x\right) \end{aligned} \tag{3-24}$$

$$\begin{aligned} Y_2 = {} & \lambda_1 C_1 e^{\sqrt[4]{\alpha}x} + \lambda_1 C_2 e^{-\sqrt[4]{\alpha}x} + \lambda_1 C_3 \cos\left(\sqrt[4]{\alpha}x\right) + \lambda_1 C_4 \sin\left(\sqrt[4]{\alpha}x\right) \\ & + \lambda_2 C_5 e^{\sqrt[4]{\beta}x} + \lambda_2 C_6 e^{-\sqrt[4]{\beta}x} + \lambda_2 C_7 \cos\left(\sqrt[4]{\beta}x\right) + \lambda_2 C_8 \sin\left(\sqrt[4]{\beta}x\right) \end{aligned} \tag{3-25}$$

where

$$\alpha = -p + \sqrt{p^2 - q}, \qquad \beta = -p - \sqrt{p^2 - q}. \tag{3-26}$$

and the amplitude ratio coefficients of the inner to outer nanotubes are

$$\lambda_j = 1 + \frac{EI_1 \gamma_j}{c} - \frac{\rho A_1 \omega^2}{c}, \quad j = 1, 2 \tag{3-27}$$

where $\gamma_{1,2} = -p \pm \sqrt{p^2 - q}$.

For the embedded DWCNTs with a length of L, the boundary conditions for free inner and outer tubes can be written as

$$Y_1''(0) = Y_1''(L) = Y_1'''(0) = Y_1'''(L) = 0 \tag{3-28}$$

$$Y_2''(0) = Y_2''(L) = Y_2'''(0) = Y_2'''(L) = 0 \tag{3-29}$$

Substituting Eqs. (3-15), (3-16) and Eqs. (3-24), (3-25) into the above boundary conditions, we yield the simultaneous equation

$$M[\omega, L]_{8\times 8}\begin{bmatrix} C_1 \\ C_2 \\ \vdots \\ C_8 \end{bmatrix} = 0, \tag{3-30}$$

where $M[\omega, L]_{8\times 8}$ is a 8×8 matrix with parameters, of the vibration frequency ω and the nanotube length. The vibration frequencies and the associated vibration modes of DWCNTs can be obtained from $|M|_{8\times 8} = 0$, which is the condition of nontrivial solution of C_j $(j = 1, 2, \cdots, 8)$ in Eq. (3-30).

3.1.3 Numerical results and discussion

In this section, vibration characteristic analysis was carried out for SWCNTs, DWCNTs and the DWCNTs embedded in an elastic modulus. We consider a DWCNT having the inner and outer diameters of 2.2 and 3.0 nm, respectively. The effective thickness of each DWCNTs was taken to be that of a graphite sheet with 0.34 nm, and the one of SWCNTs is 0.1 nm. The CNTs had an elastic modulus of 3.3 TPa, and the density of 2.3 g/cm^3 [14,15].

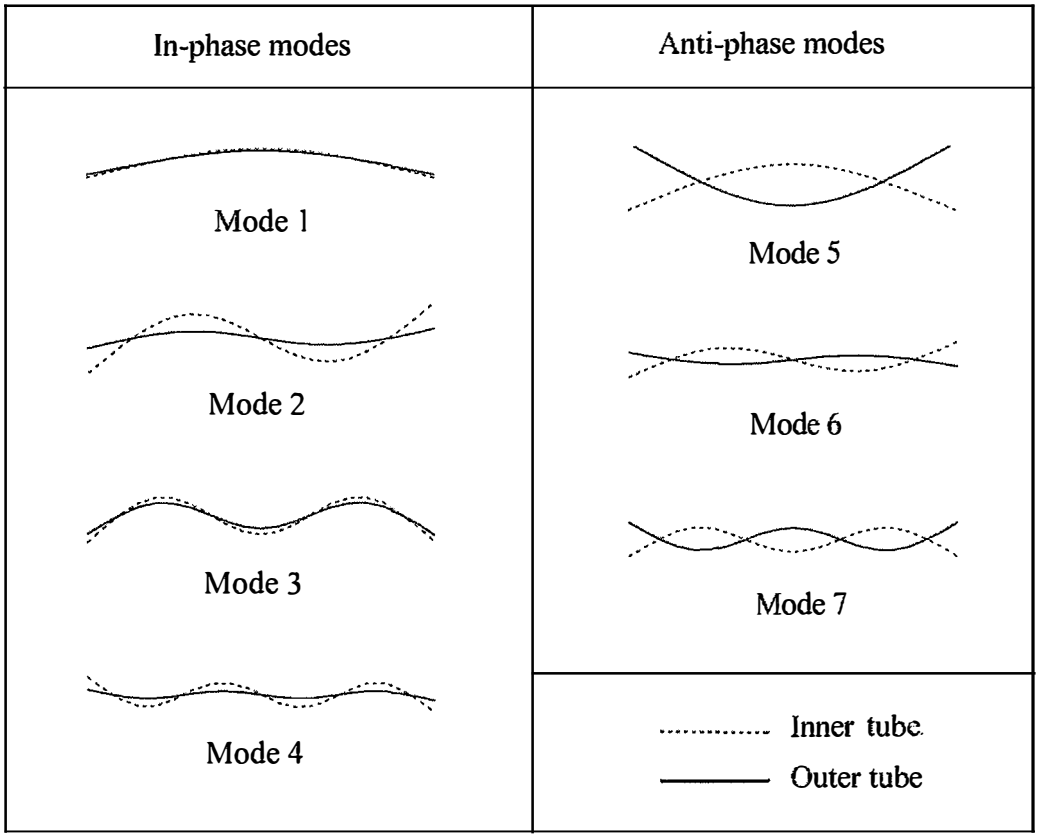

Figure 3.2 Seven vibration modes of DWCNTs with free supported boundary condition

Based on the present theoretical approach, the first seven vibration modes of DWCNTs with free boundary conditions are shown in Figure 3.2. Modes 1-4 indicate the first four vibration modes of DWCNTs. These are in-phase modes, which mean that the inner and outer nanotubes have the same direction of deflection. Modes 5-7 are the first three vibrations of anti-phase mode, in which the deflections of the inner and outer nanotubes can occur in the opposite direction. It is seen from Figure 3.2 that the vibration amplitudes (modes 1-4) of the inner nanotube are larger than those of the outer nanotube. Figure 3.3 shows the resonant frequencies of the DWCNTs with seven vibration modes (see Figure 3.2). It is found that the DWCNTs exhibit very high frequency over terahertz. In order to compare with SWCNTs, we also plot the vibration frequencies of the SWCNTs, having the same diameter as DWCNTs. In the case of SWCNTs, the resonant frequencies with different modes can be given by

$$\omega_i = \frac{\beta_i^2}{L^2}\sqrt{\frac{EI}{\rho A}} \tag{3-31}$$

where $\beta_1 = 4.73$, $\beta_2 = 7.85$, $\beta_3 = 11.0$ and $\beta_4 = 14.14$ mode values corresponding to the one, two, three and four half-waves (harmonic numbers), respectively. A is the cross-sectional area of SWCNTs, and L is the length.

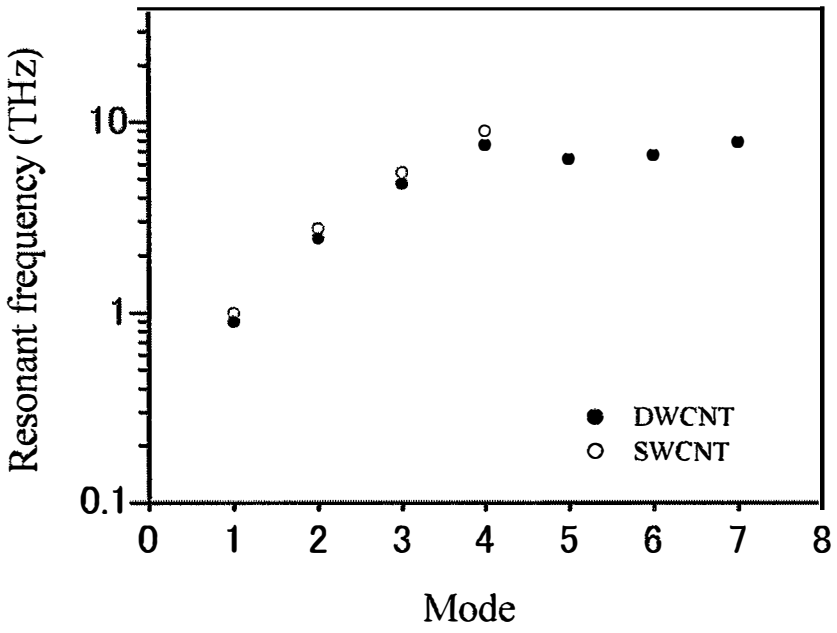

Figure 3.3 Resonant frequencies for seven vibration modes in SWCNTs and DWCNTs with aspect ratio 10

For the SWCNTs with only one layer, there are not the anti-phase modes 5-7 shown in Figure 3.2. Compared to modes 1-4 between DWCNTs and SWCNTs, it is seen from Figure 3.3 that the resonant frequencies of SWCNTs are about 15 percent larger than those of the DWCNTs. The values of both SWCNTs and DWCNTs increase with increasing harmonic numbers for the in-phase modes. In the case of DWCNTs, however, the characteristic frequencies are enormously affected by the vibrational direction of the inner and outer nanotubes. As vibration having the same harmonic number, the resonant frequencies of the anti-phase mode can be larger than those of the

in-phase mode. It is more worthy of notice that the resonant frequencies (anti-phase mode) of DWCNTs with a low harmonic number can be higher than those of in-phase mode with high harmonic number, because it is well known that the resonant frequency commonly increases with increasing harmonic number. For high vibration frequency of DWCNTs with anti-phase mode, the vibrational frequencies are very close because the vdW interaction between the inner and outer nanotubes is considered to be the dominating factor. It suggests that the DWCNTs with anti-phase mode are insensitive to the variation of axial wave number.

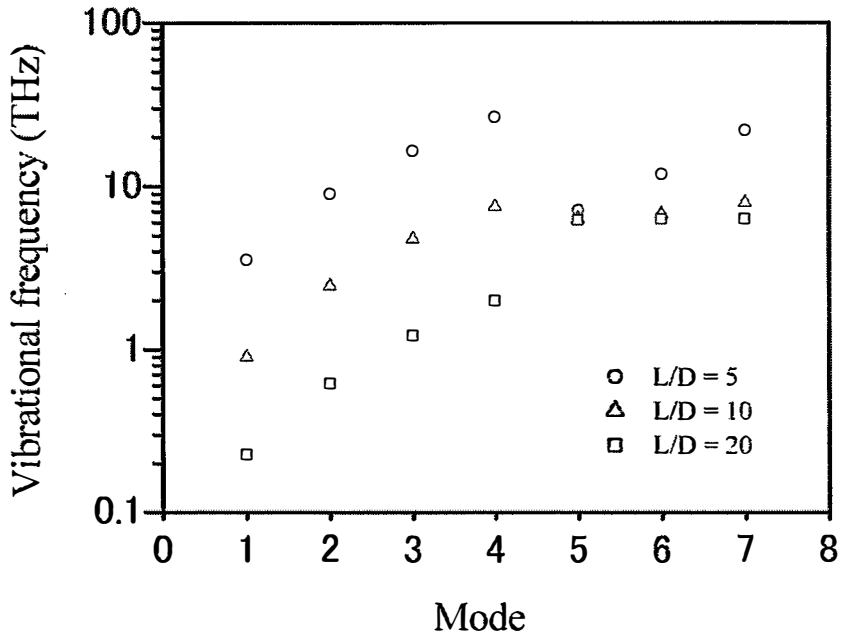

Figure 3.4 Relationship between resonant frequencies and vibration modes for DWCNTs with different aspect ratios

The resonant frequencies of DWCNTs with different aspect ratios are shown in Figure 3.4 as a function of the vibration modes. The resonant frequencies of DWCNTs decrease with increasing aspect ratio of nanotubes. For larger aspect ratio, the resonant frequencies of DWCNTs with the anti-phase modes are insensitive to the harmonic numbers. The aspect ratio dependence of the frequency is insignificant for the first

harmonic number with anti-phase mode (Mode 5).

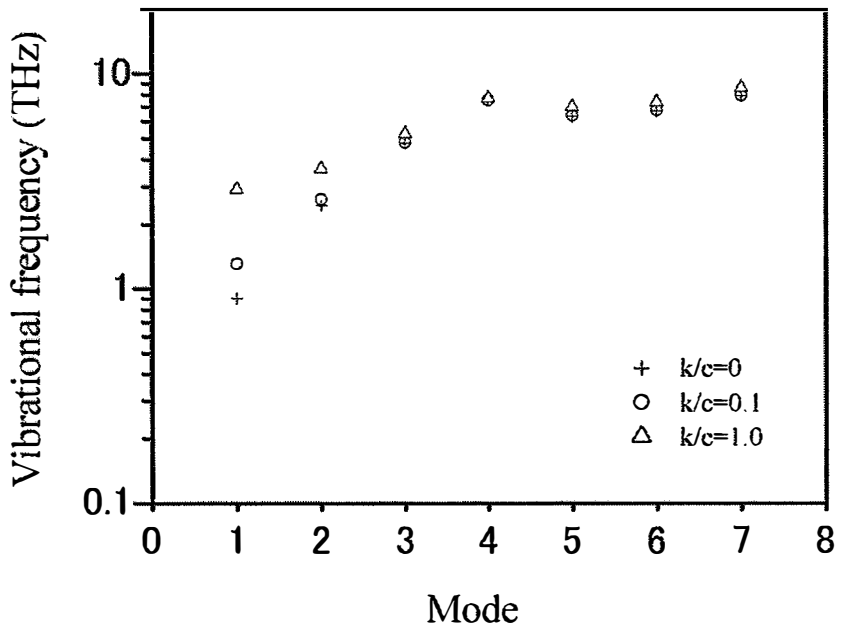

Figure 3.5 Influence of the surrounding elastic medium on the resonant frequencies of DWCNTs with aspect ratio 10

Figure 3.5 shows the resonant frequencies of embedded DWCNTs for different surrounding media. The influences of the surrounding medium on the resonant frequency are investigated based on the Winkler spring model. We take the ratio of the spring constant to the interaction coefficient (k/c) as a parameter considering the variation with the stiffness of the surrounding medium. It can be found that the resonant frequencies of the embedded DWCNTs are larger than those of the nested DWCNTs. Especially, the influences of the surrounding medium on the resonant frequency are significant for the first in-phase mode. On the other hand, the stiffness of the surrounding medium impacts little on the resonant frequencies of the anti-phase modes.

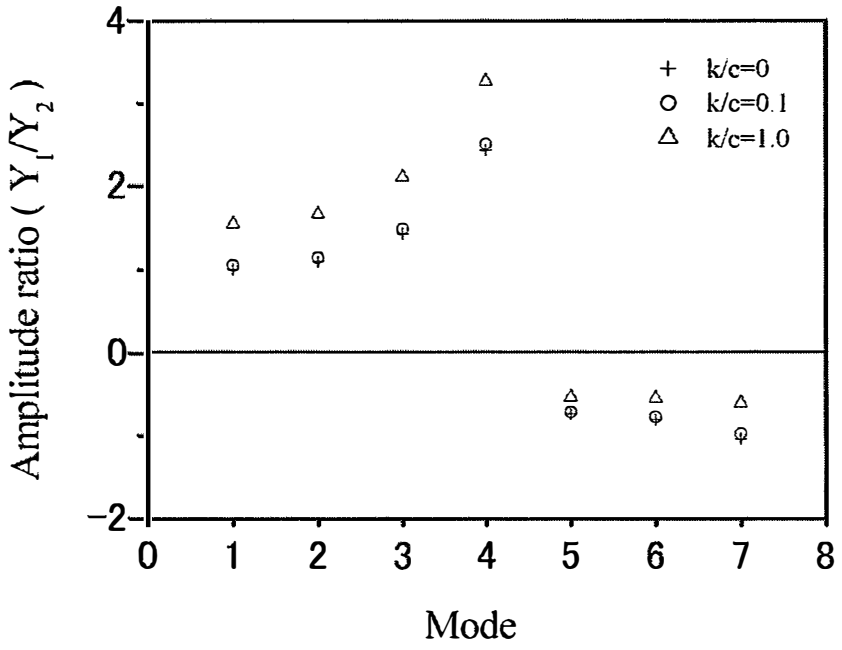

Figure 3.6 Vibration amplitude ratio of the inner to outer nanotubes in different vibration modes with aspect ratio 10

Figure 3.6 shows the vibrational amplitude ratios of the inner to outer nanotubes for different vibration modes and surrounding media. The negative amplitude ratio indicates that the deflection direction of the inner nanotube is opposite to that of the outer nanotube, which means the anti-phase mode. For the in-phase modes (modes 1-4) of DWCNTs, the vibration deflections of the inner nanotubes are larger than those of the outer nanotubes because the aspect ratios of the inner to outer nanotubes are larger than 1. It is found that the vibration amplitude ratio increases with a raise of the surrounding medium modulus. The vibration amplitude ratio of the nested DWCNTs with the first in-phase mode is almost near to 1. For the anti-phase modes (modes 5-7), however, the vibration amplitude ratios of the inner to outer nanotubes are less than -1. This indicates that the vibration deflections of two nanotubes are the opposite direction, and the deflections of the inner nanotubes are less than those of the outer nanotubes. The vibration amplitude ratio of the inner to outer nanotubes decreases with increasing modulus of the surrounding medium. However, the dependence of the anti-phase mode

on the vibration amplitude ratio is found to be less for the DWCNTs embedded in higher surrounding elastic medium.

3.1.4 Conclusions

This paper studies the free vibration of DWCNTs embedded in an elastic medium. Based on a multiple-elastic-beam model, a theoretical approach is proposed to investigate free vibration of the DWCNTs with free supported boundary condition. The present method can provide accurate analysis of the resonant frequencies of DWCNTs and the DWCNTs embedded in an elastic medium because both in-phase and anti-phase modes are considered. Using the present theoretical approach, the free resonant frequencies of DWCNTs with different vibration modes are investigated. The results indicate that the phase modes have a strong influence on the vibrational frequencies of DWCNTs. For the same harmonic number, the resonant frequencies of DWCNTs with the anti-phase mode are larger than those of the in-phase mode. The stiffness of the surrounding medium affects the resonant frequencies of DWCNTs, especially for the first in-phase mode. The investigation presented may be helpful in the application of CNTs such as high frequency oscillators, dynamic mechanical analysis and mechanical sensors.

3.2 Vibrational analysis of double-walled carbon nanotubes with inner and outer nanotubes of different lengths

3.2.1 Introduction

DWCNTs with different wall lengths have some specific practical applications where DWCNTs with walls of the same length cannot be used. CNTs with fastigiated structures can be used to effectively deliver DNA and small dye molecules into intact

plant cells by gradually changing the wall lengths of CNTs with different diameters. The structure of DWCNTs with different wall lengths is more stable than those with walls of equal length, and they can be used as atomic force microscopy tips. In the future, controlling the shape of CNTs with different wall lengths could allow their use as nanomotors and nanomachines. The preparation of DWCNTs with different lengths inner and outer tubes has been achieved [16-20]. This makes the vibrational analysis of DWCNTs with different wall lengths significant from both theoretical and practical perspectives.

Yoon *et al.* [21] and Zhang *et al.* [22] reported vibration behavior of CNTs using double-elastic beam model embedded in an elastic medium and under compressive axial load. An accurate analysis of the resonant frequency of DWCNTs with free-fixed end conditions was proposed by Natsuki *et al.* [23] considering both in-phase and anti-phase modes of DWCNTs. Murmu *et al.* [24] proposed a thermal vibration model to analyze the natural frequency of single-walled carbon nanotubes (SWCNTs) with simply supported ends using the nonlocal elasticity and Euler-Bernoulli theories. Malola *et al.* [25] discussed the effect of bending on the Raman-active vibrational modes of CNTs. However, few examples have been concerned with the vibration analysis of DWCNTs with inner and outer walls of different lengths.

In the above, the vibration characteristics of DWCNTs with the same length walls were determined based on Euler–Bernoulli beam theory. In this section, DWCNT models with different tube lengths are constructed based on our previous work. Because both in-phase and anti-phase modes of DWCNTs are considered, the method provides an accurate analysis of the resonant frequency of these DWCNTs. The resonance of DWCNTs in an anti-phase mode is excited at a high vibration frequency. The results show that the influences of the length mismatch and the vibrational modes on the resonant frequencies are significant, especially for shorter DWCNTs of unequal

inner/outer lengths.

3.2.2 Theoretical approach

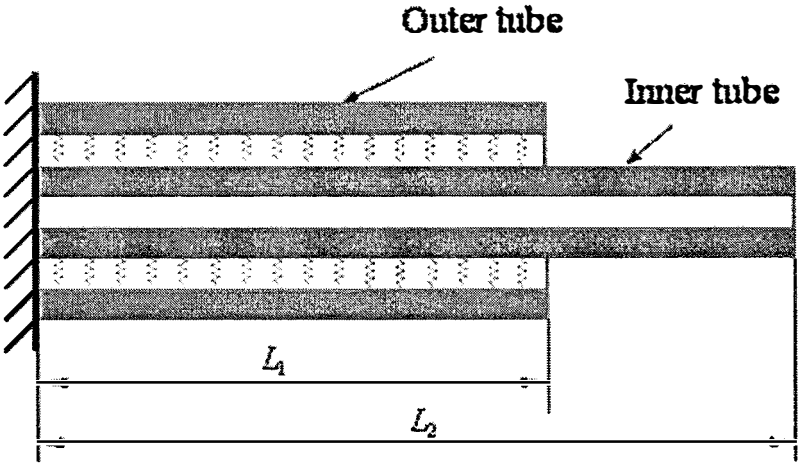

Figure 3.7 Analytical model of cantilevered DWCNTs with different inner and outer nanotube lengths in longitudinal section

Based on the Euler-Bernoulli beam model, which assumes that the cross-section of a beam remains planar during flexion and is perpendicular to the neutral axis, the governing equation of motion for a SWCNT is given by

$$\rho A \frac{\partial^2 w}{\partial t^2} + EI \frac{\partial^4 w}{\partial x^4} = p(x) \tag{3-32}$$

where x and t are the longitudinal coordinate and time, respectively. $w(x,t)$ is the deflection of the nanotube, $p(x)$ is the distributed transverse pressure acting on the nanotube per unit axial length, E is the elastic modulus, and ρ is the mass density. I and A are the moment of inertia and the area of the cross-section, respectively.

Figure 3.7 shows the analytical model of a cantilevered DWCNT with different nanotube lengths. For DWCNTs with the inner tube length L_2 and outer tube length L_1, the interaction between the inner and outer nanotubes is considered to be coupled together through the van der Waals (vdW) forces. Using the Euler-Bernoulli beam

equation in Eq. (3-32), the differential equation governing the motion of the inner and outer nanotubes $(x \le L_2)$ can be described by the following two-coupled equations:

$$\rho A_1 \frac{\partial^2 w_1}{\partial t^2} + EI_1 \frac{\partial^4 w_1}{\partial x^4} = c(w_2 - w_1) \tag{3-33}$$

$$\rho A_2 \frac{\partial^2 w_2}{\partial t^2} + EI_2 \frac{\partial^4 w_2}{\partial x^4} = c(w_1 - w_2) \tag{3-34}$$

where the subscripts 1 and 2 denote the quantities associated with the inner and outer nanotubes, respectively. $w_j (j = 1, 2)$ are the deflections of the inner and outer nanotubes, respectively. c is the vdW interaction coefficient between the inner and outer nanotubes, which can be obtained from the interlayer energy potential and is given as [12]

$$c = \frac{\pi \varepsilon R_1 R_2 \sigma^6}{a^4} \left[\frac{1001\sigma^6}{3} H^{13} - \frac{1120}{9} H^7 \right] \tag{3-35}$$

where

$$H^m = (R_1 + R_2)^{-m} \int_0^{\pi/2} \frac{d\theta}{(1 - K\cos^2\theta)^{m/2}}, \qquad (m = 7, 13), \tag{3-36}$$

and

$$K = \frac{4R_1 R_2}{(R_1 + R_2)^2} \tag{3-37}$$

where a=0.142 nm is the carbon-carbon bond length, R_1 and R_2 are the inner and outer radii of the DWCNTs, and σ and ε are the vdW radius and the well depth of the Lennard-Jones potential, respectively. The vdW parameters in the Lennard-Jones potential are ε= 2.967 meV and σ=0.34 nm as reported by Saito *et al.* [13].

For the inner nanotube with L_2 larger than L_1 as shown in Figure 3.7, the differential equation governing the motion of SWCNTs is given by

$$\rho A_1 \frac{\partial^2 w_3}{\partial t^2} + EI_1 \frac{\partial^4 w_3}{\partial x^4} = 0. \qquad (L_1 \le x \le L_2) \tag{3-38}$$

where w_3 is the deflection of the inner nanotube where L_2 is larger than L_1.

The harmonic solutions of Eqs. (3-33), (3-34) and (3-38) can be expressed as

$$w_j = Y_j(x)e^{i\omega t}, \qquad (j = 1, 2, 3) \tag{3-39}$$

where $Y_j \ (j = 1, 2, 3)$ are the vibrational amplitudes, and ω is the vibrational frequency.

Substituting Eq. (3-39) into Eqs. (3-33) and (3-34) yields the coupled equation of the vibrational properties in the inner and outer nanotubes $(x \le L_1)$:

$$\begin{bmatrix} c - \rho A_1 \omega^2 + EI_1 D^{(4)} & -c \\ -c & (k+c) - \rho A_2 \omega^2 + EI_2 D^{(4)} \end{bmatrix} \begin{Bmatrix} Y_1 \\ Y_2 \end{Bmatrix} = \begin{Bmatrix} 0 \\ 0 \end{Bmatrix} \tag{3-40}$$

where D is the differential operator. Eliminating one of the two variables Y_1 and Y_2 from Eq. (3-40), the governing equation becomes

$$\left(D^{(8)} + 2pD^{(4)} + q\right)W = 0 \tag{3-41}$$

where $W = Y_1$ or Y_2, and

$$p = \frac{1}{2}\left(\frac{c - \rho A_1 \omega^2}{EI_1} + \frac{c' - \rho A_2 \omega^2}{EI_2} \right) \tag{3-42}$$

$$q = \frac{\left(c - \rho A_1 \omega^2\right)\left(c' - \rho A_2 \omega^2\right) - c^2}{\left(EI_1\right)\left(EI_2\right)}, \qquad c' = c + k. \tag{3-43}$$

The solution of the vibrational amplitudes $W = Y_1, Y_2$ in Eq. (3-41) is obtained as follows:

(1) If $q < 0$ and for any p, then $p^2 - q \ge 0$. Therefore, the solutions are

$$
\begin{aligned}
Y_1 &= C_1 e^{\sqrt[4]{\alpha}x} + C_2 e^{-\sqrt[4]{\alpha}x} + C_3 \cos\left(\sqrt[4]{\alpha}x\right) + C_4 \sin\left(\sqrt[4]{\alpha}x\right) \\
&+ e^{\left(\sqrt[4]{\beta}/\sqrt{2}\right)x}\left[C_5 \cos\left(\sqrt[4]{\beta}/\sqrt{2}\right)x + C_6 \sin\left(\sqrt[4]{\beta}/\sqrt{2}\right)x\right] \\
&+ e^{-\left(\sqrt[4]{\beta}/\sqrt{2}\right)x}\left[C_7 \cos\left(\sqrt[4]{\beta}/\sqrt{2}\right)x + C_8 \sin\left(\sqrt[4]{\beta}/\sqrt{2}\right)x\right]
\end{aligned} \tag{3-44}
$$

$$
\begin{aligned}
Y_2 &= \lambda_1 C_1 e^{\sqrt[4]{\alpha}x} + \lambda_1 C_2 e^{-\sqrt[4]{\alpha}x} + \lambda_1 C_3 \cos\left(\sqrt[4]{\alpha}x\right) + \lambda_1 C_4 \sin\left(\sqrt[4]{\alpha}x\right) \\
&+ \lambda_2 e^{\left(\sqrt[4]{\beta}/\sqrt{2}\right)x}\left[C_5 \cos\left(\sqrt[4]{\beta}/\sqrt{2}\right)x + C_6 \sin\left(\sqrt[4]{\beta}/\sqrt{2}\right)x\right] \\
&+ \lambda_2 e^{-\left(\sqrt[4]{\beta}/\sqrt{2}\right)x}\left[C_7 \cos\left(\sqrt[4]{\beta}/\sqrt{2}\right)x + C_8 \sin\left(\sqrt[4]{\beta}/\sqrt{2}\right)x\right]
\end{aligned} \tag{3-45}
$$

where C_j $(j = 1, 2, \cdots, 8)$ are unknown integration constants, and

$$
\alpha = -p + \sqrt{p^2 - q} \geq 0, \quad \beta = p + \sqrt{p^2 - q} \geq 0, \tag{3-46}
$$

where λ_1 and λ_2 are associated amplitude ratios of the outer to inner nanotubes, which can be obtained from Eq. (3-40)

$$
\lambda_j = 1 + \frac{EI_1\gamma_j}{c} - \frac{\rho A_1 \omega^2}{c}, \quad j = 1, 2 \tag{3-47}
$$

where $\gamma_{1,2} = \mp p + \sqrt{p^2 - q}$.

(2) If $q > 0$, from Eq. (3-43), we have

$$
\left(c - \rho A_1 \omega^2\right)\left(c' - \rho A_2 \omega^2\right) > c^2 \tag{3-48}
$$

namely,

$$
\omega^2 > \frac{\left(c' A_1 + c A_2\right) + \sqrt{\Delta}}{2\rho A_1 A_2}, \qquad \Delta = \left(c' A_1 - c A_2\right)^2 + 4c^2 A_1 A_2 \tag{3-49}
$$

Furthermore, from above equations

$$
c - \rho A_1 \omega^2 < \frac{\left(c' A_1 - c A_2\right) - \sqrt{\Delta}}{2A_2} < c\sqrt{\frac{A_1}{A_2}} \tag{3-50}
$$

$$
c' - \rho A_2 \omega^2 < \frac{\left(c' A_1 - c A_2\right) - \sqrt{\Delta}}{2A_1} < c\sqrt{\frac{A_2}{A_1}} \tag{3-51}
$$

Substituting Eqs. (3-50) and (3-51) into Eqs. (3-52) and (3-53) leads to $p < 0$, and

$$p^2 - q = \frac{1}{2}\left(\frac{c - \rho A_1 \omega^2}{EI_1} - \frac{c' - \rho A_2 \omega^2}{EI_2} \right)^2 + \frac{c^2}{2(EI_1)(EI_2)} \geq 0 \tag{3-52}$$

Therefore, the solution of differential equation (10) can be given in the following forms

$$\begin{aligned} Y_1 = {} & C_1 e^{\sqrt[4]{\alpha}x} + C_2 e^{-\sqrt[4]{\alpha}x} + C_3 \cos\left(\sqrt[4]{\alpha}x\right) + C_4 \sin\left(\sqrt[4]{\alpha}x\right) \\ & + C_5 e^{\sqrt[4]{\beta}x} + C_6 e^{-\sqrt[4]{\beta}x} + C_7 \cos\left(\sqrt[4]{\beta}x\right) + C_8 \sin\left(\sqrt[4]{\beta}x\right) \end{aligned} \tag{3-53}$$

$$\begin{aligned} Y_2 = {} & \lambda_1 C_1 e^{\sqrt[4]{\alpha}x} + \lambda_1 C_2 e^{-\sqrt[4]{\alpha}x} + \lambda_1 C_3 \cos\left(\sqrt[4]{\alpha}x\right) + \lambda_1 C_4 \sin\left(\sqrt[4]{\alpha}x\right) \\ & + \lambda_2 C_5 e^{\sqrt[4]{\beta}x} + \lambda_2 C_6 e^{-\sqrt[4]{\beta}x} + \lambda_2 C_7 \cos\left(\sqrt[4]{\beta}x\right) + \lambda_2 C_8 \sin\left(\sqrt[4]{\beta}x\right) \end{aligned} \tag{3-54}$$

where

$$\alpha = -p + \sqrt{p^2 - q} \geq 0, \qquad \beta = -p - \sqrt{p^2 - q} \geq 0 \tag{3-55}$$

and the amplitude ratio coefficients of the inner to outer nanotubes are

$$\lambda_j = 1 + \frac{EI_1 \gamma_j}{c} - \frac{\rho A_1 \omega^2}{c}, \quad j = 1, 2 \tag{3-56}$$

where $\gamma_{1,2} = -p \pm \sqrt{p^2 - q}$.

For the inner nanotube shown in Figure 3.7 with L_2 larger than L_1, the vibrational function is given by

$$Y_3 = C_9 e^{\phi x} + C_{10} e^{-\phi x} + C_{11} \cos(\phi x) + C_{12} \sin(\phi x) \tag{3-57}$$

where

$$\phi = \sqrt[4]{\frac{\rho A_1 \omega^2}{EI_1}} \tag{3-58}$$

Consider that a cantilevered DWCNT as shown in Figure 3.7 has an outer tube length of L_1 and an inner tube length of L_2, the boundary conditions are obeyed as

follows:

(1) for inner and outer tubes with fixed ends

$$Y_1(0) = Y_1'(0) = Y_2(0) = Y_2'(0) = 0 \tag{3-59}$$

(2) for inner and outer tubes with free ends

$$Y_2''(L_1) = Y_2'''(L_1) = Y_3''(L_2) = Y_3'''(L_2) = 0 \tag{3-60}$$

(3) the continuous conditions (at position L_1) for the vibrational functions of the inner tube, expressed by Y_1 and Y_3 are

$$Y_1(L_1) = Y_3(L_1);\ \ Y_1'(L_1) = Y_3'(L_1);\ \ Y_1''(L_1) = Y_3''(L_1);\ \ Y_1'''(L_1) = Y_3'''(L_1) \tag{3-61}$$

Substituting the vibrational functions of the inner and outer nanotubes (Y_1, Y_2 and Y_3) into the above boundary conditions, the simultaneous equation

$$M[\omega, L_1, L_2]_{12\times 12}\begin{bmatrix} C_1 \\ C_2 \\ \vdots \\ C_{12} \end{bmatrix} = 0, \tag{3-62}$$

where $M[\omega, L_1, L_2]_{12\times 12}$ is a 12×12 matrix with parameters of vibration frequency ω, and nanotube lengths L_1 and L_2. The vibration frequencies and the associated vibrational modes of DWCNTs with nanotubes of different lengths can be obtained from $|M|_{12\times 12} = 0$, which is the condition of nontrivial solution of C_j $(j = 1, 2, \cdots, 12)$ in Eq. (3-62).

3.2.3 Numerical results and discussion

In this study, the resonant frequency of cantilevered DWCNTs was determined

using the method described in Section 2. DWCNTs with different length inner and outer nanotubes were considered, where the lengths of the outer and inner nanotubes were fixed (L_1 =constant and L_2=constant) as shown in Figure 3.8. Because the Euler -Bernoulli beam theory leads to some errors for shorter beam structures, we consider that the length-to-diameter aspect ratios of CNTs are larger than 10 [26]. In this simulation, the DWCNTs were taken as (28,0)@(37,0), that is, the inner and outer diameters were 2.19 nm and 2.90 nm, respectively. The effective thickness of each nanotube in the DWCNT (i.e., the inner and outer nanotubes) was taken to be 0.1 nm. The DWCNTs were assumed to have an elastic modulus of 3.3 TPa, and a density of 2.3 g/cm^3 [27, 28].

The resonant vibration of DWCNTs can occur in different mode shapes with lower or higher frequencies. Based on the present theoretical approach, Figure 3.9 plots the corresponding mode shapes of vibration for cantilevered DWCNTs with different wall lengths. Modes 1-7 indicate the first seven vibrational modes, which are shown in order from lower to higher frequency. The vibrational modes are essentially dominated by the vdW coupling between the inner and outer nanotubes. The lower modes (modes 1-4) are vibrations with small axial wavenumbers and are in-phase, which means that the inner and outer nanotubes have the same deflection. In contrast, the vibrational frequencies of the higher modes (modes 5-7) are anti-phase with opposite vibration direction for the inner and outer nanotubes. For inner and outer tubes of different lengths (L_{outer}/L_{inner} =1.4) as shown in Figure 3.9, it can be observed the modes 1-4 are the in-phase ones and the modes 5-7 are anti-phase ones. Moreover, the inner and outer nanotubes are of different axial wavenumber because of their mismatch in length and stiffness. This results in that show the demanded frequency of DWCNTs is easily controlled and obtained by inner and outer tubes of different lengths.

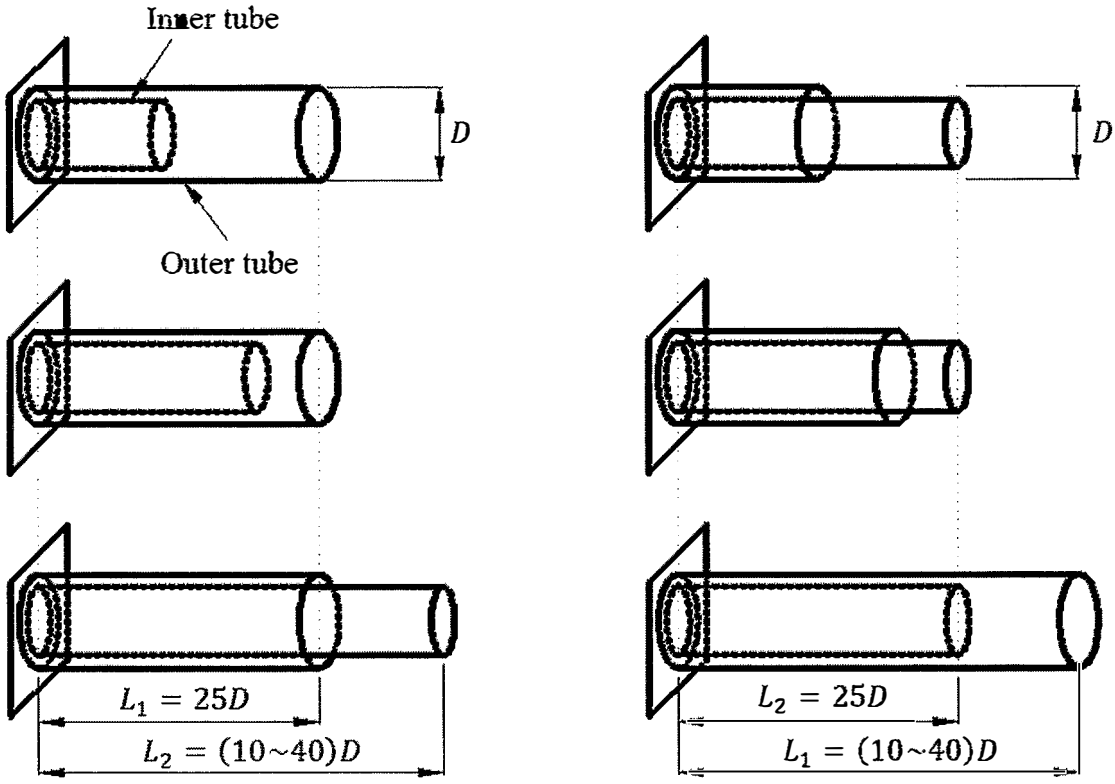

Figure 3.8 Schematic diagram describing cantilevered DWCNTs: (A) fixed outer nanotube length and varying inner nanotube length; (B) fixed inner nanotube length and varying outer nanotube length

The resonant frequencies of cantilevered DWCNTs with a fixed outer wall length (aspect ratio of $L_1/D=15$) and various inner wall lengths (L_2/D=0, 10 and 15) are shown in Figure 3.10 as a function of vibrational modes. The resonant vibration of these CNTs exhibits a very high frequency of greater than terahertz. For the SWCNT with $L_2/D=0$ shown in Figure 3.10, the resonant frequency agrees closely with the result from the well known vibration equation:

$$\omega_n = \frac{\beta_n^2}{L^2}\sqrt{\frac{EI}{\rho A}} \tag{3-63}$$

where the values $\beta_n\ (n=1,2,\cdots)$ of the cantilevered beam can be found by solving the equation $\cos\beta\cosh\beta+1=0$. $\beta_1=1.875$, $\beta_2=4.694$ and $\beta_3=7.854$ for the first,

second and third modes, respectively. $\beta_n = (n+0.5)\pi$ for the larger mode n.

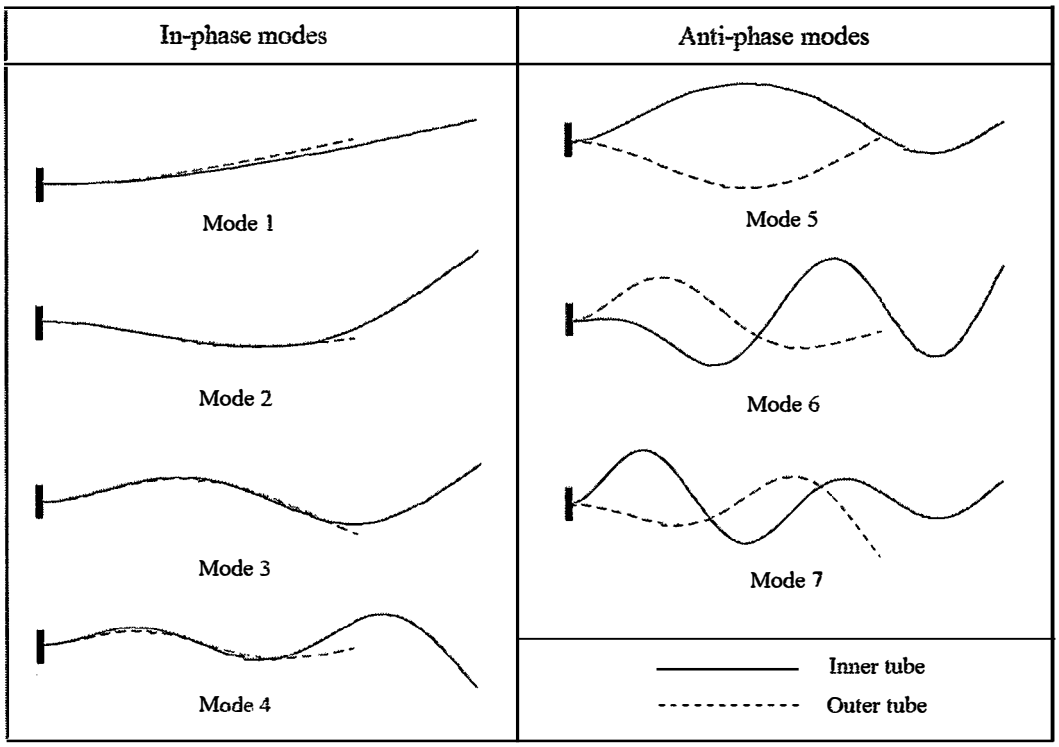

Figure 3.9 First seven mode shapes of vibration for cantilevered DWCNTs with shorter outer and longer inner nanotubes.

Figure 3.10 shows that the resonant frequencies of SWCNTs with $L_1/D=15$ increase with increasing harmonic number. However, for the DWCNTs with different inner tube lengths (L_2/D = 10 and 15), the characteristic vibrational frequencies are insensitive to the anti-phase modes (modes 6-8). Unlike the in-phase modes, the vibrational frequencies of the anti-phase modes of the DWCNTs are much lower than those of SWCNTs. This suggests that the vibrational frequencies in the anti-phase modes are essentially dominated by the vdW coupling between the inner and outer nanotubes in DWCNTs.

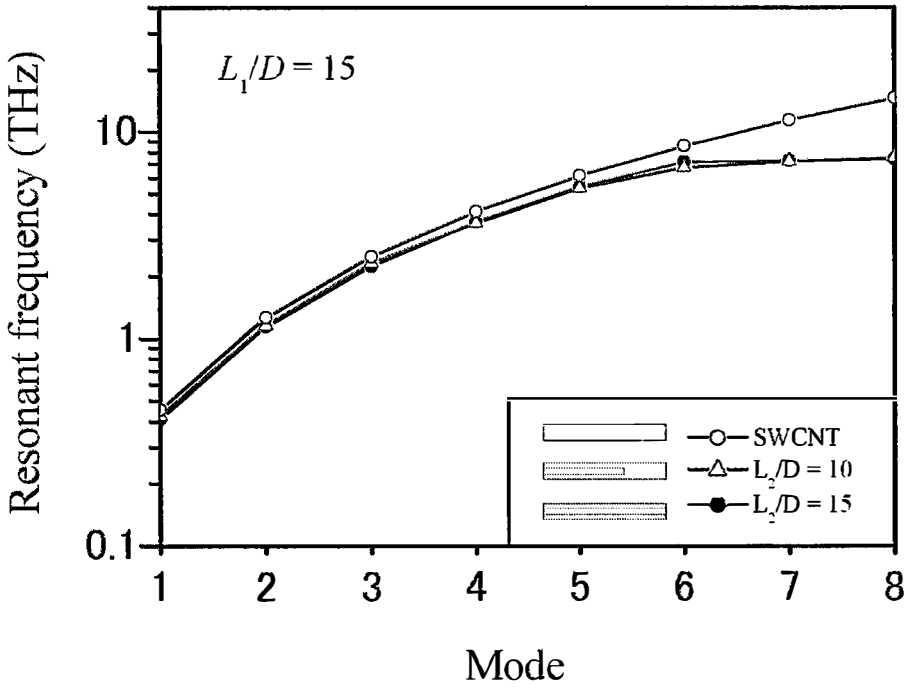

Figure 3.10 Resonant frequencies of cantilevered DWCNTs with fixed outer nanotube length (aspect ratio of L_1/D=15) and various inner nanotube lengths (L_2/D= 0, 10 and 15)

Figures 3.11~3.13 show the resonant frequencies of the DWCNTs with different tube lengths indicated in Figure 3.8, which have either (A) a fixed outer wall length $(L_1/D=25)$ and varying inner tube lengths $(L_2/D=10\sim40)$, and (B) *vice versa*. The changes in the resonant frequencies with varying tube length for modes 1-3 are shown in Figures. 3.11~3.13, respectively. For fundamental vibration frequency (mode 1) as shown in Figure 3.11, the frequency changes of DWCNTs are larger for a constant inner tube length (B) than for the outer one (A) when the difference between the inner and outer tube lengths is larger. The resonant frequency of DWCNTs with fixed inner tube length (B) increases initially with increasing outer tube length, and then decreases. The resonant frequency of condition (A) increases up to the maximum at an aspect ratio of 15, and is about 1.1 times than that of condition (B). For DWCNTs satisfying conditions (A) with constant outer tube length, the fundamental frequency

decreases slightly with increasing inner tube length. An aspect ratio of 25 corresponds to DWCNTs with inner and outer tubes of the same length. Compared with longer DWCNTs (aspect ratio greater than 25), the influence of varying tube length on the resonant frequency is more significant for shorter DWCNTs.

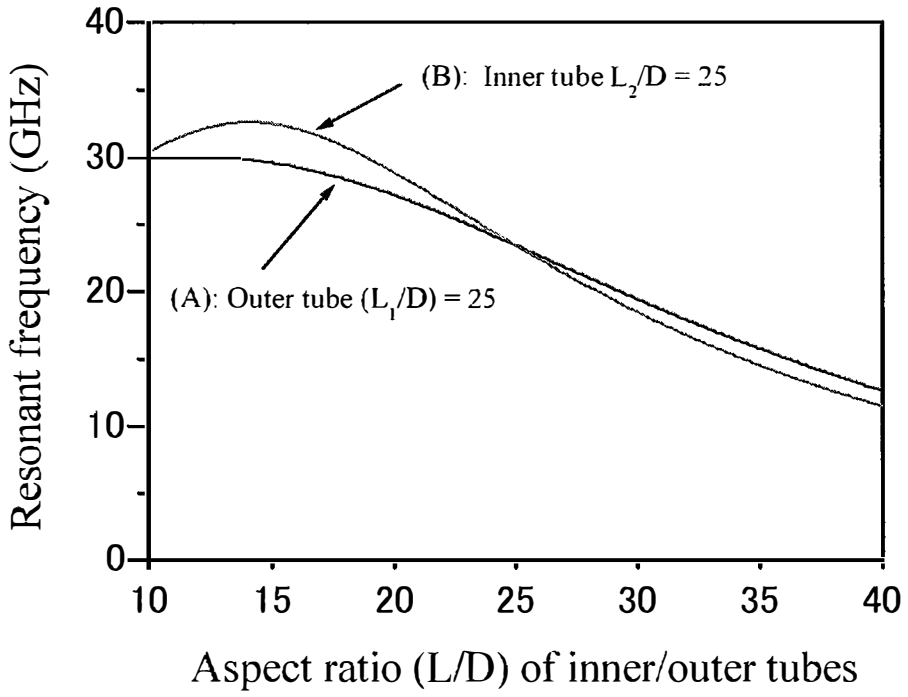

Figure 3.11 Resonant frequencies of cantilevered DWCNTs for vibration mode 1

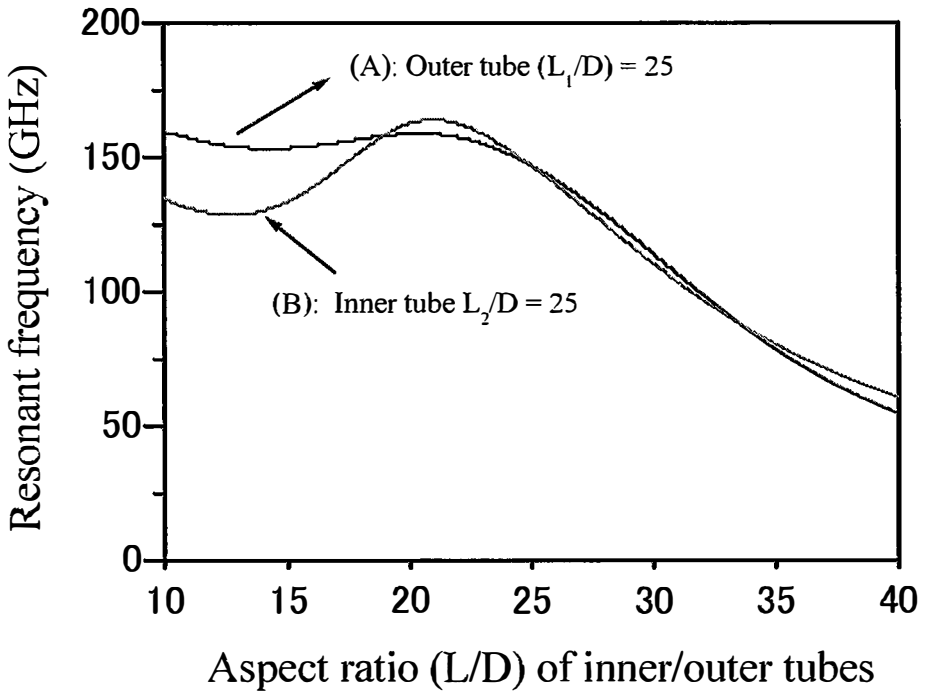

Figure 3.12 Resonant frequencies of cantilevered DWCNTs for vibration mode 2

In the cases of modes 2 and 3, as shown in Figure 3.12 and Figure 3.13, respectively, the resonant frequencies of the DWCNTs change initially in a wave shape and then decrease when lengths of the protruding inner/outer nanotube increase. This can be rationalized by considering that the vibrational frequencies of DWCNTs are affected by the wavelength mismatch between the difference in the lengths of the inner and outer nanotubes. For shorter DWCNTs with an aspect ratio less than 25, the mismatch between the lengths of the inner and outer tubes could significantly affect the frequency response of DWCNTs. The result observed is that frequencies corresponding to two waves occur in mode 2, as shown in Figure 3.12. For the vibration mode 3, three waves are observed in Figure 3.13 because of the influence of the length mismatch on the vibrational mode.

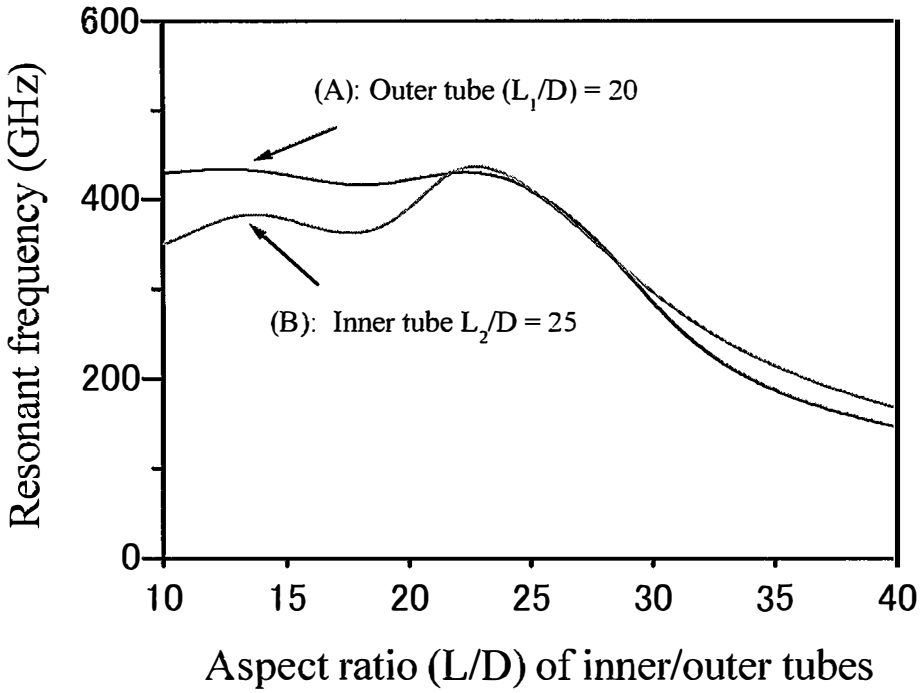

Figure 3.13 Resonant frequencies of cantilevered DWCNTs for vibration mode 3

3.2.4 Conclusions

An analytical procedure based on the Euler-Bernoulli beam model was used to characterize the resonant frequency of cantilevered DWCNTs with inner and outer nanotubes of different lengths. In particular, the present method was used to investigate both the fundamental frequency of DWCNTs and frequencies of higher vibrational modes. The influences of the length mismatch and vibrational modes on the resonant frequencies of DWCNTs were significant, especially for DWCNTs with larger difference between inner and outer tubes. The fundamental vibration (mode 1) of DWCNTs with fixed inner tube length increases initially and then decreases with increasing outer nanotube length. By separately controlling the length mismatch between the inner and outer nanotubes, a nanomechanical resonator based on DWCNT resonators can be easily realized.

References

[1] Q. Wang, V. K. Varadan, Int. J. Solids Struct. **43**, 254 (2006).

[2] C. Y. Wang, C. Q. Ru, A. Mioduchowski, Phys. Rev. B **72**, 075414 (2005).

[3] T. Natsuki, Q. Q. Ni, M. Endo, Carbon **46**, 1570 (2008).

[4] P. Poncharal, Z. L. Wang, D. Ugarte, W. A. de Heer, Science **283**, 1513 (1999).

[5] A. Krishnan, E. Dujardin, T. W. Ebbesen, P. N. Yianilos, M. M. J. Treacy, Phys. Rev. B **58**, 14013 (1998).

[6] L. L. Ke, Y. Xiang, J. Yang, S. Kitipornchai, Compot. Mater. Sci. **47**, 409 (2009).

[7] C. M. Wang, V. B. C. Tan, Y. Y. Zhang, J. Sound Vib. **294**, 1060 (2006).

[8] H. G. Craighead, Science **290**, 1532(2000).

[9] Y. Miyamoto1, S. Saito, and D. Tománek, Phys. Rev. B **65**, 041402(2001).

[10] M. F. Lin, F. L. Shyu, R. B. Chen, Phys. Rev. B **61**, 14114(2000)

[11] Y. Lanir, Y. C. B. Fung, J. Compos. Mater. **6**, 387 (1972).

[12] X. Q. He, S. Kitipornchai, K. M. Liew, J. Mech. Phys. Solids **53**, 303 (2005).

[13] R. Saito, R. Matsuo, T. Kimura, G. Dresselhaus, M. S. Dresselhaus, Chem. Phys. Lett. **348**, 187 (2001).

[14] S. S. Gupta, F. G. Bosco, R. C. Batra, Comput. Mater. Sci. **47,** 1049 (2010).

[15] R. C. Batra, S. S. Gupta, J. Appl. Mech. **75,** 061010 (2008).

[16] S. C. Tsang, P. J. F. Harris, M. L. H. Green, Nature **362**, 520 (1993).

[17] P. G. Collins, M. Hersam, M. Arnold, R. Martel, P. Avouris, Phys. Rev. Lett. **86**, 3128 (2001).

[18] S. Bandow, M. Takizawa, K. Hirahara, M. Yudasaka, S. Iijima, Chem. Phys. Lett. **337,** 48 (2001).

[19] S. Bandow, T. Hiraoka, T. Yumura, K. Hirahara, H. Shinohara, S. Iijima, Chem. Phys. Lett. **384**, 320 (2004).

[20] D. E. Luzzi, B.W. Smith, Carbon **38**, 1751 (2000).

[21] J. Yoon, C. Q. Ru, A. Mioduchowski, Comput. Sci. Technol. **63**, 1533 (2003).

[22] Y. Zhang, G. Liu, X. Han, Phys. Lett. A **340**, 258 (2005).

[23] T. Natsuki, X. W. Lei, Q. Q Ni, M. Endo, Phys. Lett. A **374**, 2670 (2010).

[24] T. Murmu, S. C. Pradhan, Comput. Mater. Sci. **46**, 854 (2009).

[25] S. Malola, H. Häkkinen, P. Koskinen, Phys. Rev. B **78**, 153409 (2008).

[26] Y. M. Fu, J. W. Hong, X. Q. Wang, J. Sound Vib. **296**, 746 (2006).

[27] S. S. Gupta, F. G. Bosco, R. C. Batra, Comput. Mater. Sci. **47**, 1049 (2010).

[28] R. C. Batra, S. S. Gupta, J. Appl. Mech. **75**, 061010 (2008).

CHAPTER FOUR

Surface Effects on the Vibration of Double-Walled Carbon Nanotubes

4 Surface effects on the vibration of double-walled carbon nanotubes

In this chapter, the vibration behaviors of double-walled carbon nanotubes (DWCNTs), accounting for surface effects, are studied based on the nonlocal Bresse-Timoshenko theory. The influences of the surface elasticity modulus, residual surface stress, nonlocal parameter, axial half-wave number and aspect ratio are investigated in detail. The present analysis shows that the effective surface properties influence on the natural frequency of carbon nanotubes (CNTs) are significant. It is shown that the natural frequency is largely affected by the surface material, nonlocal parameter, vibration mode and aspect ratio. Especially in short DWCNTs for the higher vibrational modes, the influence of the nonlocal and surface effects on vibration frequency is more pronounced.

4.1 Introduction

As already mentioned in Chapter 1, carbon nanotubes (CNTs) have been attracted worldwide attention and have a wide range of applications. In the medical field, CNTs are being proposed and actively explored as multipurpose carriers for drug delivery and diagnostic applications [1]. Currently, chemically functionalized CNTs have shown

promise in tumor-targeted accumulation in mice [2]. They also exhibited biocompatibility, excretion and little toxicity. In this case, the active substances could be dissolved in the inner core, and may also be adsorbed as their surfaces adhere to the outer tubes. Because of this, the surface effects, including the surface energy, surface tension, surface relaxation and surface reconstruction should be accounted for when the overall elastic properties of nanostructures are investigated. Due to the increasing ratio of surface area to volume at the nanoscale, the surface effects play important roles in determining the physical and mechanical properties of these materials and cannot be neglected as was demonstrated by Lee and Chang [3], and Guo and Zhao [4].

Recently, considerable attention has been given to investigating the surface effects on nanoscale materials. Feng *et al.* [5] studied surface effects on the elastic modulus of nanoporous materials. They found that the influence of the residual surface stress on the effective modulus was weaker than that of surface elasticity. He and Lilley [6, 7] investigated the effects of surface tension on the static bending of nanowires with cantilever, simply supported and fixed-fixed boundary conditions based on the Young–Laplace equation, and suggested that the overall Young's modulus of nanowires should be studied as a function of the surface effects. Wang and Feng [8] derived an analytical solution for the critical load under uniaxial compression and investigated the surface effects on buckling instability of nanowires. The frequency analyses of nanotubes and nanowires that consider both the internal and external surface effects under various boundary conditions were reported by some researchers [3, 9-11]. Moreover, the surface stress and surface elasticity were recognized as important factors, which may explain the experimentally measured size dependence of the elastic modulus of nanoscale materials [12-15].

Most of the studies have treated nanowires and nanotubes as simple Euler–Bernoulli beams, which neglects the effects of transverse shear deformation and rotary inertia

[16-20]. Unlike this, Wang and Feng [16], and Lee and Chang [21] used the nonlocal Bresse-Timoshenko beam model integrated with surface elasticity theory to discuss the natural frequency of the nanostructures. It has been clearly demonstrated that nonlocal effects played a significant role for nanostructures. Furthermore, the Bresse-Timoshenko beam model worked better than the Euler–Bernoulli beam model when considering the effects of shear deformation and rotary inertia on transverse wave propagation in individual CNTs. Yoon *et al.* [22] discovered this fact while modeling transverse terahertz wave propagation in CNTs. Based on the nonlocal Bresse-Timoshenko beam theory, Wang *et al.* [23] proposed that the nonlocal effect was more significant when dealing with short CNTs with natural frequencies of THz or greater. Lu *et al.* [24] investigated the vibrational behavior of CNTs and reported that the nonlocal parameter $e_0 a$, had a significant influence on the dynamic properties of the beam-like structures based on the nonlocal beam model.

In this chapter, the nonlocal Bresse-Timoshenko beam theory is applied to investigate the surface and small-scale effects on the natural frequency of DWCNTs. The nonlocal elasticity theory constitutes a modified classical elasticity theory [21]. Using the proposed theoretical approach, the influence of the surface and nonlocal effects as well as the aspect ratio on the vibrational modes and frequencies of DWCNTs are investigated. We hope that this study will be helpful in determining the mechanical properties of DWCNTs and designing nano-devices and systems.

4.2 Theoretical analysis

A schematic diagram of a DWCNT with a thin outer surface layer is shown in Figure 4.1; L and h are the length and thickness of the DWCNT, respectively, d is the thickness of the thin surface layer, which approached zero for this calculation method

by Wang and Feng [8].

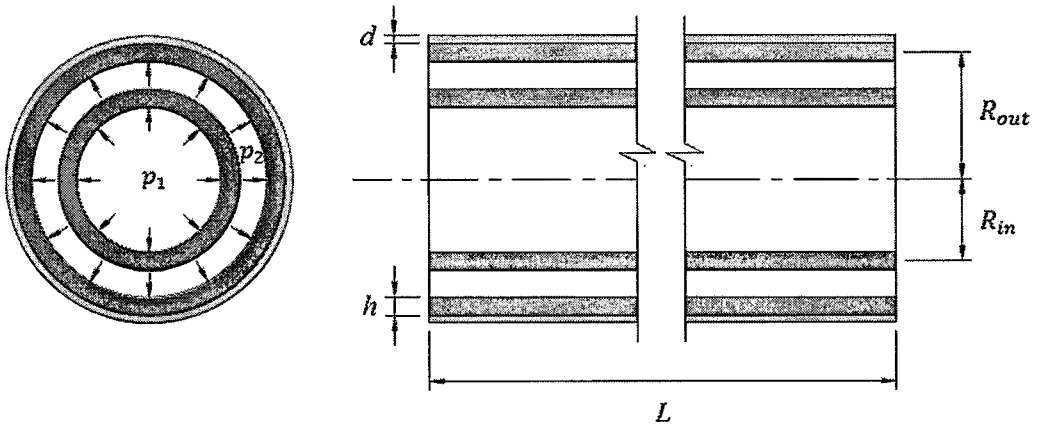

Figure 4.1 Schematic diagram showing transverse and longitudinal cross-sections of the DWCNT model with a surface layer

4.2.1 Nonlocal Bresse-Timoshenko beam theory

For the beam structure, the nonlocal constitutive relations can be given by Lee and Chang [21] and Lu *et al.* [24]:

$$\left[1-(e_0a)^2\frac{\partial^2}{\partial x^2}\right]\sigma = E\varepsilon, \qquad \left[1-(e_0a)^2\frac{\partial^2}{\partial x^2}\right]\tau = G\gamma \tag{4-1}$$

where E and G are the Young's modulus and the shear modulus, respectively, σ and ε are respectively the axial stress and strain, τ and γ are respectively the shear stress and strain. e_0a is the scale coefficient that incorporates the nonlocal effect.

Euler–Bernoulli beam equations of motion for the transversely vibration as expressed by Lee and Chang [21], and Lu *et al.* [24] read:

$$\frac{\partial S}{\partial x}+p=\rho A\frac{\partial^2 w}{\partial t^2}-\frac{\partial}{\partial x}\left(H\frac{\partial w}{\partial x}\right), \qquad \frac{\partial M}{\partial x}+S=\rho I\frac{\partial^2 \varphi}{\partial t^2} \tag{4-2}$$

where w and ϕ are the transverse displacement and the rotation angle of cross section of beam, respectively. p is the distributed transverse force acting along axis x, H is the surface parameter, which is determined by the residual surface tension, ρ is the mass

density per unit volume, t is the time, I is the moment of inertia, S is the resultant shear force on the cross section area A, whereas M is the resultant bending moment, as defined by

$$S = \int_A \tau \, dA, \qquad M = \int_A y\sigma \, dA, \tag{4-3}$$

For the Bresse-Timoshenko beam model, the axial strain ε and the shear strain γ are given by

$$\varepsilon = y\frac{\partial \phi}{\partial x}, \qquad \gamma = \frac{\partial w}{\partial x} - \phi \tag{4-4}$$

The bending moment M and the shear force S are treated as independent variables within the Bresse-Timoshenko beam model. The two resultant forces are linked to the nonlocal stress components σ and ε through the constitutive relations given in Eqs (4-1) and (4-3). According to Eqs (4-1), (4-3) and (4-4), the shear force S and the bending moment M for the nonlocal beam model can be expressed as

$$S - (e_0 a)^2 \frac{\partial^2 S}{\partial x^2} = \kappa GA\left(\frac{\partial w}{\partial x} - \varphi\right), \qquad M - (e_0 a)^2 \frac{\partial^2 M}{\partial x^2} = EI\frac{\partial \varphi}{\partial x} \tag{4-5}$$

where κ is a correction factor depending on the shape of the cross section of the considered beam [24]. By substituting Eq. (4-2) into Eq. (4-5), the explicit expressions of the nonlocal shear force S and bending moment M for the nonlocal beam model can be expressed as follows:

$$\begin{aligned} S &= \kappa GA\left(\frac{\partial w}{\partial x} - \phi\right) + (e_0 a)^2 \left[\rho A \frac{\partial^3 w}{\partial x \partial^2 t} - \frac{\partial p}{\partial x} - \frac{\partial^2}{\partial x^2}\left(H\frac{\partial w}{\partial x}\right)\right] \\ M &= EI\frac{\partial \phi}{\partial x} + (e_0 a)^2 \left[\rho I \frac{\partial^3 \phi}{\partial x \partial^2 t} - \rho A \frac{\partial^2 w}{\partial t^2} + p + \frac{\partial}{\partial x}\left(H\frac{\partial w}{\partial x}\right)\right] \end{aligned} \tag{4-6}$$

By combining Eqs (4-2) and (4-6), the equations of motion for the nonlocal Bresse-Timoshenko beam model can thus be written as

$$EI\frac{\partial^2 \phi}{\partial x^2} + \kappa GA\left(\frac{\partial w}{\partial x} - \phi\right) = \left[1 - (e_0 a)^2 \frac{\partial^2}{\partial x^2}\right] \rho I \frac{\partial^2 \phi}{\partial t^2} \tag{4-7}$$

$$-\kappa GA\left(\frac{\partial^2 w}{\partial x^2}-\frac{\partial \phi}{\partial x}\right)+\left[1-(e_0 a)^2\frac{\partial^2}{\partial x^2}\right]\left[\rho A\frac{\partial^2 w}{\partial t^2}-\frac{\partial}{\partial x}\left(H\frac{\partial w}{\partial x}\right)\right] =\left[1-(e_0 a)^2\frac{\partial^2}{\partial x^2}\right]p \tag{4-8}$$

When $e_0 a$=0, Eqs (4-7) and (4-8) are reduced to the equations of classical Bresse-Timoshenko beam.

By applying Eqs (4-7) and (4-8) to each of the inner and outer nanotubes of the DWCNT, two coupled differential equations are obtained

$$(EI)_i^*\frac{\partial^2 \phi_i}{\partial x^2}+\kappa GA_i\left(\frac{\partial w_i}{\partial x}-\phi_i\right)=\left[1-(e_0 a)^2\frac{\partial^2}{\partial x^2}\right]\rho I_i\frac{\partial^2 \phi_i}{\partial t^2} \tag{4-9}$$

$$-\kappa GA_i\left(\frac{\partial^2 w_i}{\partial x^2}-\frac{\partial \varphi_i}{\partial x}\right)+\left[1-(e_0 a)^2\frac{\partial^2}{\partial x^2}\right]\left[\rho A_i\frac{\partial^2 w_i}{\partial t^2}-\frac{\partial}{\partial x}\left(H_i\frac{\partial w}{\partial x}\right)\right] =\left[1-(e_0 a)^2\frac{\partial^2}{\partial x^2}\right]p_i \tag{4-10}$$

where the subscript i=1 and 2 stand for the inner and the outer tubes of a DWCNT, respectively, $(EI)_i^*$ is the effective flexural rigidity, which includes the surface bending elasticity and the flexural rigidity of DWCNTs considering surface effects, H_i is a constant parameter which determined by the residual surface tension and shape of the cross section. According to Lee and Chang [21], $(EI)_i^*$ and H_i are defined as follows:

$$(EI)_1^* = EI_1, \qquad H_1 = 0, \qquad \text{for the inner tube} \tag{4-11}$$

$$(EI)_2^* = EI_2 + \pi E^s R_{out}^3, \qquad H_2 = 4\tau R_{out}, \qquad \text{for the outer tube} \tag{4-12}$$

where E^S and τ are the surface elasticity modulus and the residual surface tension per length on the outer tube, respectively.

4.2.2 Van der Waals interaction forces

To study the vibrational behavior of DWCNTs, a double-elastic shell model was developed. In this model, it is assumed that each of the nested tubes in a DWCNT is an individual elastic shell, and the adjacent tubes are coupled to each other by normal van der Waals interactions. As discussed in Chapter 3, the pressures from the van der Waals forces exerted on the inner and outer nanotubes are given as:

$$p_1 = c(w_2 - w_1) \tag{4-13}$$

$$p_2 = c(w_1 - w_2) \tag{4-14}$$

where w_i are the radial displacements of the ith nanotube (i=1 for the inner tube, and i=2 for the outer tube), c is the van der Waals interaction coefficient between the inner and outer nanotubes, which can be estimated from the Lennard–Jones potential [25]:

$$c = \frac{\pi\varepsilon R_{in} R_{out} \sigma^6}{3a^4}\left[\frac{1120}{3} H^7 - 1001\sigma^6 H^{13}\right] \tag{4-15}$$

where

$$H^m = (R_{in} + R_{out})^{-m} \int_0^{\frac{\pi}{2}} \frac{d\theta}{(1 - K\cos^2\theta)^{\frac{m}{2}}} \qquad (m = 7,13) \tag{4-16}$$

and

$$K = \frac{4R_{in}R_{out}}{(R_{in} + R_{out})^2} \tag{4-17}$$

where a is the carbon–carbon bond length (0.142 nm), R_{in} and R_{out} are the inner and outer radii of the DWCNTs, respectively, σ and ε are the van der Waals radius and the well depth of the Lennard–Jones potential, respectively.

4.2.3 Natural vibration of DWCNTs

Consider a simply supported DWCNT with length L. The boundary conditions read:

$$w_i(0,t) = w_i(L,t) = 0 \qquad (i = 1, 2) \tag{4-18}$$

$$\frac{\partial \varphi_i(0,t)}{\partial x} = \frac{\partial \varphi_i(L,t)}{\partial x} = 0 \qquad (i = 1, 2) \tag{4-19}$$

To satisfy the boundary conditions given by Eqs (4-18) and (4-19), the displacement field for a DWCNT is given by

$$w_i(x,t) = W_i \sin\frac{m\pi x}{L} \sin\omega t \qquad (i = 1, 2) \tag{4-20}$$

$$\varphi_i(x,t) = \Phi_i \cos\frac{m\pi x}{L} \sin\omega t \qquad (i = 1, 2) \tag{4-21}$$

where W_1 , W_2 represent the modal amplitudes of the deflections of the inner and the outer tubes, respectively and Φ_1, Φ_2 represent the modal amplitudes of the slopes of the inner and outer tubes due to bending deformations, respectively. The integer m is the number of half-waves in the axial direction, whereas ω is the circular frequency.

By substituting Eqs (4-11)-(4-14) into Eqs (4-9) and (4-10), we obtain the governing equations of transverse vibration for the inner and outer tubes:

$$\begin{bmatrix} L_{11} & L_{12} & L_{13} & L_{14} \\ L_{21} & L_{22} & L_{23} & L_{24} \\ L_{31} & L_{32} & L_{33} & L_{34} \\ L_{41} & L_{42} & L_{43} & L_{44} \end{bmatrix} \begin{Bmatrix} \varphi_1 \\ w_1 \\ \varphi_2 \\ w_2 \end{Bmatrix} = 0 \tag{4-22}$$

where L_{ij} are the following differential operators:

$$
\begin{aligned}
L_{11} &= EI_1 \frac{\partial^2}{\partial x^2} - \kappa GA_1 - \rho I_1 \frac{\partial^2}{\partial t^2} + \rho I_1 (e_0 a)^2 \frac{\partial^4}{\partial x^2 \partial t^2} \\
L_{12} &= \kappa GA_1 \frac{\partial}{\partial x} \\
L_{21} &= -\kappa GA_1 \frac{\partial}{\partial x} \\
L_{22} &= \kappa GA_1 \frac{\partial^2}{\partial x^2} + c(e_0 a)^2 \frac{\partial^2}{\partial x^2} - \rho A_1 \frac{\partial^2}{\partial t^2} + \rho A_1 (e_0 a)^2 \frac{\partial^4}{\partial x^2 \partial t^2} - c \\
L_{24} &= -c(e_0 a)^2 \frac{\partial^2}{\partial x^2} + c \\
L_{33} &= (EI_2 + \pi E^s R_{out}^3) \frac{\partial^2}{\partial x^2} - \kappa GA_2 - \rho I_2 \frac{\partial^2}{\partial t^2} + \rho I_2 (e_0 a)^2 \frac{\partial^4}{\partial x^2 \partial t^2} \\
L_{34} &= \kappa GA_2 \frac{\partial}{\partial x} \\
L_{42} &= -c(e_0 a)^2 \frac{\partial^2}{\partial x^2} + c \\
L_{43} &= -\kappa GA_2 \frac{\partial}{\partial x} \\
L_{44} &= \kappa GA_2 \frac{\partial^2}{\partial x^2} + c(e_0 a)^2 \frac{\partial^2}{\partial x^2} - \rho A_2 \frac{\partial^2}{\partial t^2} + \rho A_2 (e_0 a)^2 \frac{\partial^4}{\partial x^2 \partial t^2} - c \\
&\quad + H_2 \frac{\partial^2}{\partial x^2} \left[1 - (e_0 a)^2 \frac{\partial^2}{\partial x^2} \right] \\
L_{13} &= L_{14} = L_{23} = L_{31} = L_{32} = L_{41} = 0
\end{aligned}
\tag{4-23}
$$

By substituting Eqs (4-20) and (4-21) into Eq (4-22), the natural frequencies of DWCNTs considering surface effects can be determined using a nontrivial solution of Eq. (4-22), expressed as a determinantal equation:

$$
\begin{vmatrix}
A_{11} & A_{12} & A_{13} & A_{14} \\
A_{21} & A_{22} & A_{23} & A_{24} \\
A_{31} & A_{32} & A_{33} & A_{34} \\
A_{41} & A_{42} & A_{43} & A_{44}
\end{vmatrix} = 0
\tag{4-24}
$$

where

$$A_{11} = -EI_1\left(\frac{m\pi}{L}\right)^2 - \kappa GA_1 + \rho I_1\omega^2 + \rho I_1(e_0a)^2\left(\frac{m\pi}{L}\right)^2\omega^2$$

$$A_{12} = \kappa GA_1\frac{m\pi}{L}$$

$$A_{21} = -\kappa GA_1\frac{m\pi}{L}$$

$$A_{22} = -\kappa GA_1\left(\frac{m\pi}{L}\right)^2 - c(e_0a)^2\left(\frac{m\pi}{L}\right)^2 + \rho A_1\omega^2 + \rho A_1(e_0a)^2\left(\frac{m\pi}{L}\right)^2\omega^2$$

$$A_{24} = c(e_0a)^2\left(\frac{m\pi}{L}\right)^2 + c$$

$$A_{33} = -\left(EI_2 + \pi E^s R_{out}^3\right)\left(\frac{m\pi}{L}\right)^2 - \kappa GA_2 + \rho I_2\omega^2 + \rho I_2(e_0a)^2\left(\frac{m\pi}{L}\right)^2\omega^2 \qquad (4\text{-}25)$$

$$A_{34} = \kappa GA_2\frac{m\pi}{L}$$

$$A_{42} = c(e_0a)^2\left(\frac{m\pi}{L}\right)^2 + c$$

$$A_{43} = \kappa GA_2\frac{m\pi}{L}$$

$$A_{44} = -\kappa GA_2\left(\frac{m\pi}{L}\right)^2 - c(e_0a)^2\left(\frac{m\pi}{L}\right)^2 + \rho A_2\omega^2 + \rho A_2(e_0a)^2\left(\frac{m\pi}{L}\right)^2\omega^2$$
$$-c - H_2\omega^2\left[1 + (e_0a)^2\omega^2\right]$$

$$A_{13} = A_{14} = A_{23} = A_{31} = A_{32} = A_{41} = 0$$

4.2.4 Free vibration of embedded DWCNTs

The Winkler spring model has been widely used to study the vibration properties of embedded CNTs [26-28]. The pressure per unit axial length, p_w, acting on the outer tubes embedded to elastic medium can be given by

$$p_w = -c_m w_2 \qquad (4\text{-}26)$$

where the negative sign indicates that the pressure is opposite to the deflection of the nanotube, c_m is a spring constant determined by the material constants of the elastic medium, the diameter of embedded CNTs, and its wavelength [29]. Instead of the Eqs (4-13) and (4-14), the pressures p_i (i=1 for the inner tube, and i=2 for the outer tube) of embedded DWNTs can be cast as

$$p_1 = c(w_2 - w_1) \tag{4-27}$$

$$p_2 = p_w + c(w_1 - w_2) = cw_1 - (c + c_m)w_2 \tag{4-28}$$

Substituting Eqs (4-27) and (4-28) into Eqs (4-9) and (4-10), and using the Eqs (4-20) and (4-21), a nontrivial solution can be obtained to analyze the natural frequency of embedded DWNTs, given as Eq. (4-24). For the solution of the natural frequencies of DWNTs embedded in elastic medium, the terms of Eq. (4-25) can also be used after altering the term of A_{44} as follows:

$$\begin{aligned} A_{44} = &-\kappa G A_2 \left(\frac{m\pi}{L}\right)^2 - (c + c_m)(e_0 a)^2 \left(\frac{m\pi}{L}\right)^2 + \rho A_2 \omega^2 \\ &+ \rho A_2 (e_0 a)^2 \left(\frac{m\pi}{L}\right)^2 \omega^2 - (c + c_m) - H_2 \left(\frac{m\pi}{L}\right)^2 \left[1 + (e_0 a)^2 \left(\frac{m\pi}{L}\right)^2\right] \end{aligned} \tag{4-29}$$

4.3 Results and discussion

Using this theoretical approach, the influence of the surface material, nonlocal parameter, aspect ratio and vibrational mode on the natural frequency are investigated hereinafter. We consider a DWCNT with inner and outer diameters of 2.2 and 3.0 nm, respectively. The DWCNTs have a Young's modulus of 1.0 TPa, Poisson's ratio of 0.27 and the mass density of 2.3 g/cm^3. The layer thickness of the DWCNT was assumed to be that of a graphite sheet with a thickness of 0.34 nm [30]. The van der

Waals parameters in the Lennard–Jones potential are σ = 0.34 nm and ε = 2.967 meV, which were reported by Saito [31]. The dependence of the shear coefficient κ is about 0.6-0.7 for thin-walled circular cross-section and 0.9 for a solid circular cross-section. For the DWCNT, we take the shear coefficient κ to be 0.8, given by Yoon, Ru and Mioduchowski [32].

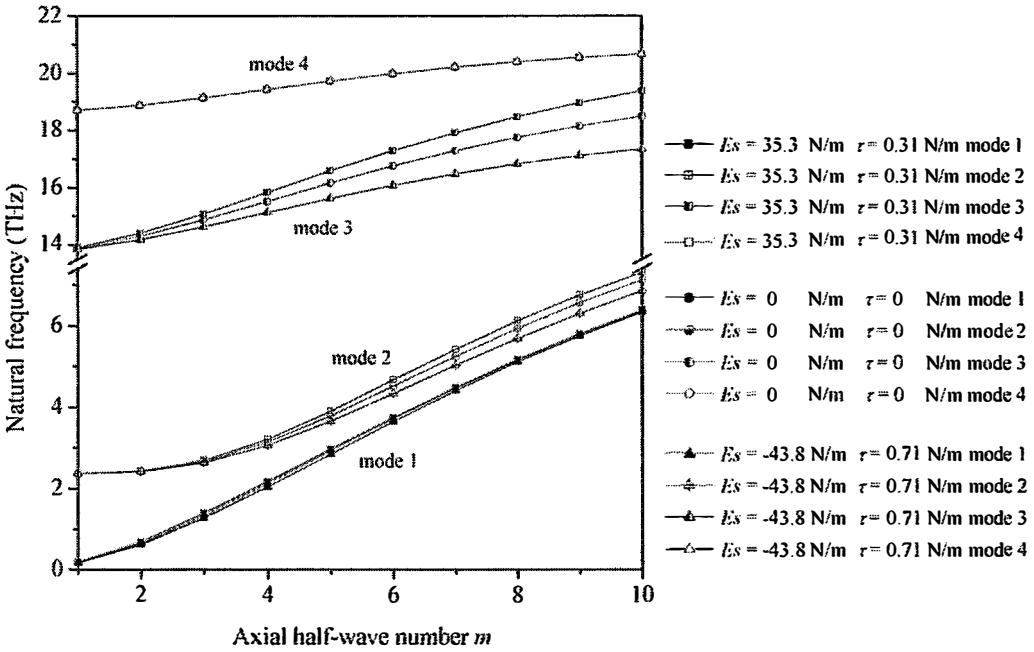

Figure 4.2 Comparison of the natural frequencies of DWCNTs with various surface elasticity and surface stress values as a function of the axial half-wave number of the vibrational mode ($L/2R_{our}$ = 10, e_0a =1 nm)

Figures 4.2 and 4.3 describe the first four natural frequencies of the DWCNT when the influence of surface elasticity modulus and the residual surface stress on the outer tubes are included. The analytical result shows that they depend on the material property and the surface crystal orientation. For the theoretical calculations using (112) and (001) nickel, the surface elasticity and surface stress values were obtained using atomistic calculations that yielded values of E^S=35.3 N/m and τ=0.31 N/m, and E^S=-43.8 N/m and τ=0.71 N/m. The surface elastic modulus E^S is obtained from

surface elastic constants S_{1111} and S_{1122}, which were calculated by Shenoy (2005) according to the formula of $E^S=(S_{1111}+2S_{1122})(S_{1111}-S_{1122})/(S_{1111}+2S_{1122})$ [6,7].

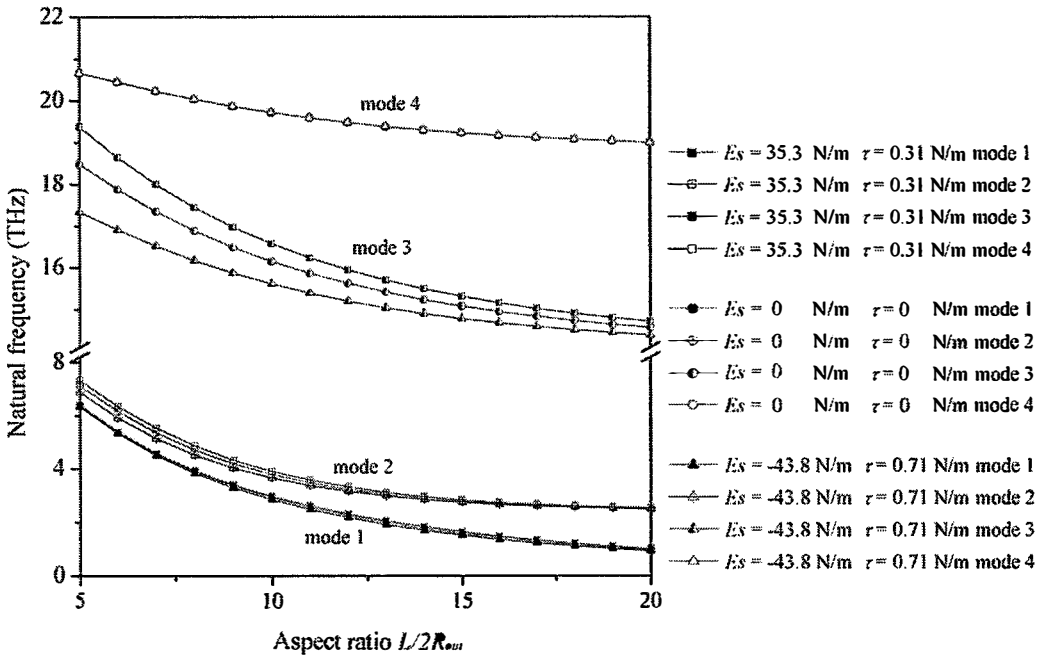

Figure 4.3 Comparison of the natural frequencies of DWCNTs with various surface elasticity and surface stress values as a function of aspect ratio ($m = 5$, e_0a =1 nm)

The dependence between the natural frequency and the number of half-waves is shown in Figure 4.2. As the axial half-wave number increases, the natural frequency of the DWCNTs, which have four modes and are covered with different crystal surfaces, also increases. As is observed, four frequency series are reported. The four modes include the axial and rotational vibrations in both inner and outer nanotubes. It can be seen that the surface effective elastic modulus and residual stress have an influence on the natural frequencies of DWCNTs. When the axial half-wave mode increases from 1 to 10, the surface effect becomes more and more pronounced. In mode 3, comparing the results between (112) and (001) nickel covered DWCNTs, there is an 11.7%

variation in the natural frequency when the vibrational mode number reaches 10.

The relationship between the natural frequency and the aspect ratio of the DWCNTs is presented in Figure 4.3. The influence of the surface parameters is considerably higher for lower aspect ratio CNTs. As the aspect ratio of the DWCNTs increases, the surface effects diminish, and the results converge to two distinct branches which are close to the natural frequency of the DWCNTs without surface material. For a short DWCNT, the surface-to-volume ratio is much larger than that of a slender one. It is observed that the natural frequency of mode 4 of the DWCNTs is not significantly affected by the surface material regardless of vibrational mode or aspect ratio.

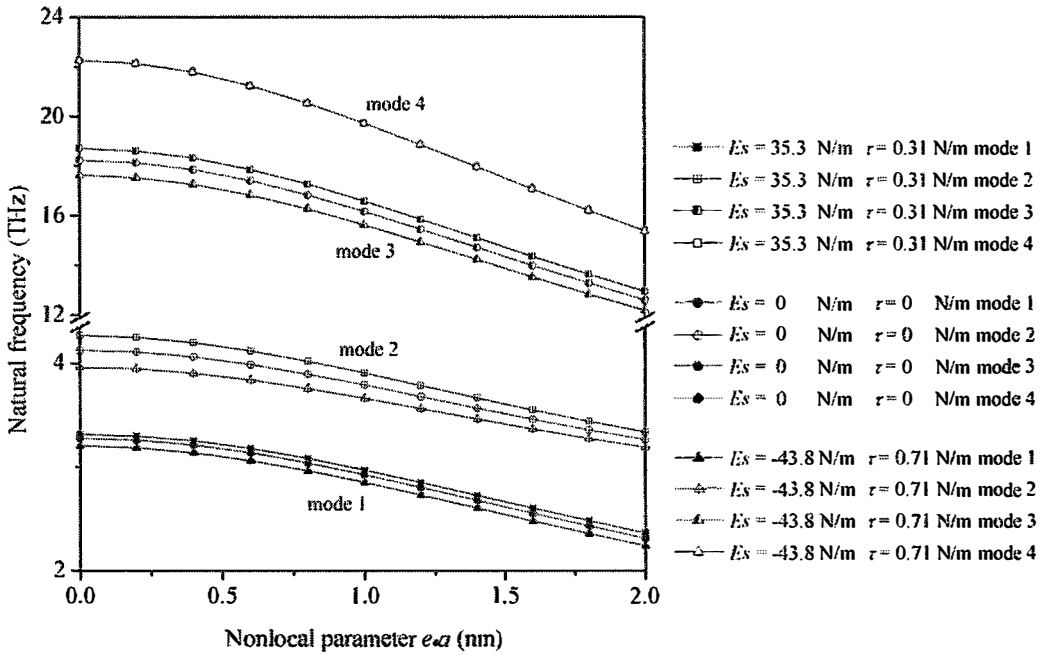

Figure 4.4 Comparison of the natural frequencies of DWCNTs with various surface elasticity and surface stress values as a function of the nonlocal parameter ($L/2R_{out} = 10$, $m = 5$)

Figure 4.4 shows the relationship between the nonlocal parameter e_0a and the natural frequency of DWCNTs with different vibrational modes. From the figure, it can be seen that the natural frequency of DWCNTs decrease with increasing scale

coefficient. The influence of the nonlocal parameter in modes 3 and 4, which has higher natural frequencies, is much larger than those in modes 1 and 2. The natural frequencies of the DWCNTs covered with surface materials with positive and negative surface elastic moduli surround those of the DWCNTs without surface materials. The negative modulus may occur in a predeformed object; it is then a negative incremental modulus [33,34] presented numerical results for two different orientations one for which the surface moduli are negative (surface [100]) while positive for the other [111].

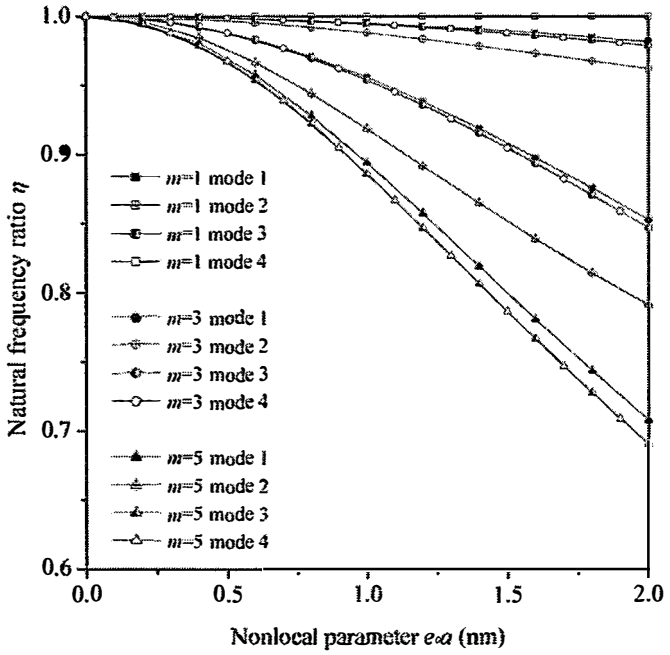

Figure 4.5 Comparison of the natural frequency ratio of DWCNTs with various axial half-wave numbers as a function of the nonlocal parameter ($L/2R_{out}$ = 10, E^S=1.22 N/m, τ=0.89 N/m)

To illustrate the influence of nonlocal effects on the vibrational frequency, we defined the frequency ratio as the number η representing the ratio of the frequency evaluated by nonlocal Bresse-Timoshenko to that of local Bresse-Timoshenko beams. In addition to the nonlocal effect, the nonlocal Bresse-Timoshenko beam model is also

dominated by the effects of the vibrational mode and the aspect ratio.

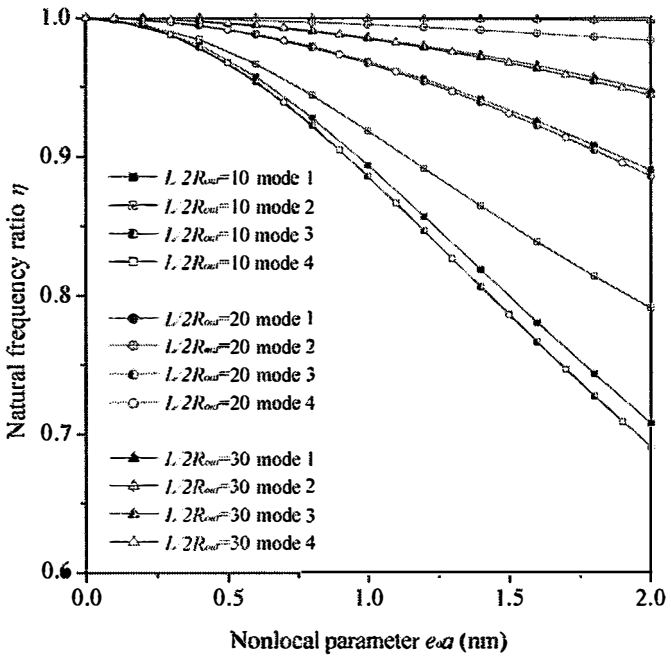

Figure 4.6 Comparison of the natural frequency ratio of DWCNTs with various aspect ratios as a function of the nonlocal parameter (m = 1, E^S=1.22 N/m, τ =0.89 N/m)

Figures 4.5 and 4.6 show the relationship between the frequency ratio and the nonlocal parameter of the DWCNTs with different vibrational modes. This is achieved by considering the influence of vibrational mode and aspect ratio, in which the surface parameters of (001) single-crystal silver (E^S=1.22 N/m and τ =0.89 N/m) are used. The frequency ratio serves as a quantitative index of assessing the nonlocal effect of DWCNTs on the vibrational solutions. We find from Figure 4.5 that the frequency ratio is less than unity for all four modes with various axial half-wave numbers. This means that the natural frequency of the DWCNTs calculated using local theory will be the largest one. As the scale coefficient e_0a increases, the values of natural frequencies obtained from the nonlocal Bresse-Timoshenko beam become smaller than those obtained from the local counterpart. For example, consider DWCNTs with m = 5,

$L/2R_{out}$ = 10 in mode 1. When the scale coefficient increases from 0 to 2.0 nm, the frequency decreases from 3.28 THz to 2.32 THz, corresponding to a reduction of over 40%. Note that at higher vibrational modes (the higher axial-wave number), the frequency ratio is farther from unity. This means that the analytical results obtained from the local and nonlocal Bresse-Timoshenko beam models may turn out to be quite different for high vibrational frequency.

Variations of the frequency ratio versus the scale coefficient for the four vibrational modes of DWCNTs with different aspect ratios are plotted in Figure 4.6. The frequency ratio parameters decrease as the nonlocal parameter increases. Meanwhile, the natural frequencies of the DWCNTs decrease when the nonlocal Bresse-Timoshenko beam model is used to analyze vibration behavior. It can be seen that the scale coefficient $e_0 a$ plays a larger role in shorter DWCNTs. Conversely, for a slender DWCNT with aspect ratio of 30, the frequency ratio approaches unity. This indicates a reduction in the nonlocal effect on the natural frequency of DWCNTs. In summary, the nonlocal effect is significant for small length-to-diameter ratios of DWCNTs, and can be neglected in longer nanotubes.

The frequency variation of embedded DWCNTs with aspect ratio and nonlocal parameter are investigated in Figures 4.7 and 4.8; c_m is a spring constant determined mainly by the material constants of the elastic medium and diameter of the embedded CNTs. In this simulation, we take the ratio c_m/c as a parameter considering the different sorts of surrounding media. The values of the ratio c_m/c are taken as 0.1, 1, and 10. From Figure 4.7, we see that the natural frequency of a DWCNT decreases rapidly with increasing aspect ratio. For larger aspect ratios of DWCNTs, the natural frequency is significantly affected by the elastic medium around the DWCNTs. When the DWCNTs are embedded in an elastic medium with c_m/c=10, the variation of the natural frequency tends to stabilize with increasing nanotube length.

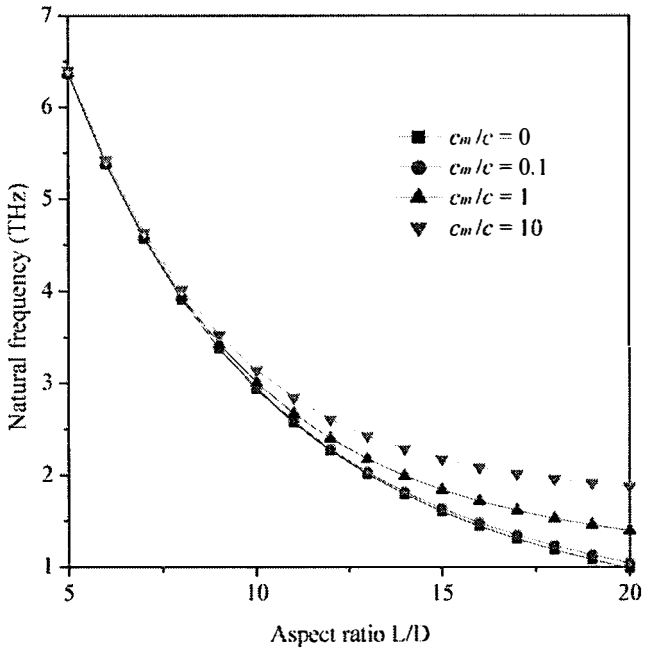

Figure 4.7 Vibration of the natural frequency with aspect ratio of embedded DWCNTs ($L/2R_{our}$ = 10, m = 5, E^S=1.22 N/m, τ =0.89 N/m)

Figure 4.8 depicts the relationship between the nonlocal parameter and the frequency ratio (nonlocal/local Bresse-Timoshenko beam) of DWCNTs embedded in different elastic media. It is seen that the frequency ratio decreases with increasing nonlocal parameter. However, the natural frequency becomes less sensitive to the nonlocal parameter for DWCNTs embedded in elastic medium with large c_m/c ratio. This suggests that the local Bresse-Timoshenko beam can be adapted to shorter nanotubes when they are embedded in an elastic medium with large c_m/c.

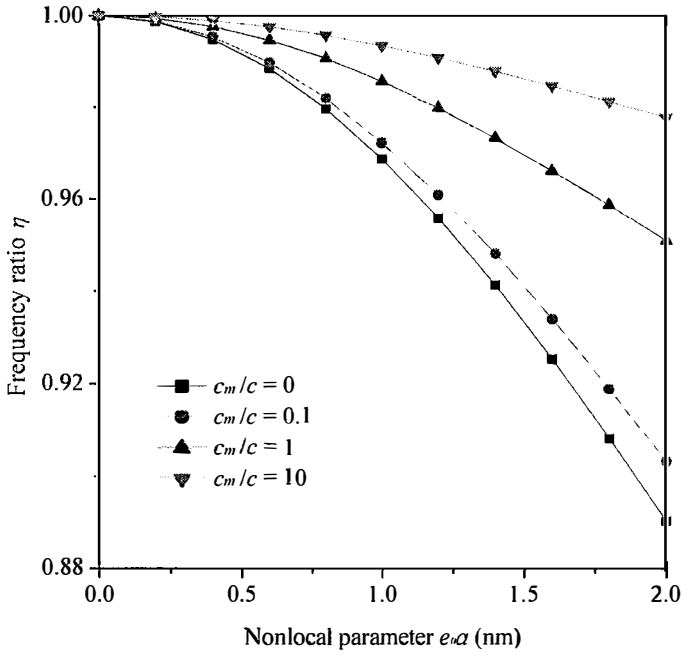

Figure 4.8 Variation of the natural frequency ratio with nonlocal parameters (e_0a=1 nm, m = 5, E^S=1.22 N/m, τ =0.89 N/m)

4.3 Conclusions

An analytical procedure based on the nonlocal Bresse-Timoshenko beam mode was used to investigate the vibrational behavior of DWCNTs adhered by surface materials and embedded in elastic media. The influence of the surface materials and the nonlocal parameter on the natural frequency is significant, especially for higher vibrational modes and shorter nanotube length. The present chapter many prove useful for further understanding the vibration properties of DWCNTs. This investigation may be helpful in application of carbon nanotubes such as high oscillators, structural elements of nanodevices, and mechanical sensors since CNTs are small in size and have terahertz-frequency vibration.

References

[1] M. Prato, K. Kostarelosk, A. Bianco, Acc. Chem. Res. **41**, 60 (2008)

[2] Z. Liu, K. Chen, C. Davis, S. Sherlock, Q. Z. Cao, X. Y. Chen, H. J. Dai, Cancer Res. **68**, 6652 (2008)

[3] H. L. Lee, W. J. Chang. J. Appl. Phys. **108**, 093503 (2010)

[4] J. G. Guo, Y. P. Zhao, Nanotechnology **18**, 295701 (2007)

[5] X. Q. Feng , R. Xia, X. D. Li, B. Li, Appl. Phys. Lett. **94**, 011916 (2009)

[6] J. He, C.M. Lilley, Appl. Phys. Lett. **93**, 263108 (2008)

[7] J. He, C.M. Lilley, Nano Lett. **8**, 1798 (2008)

[8] G. F. Wang, X. Q. Feng, Appl. Phys. Lett. **94**,141913 (2009)

[9] M. E. Gurtina, J. Weissmullerb, F. Larche, Philox Mag A **78**, 1093 (1998)

[10] G. F. Wang, X. Q. Feng, Appl. Phys. Lett. **90**, 231904 (2007)

[11] B. Farshi, A. Assadi, A. Alinia-ziazi, Appl. Phys. Lett. **96**, 093105 (2010)

[12] G. Y. Jing, H. L. Duan , X. M. Sun, Z. S. Zhang , J. Xu, Y. D. Li, J. X. Wang, D. P. Yu, Phys. Rev. B **73**, 235409 (2006)

[13] Y. Geng, H. S. Park, Phys. Rev. B **79**, 195421 (2009)

[14] P. Sharm, S. Ganti, N. Bhate, Appl. Phys. Lett. **82**, 535 (2003)

[15] Z. Q. Wang, Y. P. Zhao, Z. P. Huang, Int. J. Eng. Sci. **48**, 140 (2010)

[16] G. F. Wang, X. Q. Feng, J. Phys. D **42**, 155411 (2009)

[17] N. Hu, K. Nunoyab, D. Panc, T. Okabeb, H. Fukunagab, Int. J. Solids Struct. **44**, 6535 (2007)

[18] N. Hu, H. Fukunaga, C. Lu, M. Kameyama, B. Yan, P. Roy. Soc. A-Math Phy. **461**, 1685 (2005)

[19] C. Y. Li, T. W. Chou, Int. J. Solids. Struct. **40**, 2487 (2003)

[20] Z. Q. Wang, Y. P. Zhao, Acta. Mech. Solida Sin. **22**, 630 (2009)

[21] H. L. Lee, W. J. Chang, J. Appl. Phys. **108**, 093503 (2010)

[22] J. Yoon, C. Q. Ru, A. Mioduchowski, Composites Part B **35**, 87 (2004)

[23] C. M. Wang, Y. Y. Zhang, X. Q. He, Nanotechnology **18**, 105401 (2007)

[24] P. Lu, H. P. Lee, C. Lu, P. Q. Zhang, Int. J. Solids Struct. **44**, 5289 (2007)

[25] X. Q. He, S. Kitipornchai, K. M. Liew, J. Mech. Phys. Solids **53**, 303 (2005)

[26] J. Yoon, C. Q. Ru, A. Mioduchowski, Compos. Sci. Tech. **63**, 1533 (2003)

[27] T. Natsuki, T. Hayashi, M. Endo, J. Appl. Phys. **97**, 044307 (2005)

[28] T. Natsuki, M. Endo, H. Tsuda, J. Appl. Phys. **99**, 034311 (2006)

[29] Y. Lanir, Y. C. B. Fung, J. Compos. Mater. **6** 387 (1972)

[30] T. Natsuki, T. Tsuchiya, Q. Q. Ni, M. Endo, Carbon **48**, 4362 (2008)

[31] R. Saito, R. Matsuo, T. Kimura, G. Dresselhaus, M. S. Dresselhaus, Chem. Phys. Lett. **348**, 187 (2001)

[32] J. Yoon, C. Q. Ru, A. Mioduchowski, J. Appl. Mech. **72**, 10 (2005)

[33] T. Jaglinski, D. Kochmann, D. Stone, R. S. Lakes, Science **315**, 620 (2007).

[34] P. Sharma, S. Ganti, N. Bhate Appl. Phys. Lett. **82**, 535 (2003)

CHAPTER FIVE

Radial Breathing Vibration of Carbon Nanotubes

5 Radial breathing vibration of carbon nanotubes

As mentioned above in Chapter 3 and Chapter 4, the beam model based on Euler–Bernoulli theory and the Bresse-Timoshenko beam theory of continuum mechanical models can effectively used to study mechanical behaviors of carbon nanotubes. For the vibration property of CNT in radial direction and circumference direction cannot be solved by beam model but can be analysis using continuum shell model, in this chapter we will build shell model of CNTs to analyze the vibration behavoure in radial direction. According to Ru [1], "when aspect ratios L/R_0 of CNTs are small, or local deformation is concerned, CNTs should be treated as elastic cylindrical *shell* rather than elastic *beam* when modes having two or more circumferential waves $n \geq 2$. Radial breathing mode (RBM) of carbon nanotubes (CNTs) is a low frequency mode, but accounts for the strongest feature observed in the CNT Raman spectrum. For the RBM, all of the carbon atoms in a CNT move in the radial direction synchronously, which generates an effect similar to "breathing" [2, 3]. This mode is unique to CNTs, and is not observed in other carbon systems [4].

Raman spectroscopy has been widely recognized as a powerful nondestructive technique for characterizing the structural properties of CNTs because of better sensitivity and lower cost than other methods [2]. Raman spectra contain different features including the radial breathing mode (RBM), where all of the carbon atoms are

subject to an in-phase radial displacement, the G-band, where neighboring atoms move in opposite directions along the surface of the tube as in 2D graphite, the dispersive disorder-induced D-band and its second order related harmonic G'-band. Of these, the RBM appears at the lowest frequency but is the strongest feature observed. In the RBM, all of the carbon atoms in a CNT move in a radial direction synchronously as if the tube is "breathing" [2, 5]. This mode is unique to CNTs, and is not observed in other carbon systems [6].

Application of pressure to condensed matter systems is an ideal way to continuously modify the bonding properties of a solid, which affect virtually all of the properties of a material [7]. In the context of CNTs, pressure studies are motivated by the needs to investigate the mechanical stability, pressure–induced phase transitions like vibrational characteristics, and the effects of intertube interactions. The vibrational properties of nanotubes in a high-pressure diamond anvil cell (DAC) can be readily investigated by Raman spectroscopy [8].

The frequency of the RBM of CNTs under pressure has mainly been probed using Raman spectroscopy [9-12]. Schlecht *et al.* [9] studied isolated single-walled carbon nanotubes (SWCNTs) under pressure experimentally and found that the frequency dependence of the optical mode in bundled and isolated SWCNTs was identical. Using generalized tight-binding molecular dynamics, Venkateswaran *et al.* [10, 11] showed that van der Waals (vdW) interactions make an important contribution to the frequency of the RBM of bundled and unbundled CNTs and impact its pressure dependence strongly. During consideration of the structure characteristics of CNTs, Lebedkin *et al.* [12] demonstrated that it is possible to study pressure effects on individual unbundled SWCNTs using a DAC and a sensitive Raman spectrometer. The position of the RBM has been reported to be sensitive to excitation wavelength [13, 14], external pressure [15, 16], dopant type [17], and the size of the nanotube bundle [18]. Arvanitidis *et al.* [8]

used detailed pressure Raman experiments to determine the strength of intra-tube interactions of bundled double-walled carbon nanotubes (DWCNTs). Gadagkar *et al.* [19] focused on the responses of the inner and outer tubes of DWCNTs, and investigated the behavior of DWCNT bundles under pressure. Puech *et al.* [20, 21] examined the stability of DWCNTs under hydrostatic pressures, and compared Raman spectra obtained under different hydrostatic pressures using two different pressure media.

Computational simulation has been regarded as a powerful tool for predicting the frequency of the RBM of CNTs under hydrostatic pressure, comparing with the difficulty of the experiment. Lawler and Kurti *et al.* [22, 23] presented first-principle calculations for the RBM of bundled SWCNTs. A study exploring the frequencies and mode shapes of the RBM of various CNTs using a modified molecular structural mechanics model was reported by Cheng *et al.* [6]. Based on a multiple-elastic shell model, Wang *et al.* [24] showed that the frequencies of the RBM of MWCNTs generally increase as the external pressure increases, and the effects of pressure are associated with RBMs of different frequency for MWCNTs with innermost tubes of different diameter. Recent reviews focusing on Raman spectroscopy on CNTs [2] and CNTs under pressure [5] summarized past achievements in the field and highlighted promising directions for future development, especially in experimental studies.

5.1 Carbon nanotubes subjected to hydrostatic pressure

5.1.1 Introduction

In this section, the frequency of the RBM of CNTs subjected to pressure, is studied using an elastic continuum mechanics model. DWCNTs can be considered a kind of MWCNT where the interlayer interaction between the inner and outer nanotubes is

generally turbostratic [2, 5]. The influences of the axial half-wave number m, circumference wave number n, nanotube radius, aspect ratio L/D of nanotubes on the frequency of the RBM of the inner and outer tubes in DWCNTs under varying pressure are considered. Compared to previous results obtained from experimental investigations, the continuum shell model can be used to predict the frequency of the RBM of CNTs under pressure reasonably. This investigation will be helpful in nanodevice technologies such as nanoprobes and nanosensors.

5.1.2 Theoretical approach

5.1.2.1 Governing equations of DWCNTs under pressure

A continuum elastic shell model (Figure 5.1) was used to analyze the characteristics of the RBM of CNTs subjected to pressure. The cylindrical shell is designated as a coordinate system (x, θ, z). The coordinates x, θ, and z refer to the axial, circumferential and radial directions, respectively. The displacements of CNTs are u, v and w corresponding to the x, θ, and z directions, respectively. The dimensions of the nanotubes are defined as the thickness h, radius R, length L and Poisson's ratio υ.

Based on our previous work [25, 26], the external forces N and moment M resultants are respectively defined as

$$\{N_x, N_\theta, N_{x\theta}, N_{\theta x}\} = \frac{Eh}{1-\nu^2}\{\varepsilon_1 + \upsilon\varepsilon_2, \varepsilon_2 + \upsilon\varepsilon_1, \gamma(1-\upsilon)/2, \gamma(1-\upsilon)/2\} \tag{5-1}$$

$$\{M_x, M_\theta, M_{x\theta}, M_{\theta x}\} = -D\{\chi_x - \upsilon\chi_\theta, \chi_\theta + \upsilon\chi_x, (\upsilon-1)\chi_{x\theta}, (1-\upsilon)\chi_{x\theta}\} \tag{5-2}$$

where E is Young' modulus of CNTs.

$$D = \frac{Eh^3}{12(1-\upsilon^2)} \tag{5-3}$$

$$\varepsilon_1 = \frac{\partial u}{\partial x} \qquad \varepsilon_2 = \frac{\partial v}{R\partial\theta} - \frac{w}{R} \qquad \gamma = \frac{\partial u}{R\partial\theta} + \frac{\partial v}{\partial x} \tag{5-4}$$

$$\chi_x = \frac{\partial^2 w}{\partial x^2} \qquad \chi_\theta = \frac{1}{R^2}\left(\frac{\partial v}{\partial \theta} + \frac{\partial^2 w}{\partial \theta^2}\right) \qquad \chi_{x\theta} = \frac{1}{R}\left(\frac{\partial v}{\partial x} + \frac{\partial^2 w}{\partial x \partial \theta}\right) \tag{5-5}$$

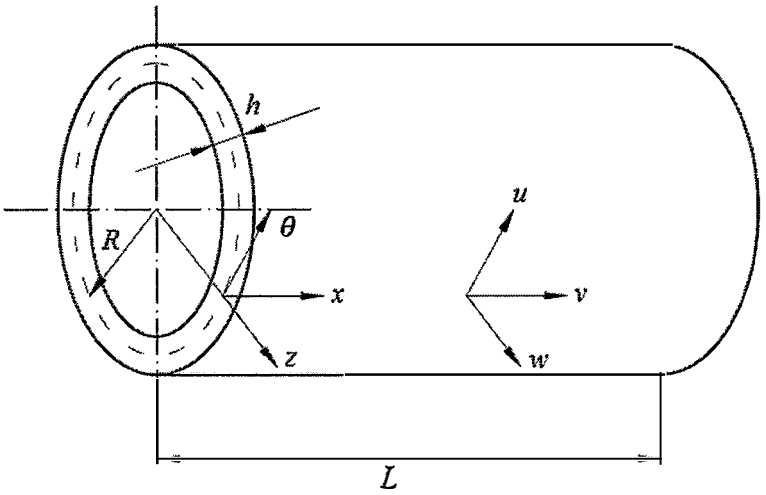

Figure 5.1 Schematic diagram showing the cylindrical coordinates of the CNT model used for analysis

We considered the vibration of CNTs in the radial direction according to Love's first approximation shell theory. Therefore, the equilibrium equations of the three external forces and moments acting on CNTs are given by

$$R\frac{\partial N_x}{\partial x} + \frac{\partial N_{\theta x}}{\partial \theta} - N_\theta\left(\frac{\partial^2 v}{\partial x \partial \theta} - \frac{\partial w}{\partial x}\right) = 0 \tag{5-6}$$

$$\frac{\partial N_\theta}{\partial \theta} + R\frac{\partial N_{x\theta}}{\partial x} - \frac{\partial M_\theta}{R\partial \theta} + \frac{\partial M_{x\theta}}{\partial x} = 0 \tag{5-7}$$

$$\frac{\partial^2 M_{\theta x}}{\partial x \partial \theta} + R\frac{\partial^2 M_x}{\partial x^2} + \frac{\partial^2 M_\theta}{R\partial \theta^2} - \frac{\partial^2 M_{x\theta}}{\partial x \partial \theta} + N_\theta\left(1 + \frac{\partial v}{R\partial \theta} + \frac{\partial^2 w}{R\partial \theta^2}\right) + p_h R = R\rho h\frac{\partial^2 w}{\partial t^2} \tag{5-8}$$

where p_h is the external pressure acting on the tube, which is shown in Figure 5.2(a). ρ is the density of CNTs. According to theory [27], by substituting Eqs. (5-1)~(5-5) into Eqs. (5-6)~(5-8), we obtain

$$\frac{\partial^2 u}{\partial x^2} + \frac{(1-\upsilon)}{2R^2}\frac{\partial^2 u}{\partial \theta^2} + \frac{(1+\upsilon)}{2R}\frac{\partial^2 v}{\partial x \partial \theta} + p_h\phi\frac{\partial^2 v}{\partial x \partial \theta} - \frac{\upsilon}{R}\frac{\partial w}{\partial x} - p_h\phi\frac{\partial w}{\partial x} = 0 \tag{5-9}$$

$$\frac{(1+\upsilon)}{2R}\frac{\partial^2 u}{\partial x\partial\theta}+\frac{1}{R^2}\frac{\partial^2 v}{\partial\theta^2}+\frac{(1-\upsilon)}{2}\frac{\partial^2 v}{\partial x^2}+\frac{\beta}{R^2}\frac{\partial^2 v}{\partial\theta^2}+(1-\upsilon)\beta\frac{\partial^2 v}{\partial x^2}-\frac{1}{R^2}\frac{\partial w}{\partial\theta}$$
$$+\beta\frac{\partial^3 w}{\partial^2 x\partial\theta}+\frac{\beta}{R^2}\frac{\partial^3 w}{\partial\theta^3}=0 \tag{5-10}$$

$$\frac{\upsilon}{R}\frac{\partial u}{\partial x}+\frac{1}{R^2}\frac{\partial v}{\partial\theta}-(2-\upsilon)\beta\frac{\partial^3 v}{\partial x^2\partial\theta}-\frac{\beta}{R^2}\frac{\partial^3 v}{\partial\theta^3}-\frac{w}{R^2}-2\beta\frac{\partial^4 w}{\partial x^2\partial\theta^2}-R^2\beta\frac{\partial^4 w}{\partial x^4}$$
$$-\frac{\beta}{R^2}\frac{\partial^4 w}{\partial\theta^4}-\frac{p_h\phi}{R}w-\frac{p_h\phi}{R}\frac{\partial^2 w}{\partial\theta^2}-\rho h\phi\frac{\partial^2 w}{\partial t^2}=0 \tag{5-11}$$

where $\Phi = (1-\nu^2)/Eh$ and $\beta = h^2/12R^2$. To simplify the calculation, Eqs. (5-9)~(5-11) can be rewritten as

$$\begin{bmatrix} L_{11} & L_{12} & L_{13} \\ L_{21} & L_{22} & L_{23} \\ L_{31} & L_{32} & L_{33} \end{bmatrix}\begin{Bmatrix} u \\ v \\ w \end{Bmatrix}=0 \tag{5-12}$$

where L_{ij} are the differential operators given as

$$L_{11}=\frac{\partial^2}{\partial x^2}+\frac{(1-\upsilon)}{2R^2}\frac{\partial^2}{\partial\theta^2}$$
$$L_{12}=\frac{(1+\upsilon)}{2R}\frac{\partial^2}{\partial x\partial\theta}+p_h\phi\frac{\partial^2}{\partial x\partial\theta}$$
$$L_{13}=-\frac{\upsilon}{R}\frac{\partial}{\partial x}-p_h\phi\frac{\partial}{\partial x}$$
$$L_{21}=\frac{(1+\upsilon)}{2R}\frac{\partial^2}{\partial x\partial\theta}$$
$$L_{22}=\frac{1}{R^2}\frac{\partial^2}{\partial\theta^2}+\frac{(1-\upsilon)}{2}\frac{\partial^2}{\partial x^2}+\frac{\beta}{R^2}\frac{\partial^2}{\partial\theta^2}+(1-\upsilon)\beta\frac{\partial^2}{\partial x^2}$$
$$L_{23}=-\frac{1}{R^2}\frac{\partial}{\partial\theta}+\beta\frac{\partial^3}{\partial^2 x\partial\theta}+\frac{\beta}{R^2}\frac{\partial^3}{\partial\theta^3} \tag{5-13}$$
$$L_{31}=\frac{\upsilon}{R}\frac{\partial}{\partial x}$$
$$L_{32}=\frac{1}{R^2}\frac{\partial}{\partial\theta}-(2-\upsilon)\beta\frac{\partial^3}{\partial^2 x\partial\theta}-\frac{\beta}{R^2}\frac{\partial^3}{\partial\theta^3}$$
$$L_{33}=-\frac{1}{R^2}-2\beta\frac{\partial^4}{\partial x^2\partial\theta^2}-R^2\beta\frac{\partial^4}{\partial x^4}-\frac{\beta}{R^2}\frac{\partial^4}{\partial\theta^4}-\frac{p_h\phi}{R}-\frac{p_h\phi}{R}\frac{\partial^2}{\partial\theta^2}$$
$$-\rho h\phi\frac{\partial^2}{\partial t^2}$$

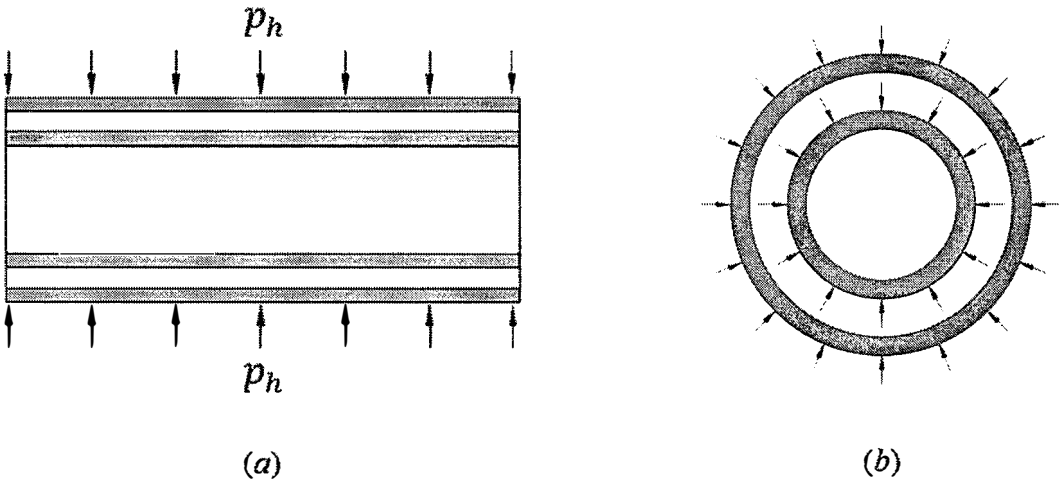

Figure 5.2 DWCNT model subjected to pressure for analysis

5.1.2.2 Van der Waals interaction forces

To study the vibrational behavior of DWCNTs, a double-elastic shell model was developed that assumes each of the nested tubes in a CNT is an individual elastic shell, and the adjacent tubes are coupled to each other by normal vdW interactions. The pressures from vdW forces exerted on the inner and outer nanotubes through vdW interaction forces (Figure 5.2 (b)) are given as

$$p_1 = c_{12}(\Delta w_2 - \Delta w_1) \tag{5-14}$$

$$p_2 = c_{21}(\Delta w_1 - \Delta w_2) + p_h \tag{5-15}$$

Δw_k (k=1, 2) are the radial displacements of the inner and outer nanotubes, and c_{ij} (i,j=1, 2) is the vdW interaction coefficient between nanotubes, which can be estimated from the Lennard-Jones potential [28]

$$c_{ij} = \frac{\pi\varepsilon R_j \sigma^6}{3a^4}\left[\frac{1120}{3}H_{ij}^7 - 1001\sigma^6 H_{ij}^{13}\right] \tag{5-16}$$

where

$$H_{ij}^{m} = \left(R_i + R_j\right)^{-m} \int_0^{\frac{\pi}{2}} \frac{d\theta}{\left(1 - K_{ij}\cos^2\theta\right)^{\frac{m}{2}}} \qquad (m = 7,13) \tag{5-17}$$

and

$$K_{ij} = \frac{4R_iR_j}{\left(R_i + R_j\right)^2} \tag{5-18}$$

where a is the carbon-carbon bond length (0.142 nm), R_i and R_j are the inner and outer radii of the DWCNTs, and σ and ε are the vdW radius and the well depth of the Lennard-Jones potential, respectively. The vdW parameters in the Lennard-Jones potential are ε = 2.967 meV and σ = 0.34 nm as reported by Saito *et al.* [29].

Under pressure, the radial displacements of DWCNTs Δw_k (k=1, 2) in Eqs. (5-14)~(5-15) are the function of the pressure exerted on the inner and outer tubes, given as

$$\Delta w_k = \frac{p_k R_k^2}{Eh}\left(1 - \frac{\upsilon_k}{2}\right) \qquad (k = 1,2) \tag{5-19}$$

where υ_k and R_k (k=1, 2) are Poisson's ratio and the radii of the inner and outer tubes, respectively.

Substituting Eq. (5-19) into Eqs. (5-14)~(5-15) yields

$$p_1 = \frac{p_h}{\Delta}\frac{c_{12}R_2^2}{Eh}\left(1 - \frac{\upsilon_2}{2}\right) \tag{5-20}$$

$$p_2 = \frac{p_h}{\Delta}\left[1 + \frac{c_{12}R_1^2}{Eh}\left(1 - \frac{\upsilon_1}{2}\right)\right] \tag{5-21}$$

where

$$\Delta = 1 + \frac{c_{12}R_1^2}{Eh}\left(1 - \frac{\upsilon_1}{2}\right) + \frac{c_{21}R_2^2}{Eh}\left(1 - \frac{\upsilon_2}{2}\right) \tag{5-22}$$

5.1.2.3 RBM frequency of CNTs

The general solution for the displacements u, v and w in the inner and outer tubes of a DWCNT can be given by

$$u = A_k \sin(n\theta)\cos\frac{m\pi x}{l} e^{i\omega t} \tag{5-23}$$

$$v = B_k \cos(n\theta)\sin\frac{m\pi x}{l} e^{i\omega t} \tag{5-24}$$

$$w = C_k \sin(n\theta)\sin\frac{m\pi x}{l} e^{i\omega t} \qquad (k = 1,2) \tag{5-25}$$

where A_k, B_k and C_k are the longitudinal, circumferential and radial amplitudes of displacement in the inner tube (k=1) and the outer tube (k=2), respectively. ω is the circular frequency of RBM and t is time. The wave numbers m and n are the axial half-wave and circumferential numbers, respectively.

5.1.3 Numerical results and discussion

The influence of different nanotube parameters on the frequency of the RBM was investigated using the proposed method. An individual SWCNT is regarded to have the thickness of a graphene sheet, 0.34 nm. In the calculations, the elastic modulus of a CNT is 3.3 TPa, Poisson's ratio is 0.27, and the mass density of CNTs is 2.3 g/cm^3. DWCNTs were assumed to have an inner diameter of 2.2 nm and an outer diameter of 3.0 nm [30].

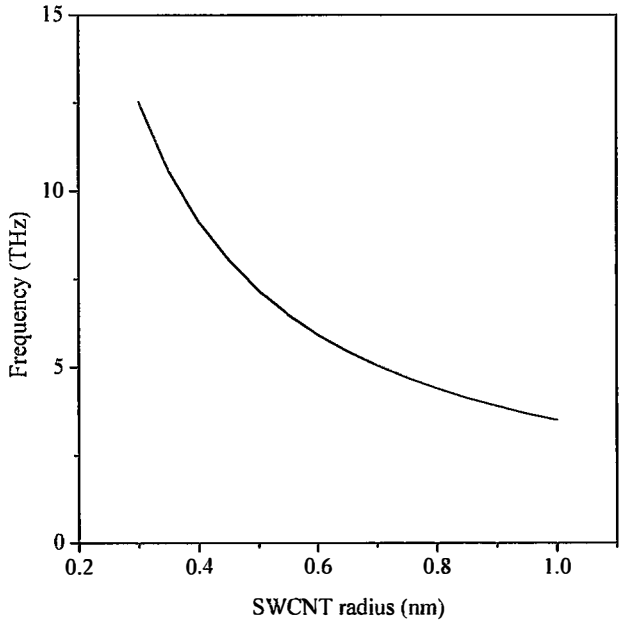

Figure 5.3 Frequency of the RBM of SWCNTs not subjected to pressure as a function of radius

Using the present theoretical approach, the frequency of the RBM of isolated SWCNTs under no pressure as a function of radius was calculated and is shown in Figure 5.3. The frequency of the RBM decreases significantly as the radius of the SWCNT increased from 0.3 to 1.0 nm. Note that the commonly used unit for the frequency of the RBM f is in cm^{-1} for Raman spectroscopy experiments; the unit of Hertz (Hz) for ω has been adopted for convenience in this study. The relation between these terms is $\omega = c \times f$, where $c = 3.0 \times 10^8$ m/s and is the velocity of light in a vacuum. Some studies have used other approaches to research the frequency of the RBM of isolated SWCNTs. Kurti *et al.* [22] used first-principles calculations to show that the frequency of the RBM was 9.87—4.50 THz for SWCNTs with radii of 0.35—0.78 nm. Jorio *et al.* [31] calculated that the frequency of the RBM ranged from 5.28 to 4.32 THz for SWCNTs with radii of 0.715 to 0.86 nm considering structural determination. Finite element methods [6] have also been used to investigate the RBM of CNTs and Dresselhaus *et al.* [32] published a review on the frequency of the RBM of isolated

SWCNTs. The calculated frequencies of the RBM of SWCNTs with varying radius under no pressure agree closely with the values reported in the literatures, which verifies that the continuum elastic shell model accurately describes the frequency of the RBM of CNTs.

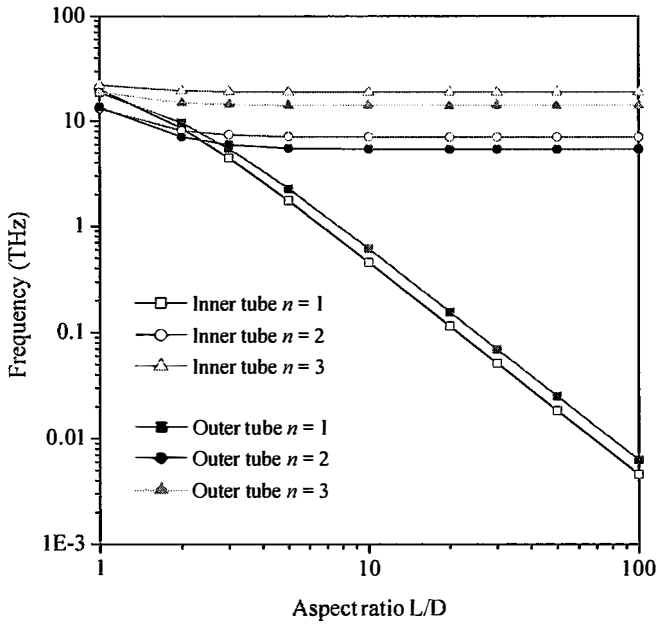

Figure 5.4 Comparison of the frequencies of the RBM of inner and outer tubes in DWCNTs subjected pressure with different circumference wave numbers as a function of aspect ratio (m = 1)

The frequencies of the RBM of the inner tube and outer tube of a DWCNT as a function of aspect ratio L/D are compared in Figure 5.4. The changes in frequency for both inner and outer tubes show a sublinear logarithmic relationship with increasing aspect ratio. The frequencies of the RBM of the inner and outer tubes exhibit a concentrated distribution in the same region. Each tube exhibits the vibration frequency of CNTs over one terahertz, and the frequency of the inner tube is a little higher than that of the outer tube, except for a circumferential wave of n = 1. The lowest frequency of DWCNTs is characterized by the circumferential wave n = 1, and exists in the DWCNTs with larger aspect ratio. Meanwhile, the frequency of the RBM decreases

dramatically with increasing aspect ratio. When the circumferential wave n = 1, the cross sections of DWCNTs present away from the axial central axis, which makes the whole tubes to be unstable status. This phenomena is unique to DWCNTs with circumferential wave n = 1, and is not observed in other circumferential waves. The unsteady DWCNTs with circumferential wave n = 1 can be influenced by external factors more easily than with other circumferential waves. The frequency of the RBM of DWCNTs with an aspect ratio of L/D < 2 decreases slightly with increasing aspect ratio. At aspect ratios of L/D > 2, the frequency is almost independent of the aspect ratio when the circumferential wave n is 2 or greater.

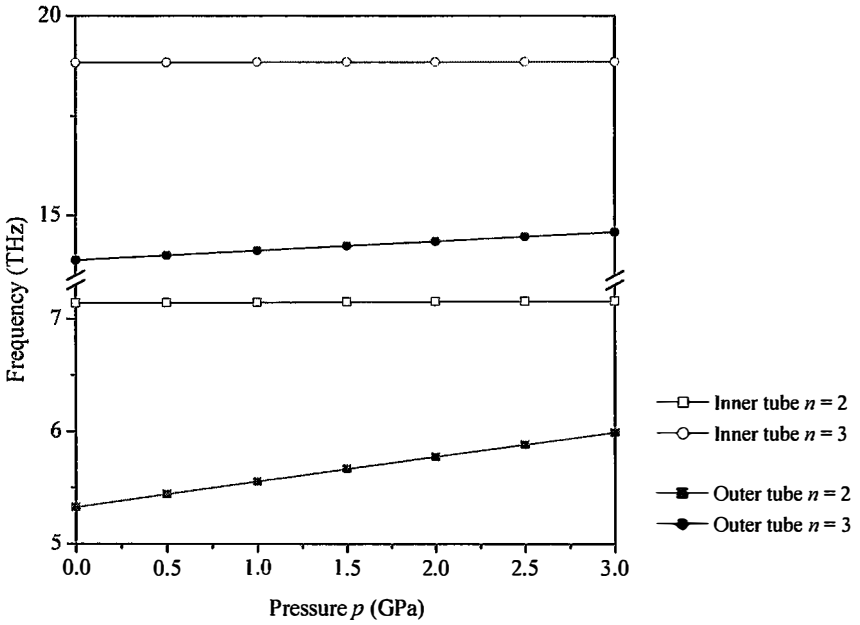

Figure 5.5 Comparison of the frequencies of the RBM between inner and outer tubes in DWCNTs with different circumference wave numbers as a function of pressure (m = 4, L/D = 20)

The frequencies of the RBM of DWCNTs with different circumferential wave numbers (n = 2, 3), axial half-wave numbers (m = 1, 3, 5) and aspect ratios (L/D = 5, 10, 20) subjected to pressure were investigated and the results are shown in Figures. 5.5—5.7. The circumference wave number n plays a critical role as the pressure

increases, while the frequency of the RBM is hardly affected by the axial half-wave number or the aspect ratio. The frequency of the RBM has a positive linear relationship with increasing pressure in these figures, and this increase is more significant for the outer tube than the inner tube. Figure 5.5 shows the frequencies of the RBM of inner and outer tubes with circumference numbers of $n = 2$ and $n = 3$ ($m = 4$, L/D = 20) with increasing pressure. The gradients for frequency/pressure of the inner tube with $n = 2$ and $n = 3$ are 6.5 and 6.6 GHz/GPa, respectively, and 200.2 and 223.8 GHz/GPa for the outer tube, respectively. Frequencies of the RBM of the inner and outer tube with axial half-waves of $m = 1$, $m = 3$ and $m = 5$ ($n = 2$, L/D = 20) with increasing pressure are shown in Figure 5.6. The gradients of the inner tube with $m = 1$, $m = 3$ and $m = 5$ are 6.6, 6.5 and 6.4 GHz/GPa, respectively, and 204.9, 202.7 and 196.7 GHz/GPa for the outer tube, respectively. Figure 5.7 shows the frequencies of the RBM of inner and outer tubes with aspect ratios of L/D = 5, 10 and 20 ($m = 1$, $n = 2$) with increasing pressure. The gradients of the inner tube with L/D = 5, 10 and 20 are 6.5, 6.6 and 6.6 GHz/GPa, respectively, and 200.3, 204.2 and 204.9 GHz/GPa for the outer tube, respectively.

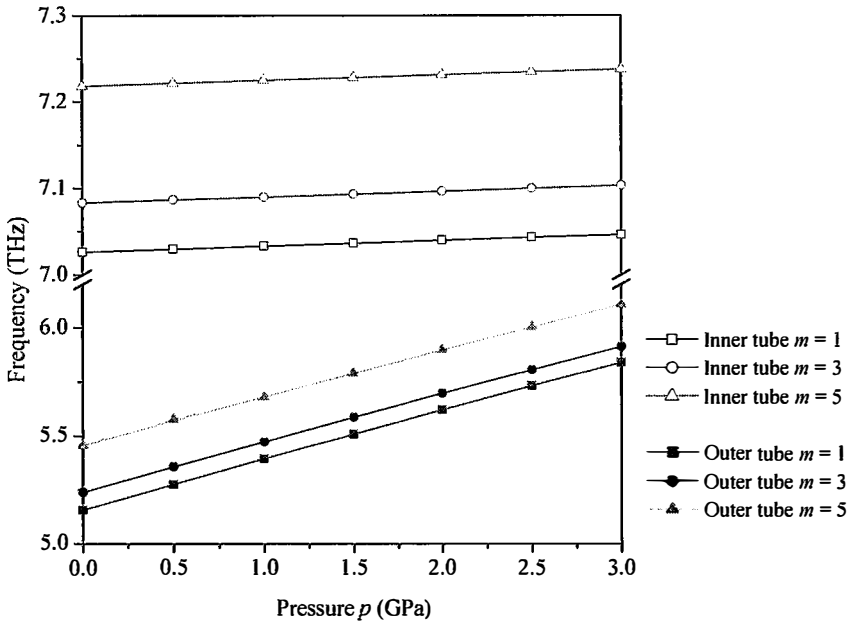

Figure 5.6 Comparison of the frequencies of the RBM between inner and outer tubes in DWCNTs with different axial half-wave numbers as a function of pressure (n = 2, L/D = 20)

Therefore, according to the variation in the curves of the frequencies of the RBM frequencies of inner and outer tubes are almost parallel lines, and the range of variation in the RBM frequency of inner tube is smaller than that of outer tube. Considering unbundled DWCNTs, the trends and range of frequencies of the RBM for both the inner and outer tubes with increasing pressure agree closely with the experimental results of Arvanitidis and Christofilos [8], who revealed that the frequency of the RBM of the external tubes increased linearly with increasing pressure. Therefore, the theoretical results calculated in this study are consistent with experimental results. Moreover, due to vdW interaction forces and external pressure, the inner tube owns smaller variation of the RBM frequency than the outer tube. The inner tube is only reinforced by vdW interaction forces, and is slightly influenced by the external pressure, so the vdW interaction forces make a governing and positive role in the RBM frequency of the inner tube. Comparing with the inner tube, the outer tube suffers not

only with vdW interaction forces, but also with external pressure which neutralizes the positive vdW interaction forces and makes a negative role at the same time. With the growing external pressure, the governing role of vdW interaction forces become less and less, which leads that the RBM frequency of the outer tube is more sensitive to the external pressure and has a bigger variation of the RBM frequency than that of the inner tube.

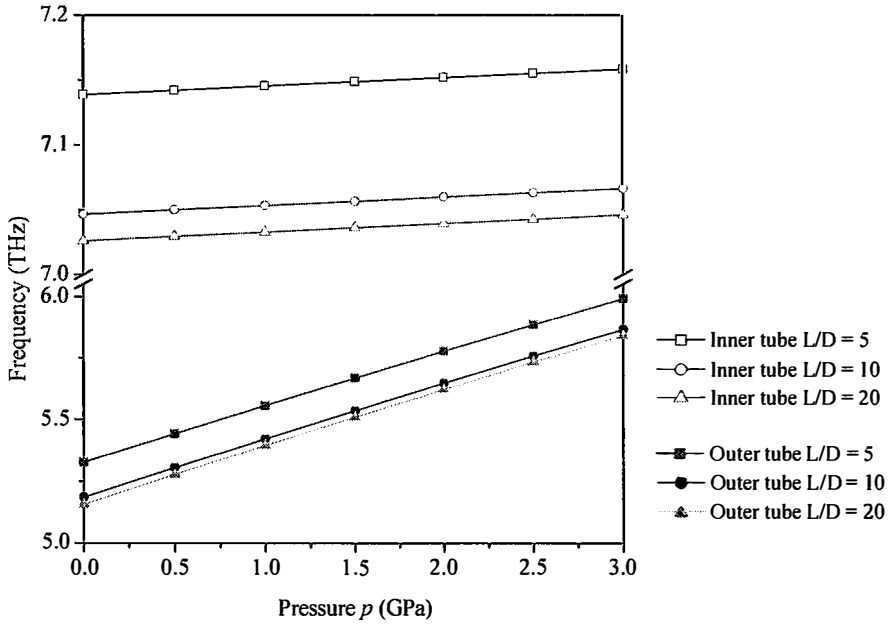

Figure 5.7 Comparison of the frequencies of the RBM between inner and outer tubes in DWCNTs with different aspect ratios as a function of pressure ($m = 1, n = 2$)

5.1.4 Conclusions

The RBM of DWCNTs subjected to pressures were investigated using an elastic continuum shell model. In the analysis, each tube of a DWCNT was described as an individual elastic shell and DWCNTs were considered to be two-layered nanotube shells coupled by vdW interactions. The axial half-wave number and the aspect ratio had little effect on the frequency of the RBM. In contrast, the circumference wave number affected the frequency of the RBM significantly. Compared with previous experimental and simulation investigations on the frequency of the RBM of isolated

SWCNTs with increasing radius and DWCNTs with increasing pressure, the continuum shell model can be used to reasonably predict the frequency of the RBM of CNTs subjected to pressure. According to the variation of the frequency of the RBM of DWCNTs with increasing pressure, the inner tube is affected less than the outer tube. Based on this model and a theoretical approach, a numerical simulation investigating the RBM of multiwalled CNTs subjected to pressure can be developed. Theoretical analysis of the RBM of DWCNTs is useful for nanofabrication and nanodevice technologies.

5.2 Carbon nanotubes subjected to axial pressure

5.2.1 Introduction

For CNTs, pressure studies are motivated by the need to investigate mechanical stability, pressure–induced phase transitions (such as vibrational characteristics), and the effects of intertube interactions. In this section, the RBM frequency of CNTs subjected to axial pressure is studied using an elastic continuum mechanics model. Single-walled carbon nanotubes (SWCNTs) are described as an individual elastic shell and double-walled carbon nanotubes (DWCNTs) are considered as two shells coupled through the van der Waals (vdW) force interaction between them. The interaction of the vdW force between the inner and outer tubes and the effect of axial pressure are incorporated into the formulation. We consider the effects of the influences of the axial half-wave number m, circumference wave number n, nanotube diameter, and the aspect ratio L/D of the nanotubes on the RBM frequency for SWCNTs and DWCNTs exposed to varying axial pressures. Through comparison with previous results obtained from experiments and simulations, it can be seen that the continuum shell model can be used to predict the RBM frequency of CNTs exposed to various axial pressures.

5.2.2 Theoretical approach

5.2.2.1 Governing equations of SWCNTs under axial pressure

Based on shell theory mentioned above, the equation of motion for simple supported CNTs is given by:

$$R\frac{\partial^2 u}{\partial x^2}+\frac{(1-\upsilon)}{2R}\frac{\partial^2 u}{\partial \theta^2}+\frac{(1+\upsilon)}{2}\frac{\partial^2 v}{\partial x\partial\theta}-\upsilon\frac{\partial w}{\partial x}=0 \tag{5-26}$$

$$\frac{(1+\upsilon)}{2R}\frac{\partial^2 u}{\partial x\partial\theta}+\frac{1}{R^2}\frac{\partial^2 v}{\partial\theta^2}+\frac{(1-\upsilon)}{2}\frac{\partial^2 v}{\partial x^2}+\phi h p_x\frac{\partial^2 v}{\partial x^2}+(1-\upsilon)\beta\frac{\partial^2 v}{\partial x^2}+\frac{\beta}{R^2}\frac{\partial^2 v}{\partial\theta^2}$$
$$-\frac{1}{R^2}\frac{\partial w}{\partial\theta}+\beta\frac{\partial^3 w}{\partial^2 x\partial\theta}+\frac{\beta}{R^2}\frac{\partial^3 w}{\partial\theta^3}=0 \tag{5-27}$$

$$\frac{\upsilon}{R}\frac{\partial u}{\partial x}+\frac{1}{R^2}\frac{\partial v}{\partial\theta}-(2-\upsilon)\beta\frac{\partial^3 v}{\partial x^2\partial\theta}-\frac{\beta}{R^2}\frac{\partial^3 v}{\partial\theta^3}+\phi h p_x\frac{\partial^2 v}{\partial x^2}-\frac{w}{R^2}-2\beta\frac{\partial^4 w}{\partial x^2\partial\theta^2}$$
$$-R^2\beta\frac{\partial^4 w}{\partial x^4}-\frac{\beta}{R^2}\frac{\partial^4 w}{\partial\theta^4}-\rho h\phi\frac{\partial^2 w}{\partial t^2}+2\phi p=0 \tag{5-28}$$

where $\Phi = (1-\nu^2)/Eh$ and $\beta = h^2/12R^2$; p_x is the axial pressure acting on the both ends of the CNT; and p is the vdW interaction pressure between inner tube and outer tube in a DWCNT, which is shown schematically in Figure 5.8.

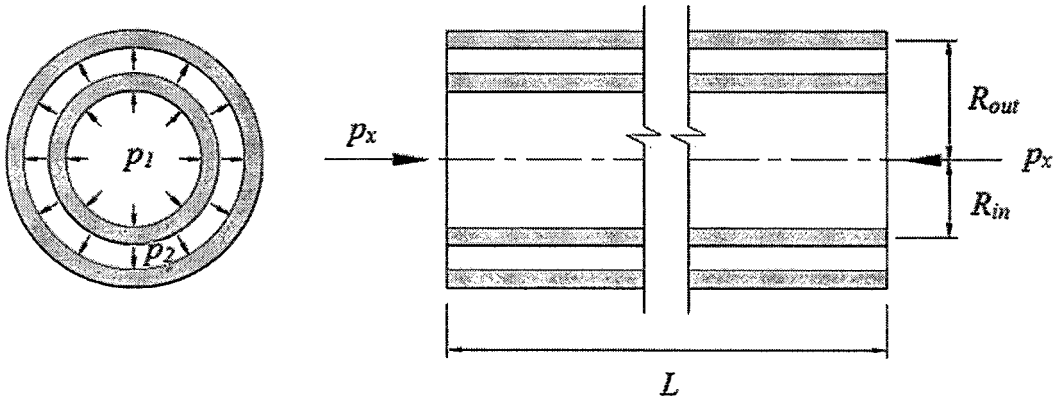

Figure 5.8 Schematic of the DWCNT model subjected to axial pressure for analysis. The left image displays the latitudinal cross-section, which shows the vdW

force between the inner and outer tubes. The right image displays the longitudinal cross-section, which shows the axial pressure acting on both ends of the DWCNT.

5.2.2.2 Van der Waals interaction forces

To study the vibrational behavior of DWCNTs, a double-elastic shell model was developed that assumes each of the nested tubes in a CNT is an individual elastic shell, and the adjacent tubes are coupled to each other by normal vdW interactions. The pressures exerted on the inner and outer nanotubes through the vdW interaction forces (Figure 5.8) are given as

$$p_1 = c_{12}(w_2 - w_1) \tag{5-29}$$

$$p_2 = c_{21}(w_1 - w_2) \tag{5-30}$$

w_k (k = 1, 2) are the radial displacements of the inner and outer nanotubes, and c_{ij} (i,j=1, 2) is the vdW interaction coefficient between nanotubes, which has been mentioned in Eqs. (5-16)~(5-18)

5.2.2.3 RBM frequency of DWCNTs

To model the vdW force, we substitute Eqs. (5-29) and (5-30) into Eqs. (5-26)~(5-29). The governing equations for the RBM frequency of inner and outer tubes of DWCNTs subjected to an axial pressure can be expressed as:

For inner tube

$$r\frac{\partial^2 u_1}{\partial x^2} + \frac{(1-\upsilon)}{2r}\frac{\partial^2 u_1}{\partial \theta^2} + \frac{(1+\upsilon)}{2}\frac{\partial^2 v_1}{\partial x \partial \theta} - \upsilon\frac{\partial w_1}{\partial x} = 0 \tag{5-31}$$

$$\begin{aligned}&\frac{(1+\upsilon)}{2r}\frac{\partial^2 u_1}{\partial x \partial \theta} + \frac{1}{r^2}\frac{\partial^2 v_1}{\partial \theta^2} + \frac{(1-\upsilon)}{2}\frac{\partial^2 v_1}{\partial x^2} + \phi h p_x \frac{\partial^2 v_1}{\partial x^2} + (1-\upsilon)\beta\frac{\partial^2 v_1}{\partial x^2} + \frac{\beta}{r^2}\frac{\partial^2 v_1}{\partial \theta^2} \\ &-\frac{1}{r^2}\frac{\partial w_1}{\partial \theta} + \beta\frac{\partial^3 w_1}{\partial^2 x \partial \theta} + \frac{\beta}{r^2}\frac{\partial^3 w_1}{\partial \theta^3} = 0\end{aligned} \tag{5-32}$$

$$\frac{\upsilon}{r}\frac{\partial u_1}{\partial x}+\frac{1}{r^2}\frac{\partial v_1}{\partial \theta}-(2-\upsilon)\beta\frac{\partial^3 v_1}{\partial x^2\partial\theta}-\frac{\beta}{r^2}\frac{\partial^3 v_1}{\partial\theta^3}+\phi hp_x\frac{\partial^2 v_1}{\partial x^2}-\frac{w_1}{r^2}-2\beta\frac{\partial^4 w_1}{\partial x^2\partial\theta^2}$$
$$-r^2\beta\frac{\partial^4 w_1}{\partial x^4}-\frac{\beta}{r^2}\frac{\partial^4 w_1}{\partial\theta^4}-\rho h\phi\frac{\partial^2 w_1}{\partial t^2}-2\phi c_{12}w_1+2\phi c_{12}w_2=0 \tag{5-33}$$

For outer tube

$$R\frac{\partial^2 u_2}{\partial x^2}+\frac{(1-\upsilon)}{2R}\frac{\partial^2 u_2}{\partial\theta^2}+\frac{(1+\upsilon)}{2}\frac{\partial^2 v_2}{\partial x\partial\theta}-\upsilon\frac{\partial w_2}{\partial x}=0 \tag{5-34}$$

$$\frac{(1+\upsilon)}{2R}\frac{\partial^2 u_2}{\partial x\partial\theta}+\frac{1}{R^2}\frac{\partial^2 v_2}{\partial\theta^2}+\frac{(1-\upsilon)}{2}\frac{\partial^2 v_2}{\partial x^2}+\phi hp_x\frac{\partial^2 v_2}{\partial x^2}+(1-\upsilon)\beta\frac{\partial^2 v_2}{\partial x^2}+\frac{\beta}{R^2}\frac{\partial^2 v_2}{\partial\theta^2}$$
$$-\frac{1}{R^2}\frac{\partial w_2}{\partial\theta}+\beta\frac{\partial^3 w_2}{\partial^2 x\partial\theta}+\frac{\beta}{R^2}\frac{\partial^3 w_2}{\partial\theta^3}=0 \tag{5-35}$$

$$2\phi c_{12}w_1+\frac{\upsilon}{R}\frac{\partial u_2}{\partial x}+\frac{1}{R^2}\frac{\partial v_2}{\partial\theta}-(2-\upsilon)\beta\frac{\partial^3 v_2}{\partial x^2\partial\theta}-\frac{\beta}{R^2}\frac{\partial^3 v_2}{\partial\theta^3}+\phi hp_x\frac{\partial^2 w_2}{\partial x^2}-\frac{w_2}{R^2}$$
$$-2\beta\frac{\partial^4 w_2}{\partial x^2\partial\theta^2}-R^2\beta\frac{\partial^4 w_2}{\partial x^4}-\frac{\beta}{R^2}\frac{\partial^4 w_2}{\partial\theta^4}-\rho h\phi\frac{\partial^2 w_2}{\partial t^2}-2\phi c_{12}w_2=0 \tag{5-36}$$

where r and R are the radius of inner tube and outer tube of the DWCNT, respectively.

To simplify the calculation, Eqs. (5-31)~(5-36) can be rewritten as

$$\begin{bmatrix} L_{11} & L_{12} & L_{13} & L_{14} & L_{15} & L_{16} \\ L_{21} & L_{22} & L_{23} & L_{24} & L_{25} & L_{26} \\ L_{31} & L_{32} & L_{33} & L_{34} & L_{35} & L_{36} \\ L_{41} & L_{42} & L_{43} & L_{44} & L_{45} & L_{46} \\ L_{51} & L_{52} & L_{53} & L_{54} & L_{55} & L_{56} \\ L_{61} & L_{62} & L_{63} & L_{64} & L_{65} & L_{66} \end{bmatrix}\begin{Bmatrix} u_1 \\ v_1 \\ w_1 \\ u_2 \\ v_2 \\ w_2 \end{Bmatrix}=0 \tag{5-37}$$

where L_{ij} are the differential operators given as:

$$L_{11}=r\frac{\partial^2}{\partial x^2}+\frac{(1-\upsilon)}{2r}\frac{\partial^2}{\partial\theta^2}$$
$$L_{12}=\frac{(1+\upsilon)}{2}\frac{\partial^2}{\partial x\partial\theta}$$
$$L_{13}=-\upsilon\frac{\partial}{\partial x}$$
$$L_{21}=\frac{(1+\upsilon)}{2r}\frac{\partial^2}{\partial x\partial\theta}$$
$$L_{22}=\frac{1}{r^2}\frac{\partial^2}{\partial\theta^2}+\frac{(1-\upsilon)}{2}\frac{\partial^2}{\partial x^2}+\phi hp_x\frac{\partial^2}{\partial x^2}+\frac{\beta}{r^2}\frac{\partial^2}{\partial\theta^2}+(1-\upsilon)\beta\frac{\partial^2}{\partial x^2} \tag{5-38}$$

$$L_{23} = -\frac{1}{r^2}\frac{\partial}{\partial\theta} + \beta\frac{\partial^3}{\partial^2 x\partial\theta} + \frac{\beta}{r^2}\frac{\partial^3}{\partial\theta^3}$$

$$L_{31} = \frac{\upsilon}{r}\frac{\partial}{\partial x}$$

$$L_{32} = \frac{1}{r^2}\frac{\partial}{\partial\theta} - (2-\upsilon)\beta\frac{\partial^3}{\partial^2 x\partial\theta} - \frac{\beta}{r^2}\frac{\partial^3}{\partial\theta^3}$$

$$L_{33} = \phi hp_x\frac{\partial^2}{\partial x^2} - \frac{1}{r^2} - 2\beta\frac{\partial^4}{\partial x^2\partial\theta^2} - r^2\beta\frac{\partial^4}{\partial x^4} - \frac{\beta}{r^2}\frac{\partial^4}{\partial\theta^4} - \rho h\phi\frac{\partial^2}{\partial t^2}$$
$$-2\phi c_{12}$$

$$L_{36} = 2\phi c_{12}$$

$$L_{44} = R\frac{\partial^2}{\partial x^2} + \frac{(1-\upsilon)}{2R}\frac{\partial^2}{\partial\theta^2}$$

$$L_{45} = \frac{(1+\upsilon)}{2}\frac{\partial^2}{\partial x\partial\theta}$$

$$L_{46} = -\upsilon\frac{\partial}{\partial x}$$

$$L_{54} = \frac{(1+\upsilon)}{2R}\frac{\partial^2}{\partial x\partial\theta}$$

$$L_{55} = \frac{1}{R^2}\frac{\partial^2}{\partial\theta^2} + \frac{(1-\upsilon)}{2}\frac{\partial^2}{\partial x^2} + \phi hp_x\frac{\partial^2}{\partial x^2} + \frac{\beta}{R^2}\frac{\partial^2}{\partial\theta^2} + (1-\upsilon)\beta\frac{\partial^2}{\partial x^2}$$

$$L_{56} = -\frac{1}{R^2}\frac{\partial}{\partial\theta} + \beta\frac{\partial^3}{\partial^2 x\partial\theta} + \frac{\beta}{R^2}\frac{\partial^3}{\partial\theta^3}$$

$$L_{63} = 2\phi c_{21}$$

$$L_{64} = \frac{\upsilon}{R}\frac{\partial}{\partial x}$$

$$L_{65} = \frac{1}{R^2}\frac{\partial}{\partial\theta} - (2-\upsilon)\beta\frac{\partial^3}{\partial^2 x\partial\theta} - \frac{\beta}{R^2}\frac{\partial^3}{\partial\theta^3}$$

$$L_{66} = \phi hp_x\frac{\partial^2}{\partial x^2} - \frac{1}{R^2} - 2\beta\frac{\partial^4}{\partial x^2\partial\theta^2} - R^2\beta\frac{\partial^4}{\partial x^4} - \frac{\beta}{R^2}\frac{\partial^4}{\partial\theta^4} - \rho h\phi\frac{\partial^2}{\partial t^2}$$
$$-2\phi c_{21}$$

$$L_{14} = L_{15} = L_{16} = L_{24} = L_{25} = L_{26} = L_{34} = L_{35} = L_{41} = L_{42} = L_{43} = L_{51}$$
$$= L_{52} = L_{53} = L_{61} = L_{62} = 0$$

The general solution for the displacements u_k, v_k and w_k in the inner and outer tubes of a DWCNT can be given by

$$u = A_k \sin(n\theta)\cos\frac{m\pi x}{l} e^{i\omega t} \tag{5-39}$$

$$v = B_k \cos(n\theta)\sin\frac{m\pi x}{l} e^{i\omega t} \tag{5-40}$$

$$w = C_k \sin(n\theta)\sin\frac{m\pi x}{l} e^{i\omega t} \qquad (k = 1,2) \tag{5-41}$$

where A_k, B_k and C_k are the longitudinal, circumferential and radial amplitudes of the displacements in the inner (k = 1) and outer tubes (k = 2), respectively. L is the length of CNT which is shown in Figure 5.1. The wave numbers m and n are the axial half-wave and circumferential numbers, respectively.

5.2.3 Numerical results and discussion

For the present analysis, an individual SWCNT was assumed to be a graphene sheet rolled into a cylinder and the DWCNT is considered to be two layered nanotube shells coupled by vdW interactions. The value of the thickness of sheet is 0.34 nm; the elastic modulus is 1.0 TPa; the Poisson's ratio is 0.27; the mass density of the CNTs is 2.3 g/cm^3; and the inner and outer diameters of the DWCNTs are 2.2 nm and 3.0 nm, respectively [30].

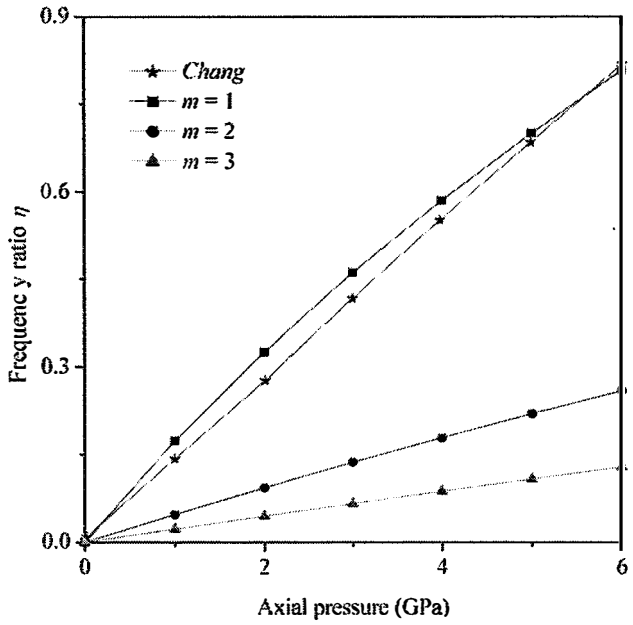

Figure 5.9 RBM frequency ratios for SWCNTs with axial half-wave numbers (m) varying from 1 to 4. The results from the nonlinear stick-spiral model by Chang *et al.* [33] are also presented for comparison.

Based on our proposed theoretical approach, we first calculate the RBM frequency of an isolated SWCNT subjected to zero pressure varying with radius. The RBM frequency ratios of SWCNTs with different axial half-wave numbers subjected to axial pressure in shown in Figure 5.9. The frequency ratio η is defined as:

$$\eta = \frac{f_p - f_0}{f_0} \tag{5-42}$$

where f_p is the frequency of the RBM with exposed to axial pressure, and f_0 is the frequency of RBM not exposed to axial pressure. Note that the RBM frequency ratio η is sublinear with respect to increasing axial pressure. We also found that the axial half-wave number m plays a critical role in this increasing frequency ratio. When the axial half-wave number increases, the increment of change in the speed of the frequency ratio becomes much smaller. The results from nonlinear stick-spiral model, presented by Chang *et al.* [33], are also shown for comparison. The models show good agreement

when the axial half-wave number m is 1. These results confirm that the largest contribution to the RBM for a SWCNT comes when $m = 1$. By contrast, $m \geq 2$ wave numbers are in the minority.

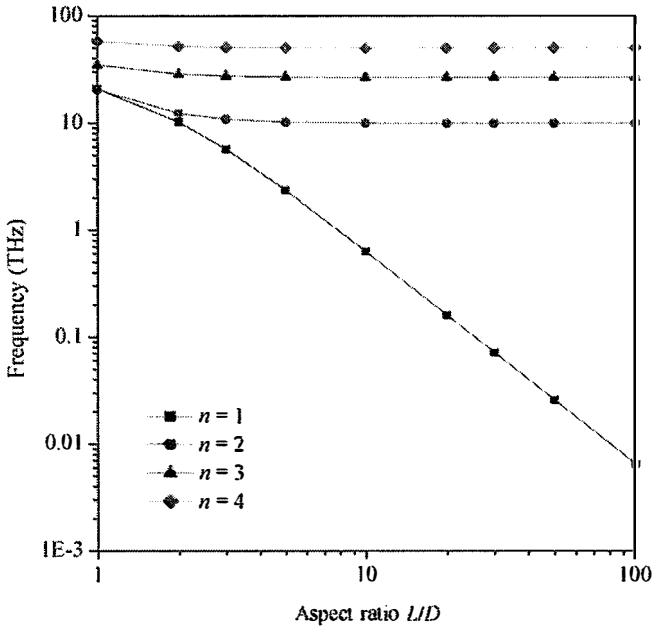

Figure 5.10 RBM frequencies of the SWCNTs as a function of aspect ratio. The SWCNTs have the same axial half-wave numbers, $m = 1$; and axial pressures, $p_x = 1$ TPa. However, they have circumference wave numbers n that vary from 1 to 4.

Figure 5.10 shows the RBM frequencies of SWCNTs as a function of the aspect ratio L/D (D is the diameter of the SWCNT). The frequencies of the SWCNTs grow sublinear logarithmically with an increasing aspect ratio. When the circumferential wave n is 1, the frequency of the RBM decreases dramatically with increasing aspect ratio. This is especially true for larger aspect ratios, and the variational trend of the RBM frequency is quite different for $n = 2$, 3, 4 or higher. This is caused by the misalignment of the tubes for the circumferential wave $n = 1$, which makes the entire SWCNTs unstable. The unstable SWCNTs with $n = 1$ can be affected by external factors more easily than those with other circumferential waves numbers. This

phenomena is unique to SWCNTs with n = 1, and cannot be observed with other circumferential waves numbers. However, the RBM frequency is largely unaffected by the aspect ratio of the tube when $n \geq 2$.

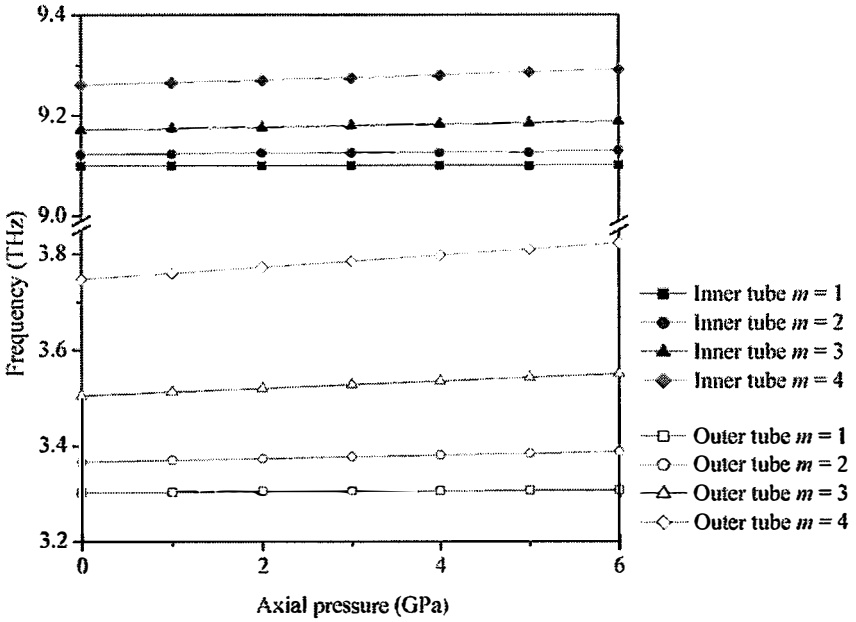

Figure 5.11 RBM frequencies of DWCNTs as a function of axial pressure with axial half-wave numbers (m) that vary from 1 to 4.

In the following, an analysis of the RBM frequency of inner and outer tubes in DWCNTs subject to axial pressure is carried out. Figure 5.11 shows the RBM frequencies of DWCNTs with different axial half-wave numbers of m = 1–4 as a function of increasing axial pressure for inner and outer tubes. The wave number in the axial direction plays an important role in determining the RBM frequency of DWCNTs. Thus, the larger mode numbers result in higher RBM frequencies with increasing axial pressure. The RBM frequencies of both inner and outer tubes have positive linear relationships with pressure acting on both ends of DWCNTs. Compared with RBM frequencies of inner tubes, the frequencies of outer tubes are more sensitive to the varying wave numbers and axial pressure shown in Figure 5.11. The frequencies of

inner and outer tubes vary over different ranges when the DWCNTs are subjected to the same axial pressures. For a given interval of axial pressure, the RBM frequency of outer tubes is a little higher than that of inner tubes. The reason is that the RBM frequency with smaller radius CNT is much less than that of longer radius CNT, which has been mentioned in the beginning.

5.2.4 Conclusions

Based on elastic continuum mechanics, we studied the RBM frequency of simply-supported CNTs exposed to axial pressure. The SWCNTs were modeled as individual elastic shells, and the DWCNTs were considered to be two layered nanotube shells coupled by vdW interactions. The effects of the wave numbers, aspect ratio and axial pressure are discussed in detail. It can be seen through comparison with previous experimental and simulation investigations on the RBM frequency of isolated SWCNTs with increasing radius and the RBM frequency ratio with increasing pressure, the continuum shell model can be used to predict the RBM frequency of CNTs subject to an axial pressure. The results of the CNTs exposed to an axial pressure show that the RBM vibration frequency is sensitive to both the vibrational mode and axial pressure, while the frequency of the RBM is hardly affected by the aspect ratio. We are now processing the theoretical analysis on vibrational properties of SWCNTs and DWCNTs subjected to axial pressure in order to provide further quantitative and qualitative experiments and simulations on RBM of CNTs.

References

[1] C. Q. Ru, "Elastic Models for Carbon Nanotubes," in *Encyclopedia of Nanoscience and Nanotechnology*, (edited by H. S. Nalwa) (American Scientific, Publishers) **2**, 731 (2004)

[2] M. S. Dresselhausa, G. Dresselhausb, R. Saitoc, A. Joriod, Phys. Rep. **409**, 47 (2005)

[3] S. Costa, E. Borowiak-Palen, M. Kruszyñska, A. Bachmatiuk, R. J. Kaleńczuk, Mater. Sci. Poland **26**, 433 (2008)

[4] R. C. Batra, S. S. Gupta, J. Appl. Mech. **75**, 061010 (2008)

[5] S. Costa, E. Borowiak-Palen, M. Kruszyñska, A. Bachmatiuk, R J. Kaleńczuk, Mater. Sci. Poland **26**, 433 (2008).

[6] H.C. Cheng, Y.L. Liu, C.H. Wu, W.H. Chen, Comput. Methods Appl. M. **199**, 2820 (2010)

[7] I. Loa, J. Raman Spectrosc. **34**, 611 (2003)

[8] J. Arvanitidis, D. Christofilos, Phys. Stat. Sol. (*b*) **244**, 127 (2007)

[9] U. Schlecht, U. D. Venkateswaran, E. Richter, J. Chen, R. C. Haddon, P. C. Eklund, A. M. Rao, J. Nanosci. Nanotech. **3**, 139 (2003)

[10] U. D. Venkateswaran, A. M. Rao, E. Richter M. Menon, A. Rinzler, R. E. Smalley, P. C. Eklund, Phys. Rev. B 59, 10928 (1999)

[11] U. D. Venkateswaran, E. A. Brandsen, U. Schlecht, A. M. Rao, E. Richter, I. Lo, K. Syassen, P. C. Eklund, Phys. Stat. Sol. (*b*) **223**, 225 (2001)

[12] S. Lebedkin, K. Arnold, O. Kiowski, F. Hennrich, M. M. Kappes, Phys. Rev. B **73**, 094109 (2006)

[13] A. M. Rao, E. Richter, S. Bandow, B. Chase, P. C. Eklund, K. A. Williams, S. Fang, K. R. Subbaswamy, M. Menon, A. Thess, R. E. Smalley, G. Dresselhaus, M.

S. Dresselhaus, Science **275**, 187 (1997)

[14] S. Bandow, S. Asaka, Y. Saito, A. M. Rao, L. Grigorian, E. Richter, P. C. Eklund, Phys. Rev. Lett. **80**, 3779 (1998)

[15] A. K. Sood, P. V. Teresdesai, D. V. S. Muthu, R. Sen, A. Govindaraj, C. N. R. Rao, Phys. Status Solidi B **215**, 393 (1999)

[16] M. J. Peters, L. E. McNeil, J. P. Lu, D. Kahn, Phys. Rev. B **61**, 5939 (2000)

[17] A. M. Rao, P. C. Eklund, S. Bandow, A. Thess, R. E. Smalley, Nature **388**, 257 (1997)

[18] A. M. Rao, J. Chen, E. Richter, U. Schlecht, P. C. Eklund, R.C. Haddon, U.D. Venkateswaran, Y. K. Kwon, D. Tománek, Phys. Rev. Lett. **86**, 3895 (2001)

[19] V. Gadagkar, S. Saha, D. V. S. Muthu, P. K. Maiti, Y.Lansac, A. Jagota, A. Moravsky, R. O. Loutfy, A. K. Sood, J. Nanosci. Nanotechnol. **7**, 1753 (2007)

[20] P. Puech, H. Hubel, D. J. Dunstan, R. R. Bacsa, C. Laurent, W.S. Bacsal, Phys. Rev. Lett. **93**, 095506 (2004)

[21] P. Puech, H. Hubel, D. J. Dunstan, A. Bassil, R. Bacsa, A. Peigney, E. Flahaut, C. Laurent, W. S. Bacsa, Phys. Stat. Sol. (*b*) **241**, 3360 (2004)

[22] J. Kurti, G. Kresse, H. Kuzmany, Phys. Rev. B **58**, 8869 (1998)

[23] H. M. Lawler, D. Areshkin, J. W. Mintmire, C. T. White, Phys. Rev. B **72**, 233403 (2005)

[24] C.Y. Wang, C. Q. Ru, A. Mioduchowski, J. Appl. Phys. **97**, 024310 (2005)

[25] T. Natsuki, T. Hayashi, M. Endo, Appl. Phys. A **83**, 13 (2006)

[26] T. Natsuki, N. Fujita, Q. Q. Ni, M. Endo, J. Appl. Phys. **106**, 084310 (2009)

[27] S. P. Timoshenko, J. M.Gere, Theory of elastic stability, second ed., McGraw-Hill, New York, 1961.

[28] X. Q. He, S. Kitipornchai, K. M. Liew, J. Mech. Phys. Solids **53**, 303 (2005)

[29] R. Saito, R. Matsuo, T. Kimura, G. Dresselhaus, M.S. Dresselhaus, Chem. Phys.

Lett. **348**, 187 (2001)

[30] T. Natsuki, X. W. Lei, Q. Q Ni, M. Endo, Phys. Lett. A **374**, 2670 (2010)

[31] A. Jorio, R. Saito, J.H. Hafner, C.M. Lieber, M. Hunter, T. McClure, G. Dresselhaus and M.S. Dresselhaus, Phys. Rev. Lett. **86**, 1118 (2001)

[32] M. S. Dresselhaus, G. Dresselhaus, A. Joriob, A. G. Souza Filhob, R. Saitof, Carbon **40**, 2043 (2002)

[33] T. C. Chang, Appl. Phys. Lett. **93**, 061901 (2008)

CHAPTER SIX

Conclusions

6 Conclusions

This thesis has investigated the dynamic analysis of CNTs based on continuum mechanical models. Analytical procedures based on the mechanical contimuum model were used to bluit three models of CNTs. The vibration behaviors of CNTs in different conditions were firstly characterized by the three models. The berief summaries are reported as follows.

In Chapter 1, I reviewed references and provided brief summary of CNTs.

In Chapter 2, we aim at characterizing the mechanical properties of SWCNTs. The *C-C* bonds between two adjacent atoms are modeled as Euler beams. According to the relationship of Tersoff-Brenner force theory and potential energy acting on *C-C* bonds, material constants of beam element are determined at the atomic scale. Based on the elastic deformation energy and mechanical equilibrium of a unit in graphite sheet, simply form equations of calculating Young's modulus of armchair and zigzag graphite sheets are derived. Following with the geometrical relationship of SWCNTs in cylindrical coordinates and the structure mechanics approach, Young's modulus and Poisson's ratio of armchair and zigzag SWCNTs are also investigated. The results show that the approach to research mechanical properties of SWCNTs is a concise and valid method.

In Chapter 3, a theoretical analysis of the resonant vibration of DWCNTs and the DWCNTs embedded in an elastic medium is presented based on Euler–Bernoulli beam model and Winkler spring model. The vibration modes of DWCNTs are quite different

from those of SWCNTs. The resonant vibrations of DWCNTs are found to have inphase and anti-phase modes, in which the deflections of the inner and outer nanotubes occur in the same and opposite directions, respectively. For the vibration of DWCNTs with the same harmonic numbers, the resonant frequencies of anti-phase mode are larger than the ones of in-phase mode. Moreover, influence of the surrounding medium on the resonant vibrations is investigated using the Winkler spring model. The results show that surrounding medium makes a strong impact on the vibration frequencies of inphase mode, but little on those of anti-phase mode.

And, the Euler–Bernoulli beam model is also used to analyze the resonant vibration of DWCNTs with inner and outer nanotubes of different lengths. The resonant properties of DWCNTs with different inner and outer nanotube lengths are investigated in detail using this theoretical approach. The resonant vibration is significantly affected by the vibrational modes of the DWCNTs, and by the lengths of the inner and outer nanotubes. For an inner or outer nanotube of constant length, the vibrational frequencies of the DWCNTs increase initially and then decrease as the length of another nanotube increases. A design for nanoelectromechanical devices that operate at various frequencies can be realized by controlling the length of the inner and outer nanotubes of DWCNTs.

In Chapter 4, the vibration behaviors of double-walled carbon nanotubes (DWCNTs), accounting for surface effects, are studied based on the nonlocal Bresse-Timoshenko theory. The influences of the surface elasticity modulus, residual surface stress, nonlocal parameter, axial half-wave number and aspect ratio are investigated in detail. The present analysis shows that the effective surface properties influence on the natural frequency of CNTs are significant. It is shown that the natural frequency is largely affected by the surface material, nonlocal parameter, vibration mode and aspect ratio. Especially in short DWCNTs for the higher vibrational modes,

the influence of the nonlocal and surface effects on vibration frequency is more pronounced.

In Chapter 5, a theoretical vibrational analysis of the RBM of DWCNTs subjected to pressure is presented based on an elastic shell continuum model. The results agree with reported experimental results obtained under different conditions. Frequencies of the RBM in DWCNTs subjected to increasing pressure depend strongly on circumferential wave numbers, but weakly on the aspect ratio and axial half-wave numbers. For the inner and outer tubes of DWCNTs, the frequency of the RBM increases obviously as the pressure increases under different conditions. The range of variation is smaller for the inner tube than the outer tube.

The theoretical analysis of the RBM of CNTs subjected to axial pressure is also presented based on an elastic continuum model. SWCNTs are described as an individual elastic shell and DWCNTs are considered to be two shells coupled through the van der Waals force. The effects of axial pressure, wave numbers and nanotube diameter on the RBM frequency are investigated in detail. The validity of these theoretical results is confirmed through the comparison of the experiment, calculation and simulation. Our results show that the RBM frequency is linearly dependent on the axial pressure and is affected by the wave numbers. We concluded that RBM frequency can be used to characterize the axial pressure acting on both ends of a CNT.